POLITECNICO DI TORINO

SCUOLA DI DOTTORATO

Dottorato in Metrologia: Scienza e Tecnica delle Misure – XXI ciclo

Tesi di Dottorato

Measurement Techniques for Radio Frequency and Microwave Applications



Marco Garelli 135646

Tutore prof. Andrea Ferrero

Coordinatore del corso di dottorato prof. Giulio Barbato

Disclaimer

Many illustrations and figures in this thesis were taken from technical documentation, application notes and manuals of commercial instrumentation. Wherever possible, the material comes from old publications, referring to discontinued products. The reasons behind this choice are:

- 1. the thesis is not an endorsement of a particular instrument model or vendor,
- 2. the quality and technical details of older documentations are by far superior to the current ones.

Summary

This work summarizes the results obtained during the doctorate studies from 2005 to 2008. Most of the time has been spent at the Politecnico di Torino, and about eight months at the National Institute of Standards and Technology, Boulder, Colorado.

The research focused on methods for accurate measurements of electrical quantities in the Radio Frequency and Microwave range. The applications involved multiport scattering parameter measurements, noise power and amplifier noise parameters extraction, large-signal transistor characterization and dielectric permittivity measurement.

In all these fields, it was found mandatory to formulate a consistent measurement model in order to calibrate out the systematic errors affecting the measurements. It seemed therefore appropriate to lay out the work stressing the advantages and disadvantages of different models applied to the same problem.

The work has been divided in four parts.

Chapter 2 deals with small-signal scattering parameter measurement. Error models used in modern Vector Network Analyzers (VNA) will be introduced, with focus on a recent multiport error model suited for low-cost multiport VNAs.

Chapter 3 introduces recent techniques for large-signal characterization of active devices, with particular attention to multiport balanced system like differential amplifiers.

Chapter 4 regards noise measurements. This summarizes the core of my Doctorate studies, that led to the development of two different noise measuring systems.

Finally, Chapter 5 is dedicated to dielectric permittivity measurements at microwave frequencies. This chapter presents methods for improving the measurement accuracy for microwave resonator-based techniques.

Acknowledgements

The most intense experience was, without any doubt, my internship at the National Institute of Standards and Technology. I am in very grateful to Michael Janezic, who hosted me in the Material Project during the first three months. He always offered me support and great encouragement, and, among all, lots of help with not work-related stuff. I'd like to thank James Baker–Jarvis and Bill Riddle from the Material Project for the good suggestions they gave me.

I am also very thankful to James Randa and David Walker from the NIST Noise Project. They gave me the opportunity of spending five months in their lab, conducting free research, and I have learned many lessons of work and life there. In that period, I had the pleasure of working with Dazhen Gu and Robert Billinger, who always gave experienced answers to my naive questions.

I kindly remember the NIST division group leader, Ronald Ginley, and the extraordinary group secretary, Susie Rivera, who took me away lots of the burden connected with my stay and travels.

I am always looking forward to meet again Juanita Morgan, Terry Beach, Ron Schrein, Isadore Million, Nathan Orloff and Henry Romero. We spent very good time –and beer– together.

I also owe a lot to Andrea Ferrero and Valeria Teppati for what I have learned from them in these years. In a totally arbitrary order of preference, I first thank them for having made my period in the United States possible and for their continuous support and encouragement; in second place, I am grateful for their correct reproaches related to "minor" faults when working with them.

Finally, I am glad of having spent many months with the nicest colleagues one could imagine, namely Alessandra Neri and Serena Bonino.

Contents

Sι	ımm	ary	II
\mathbf{A}	ckno	wledgements	III
1	Int r 1.1	roduction The high-frequency measurement problem	1 1
	1.2	Quantities of interest	
	1.3	RF instrumentation	
2	Sma	all-signal Multiport Measurement Techniques	9
	2.1	Basics	9
	2.2	Error models	11
		2.2.1 Complete hardware architecture – Traditional error model	12
		2.2.2 Reduced hardware architecture – Multistate error model	13
		2.2.3 Reduced hardware architecture – Two-state error model	16
	2.3	Non-leaky two-state multiport calibration	18
		2.3.1 General multiport formulation for the error coefficients com-	
		putation	20
		2.3.2 Multiport calibration using one-port and two-port standards .	21
	2.4	Non-leaky two-state multiport de-embedding	29
		2.4.1 Switch error correction	30
		2.4.2 Accuracy considerations – Comparison with the complete hard-	
	~ ~	ware model	30
	2.5	Conclusions	35
3	Lar	ge-Signal Multiport Measurement Techniques	38
	3.1	Basics	38
	3.2	Mixed-mode load-pull bench	46
		3.2.1 Error model and calibration	
		3.2.2 Real-time measurements	51
	3.3	Measurement results	55

		3.3.1	Oscillators and transmitters	. 55
		3.3.2	Balanced Amplifiers	. 57
	3.4	Conclu	usions	. 60
4	The	ermal r	noise Measurement Techniques	61
	4.1	Basics	3	. 61
		4.1.1	Noise in two-port circuits	. 65
		4.1.2	Wave approach to the noise parameters determination	. 68
		4.1.3	Present measurement techniques	. 71
	4.2	The S	PARRAD system at NIST	. 76
		4.2.1	Scattering parameters calibration and measurement	. 78
		4.2.2	Noise calibration and measurement	. 80
		4.2.3	Measurement results	. 84
		4.2.4	Conclusions	. 85
	4.3	The S	PARYF system at Politecnico di Torino	. 86
		4.3.1	Scattering parameters calibration and measurement	. 89
		4.3.2	Noise calibration and measurement	. 94
		4.3.3	Measurement results	. 98
		4.3.4	Conclusions	. 100
5	Die	lectric	Permittivity Measurements by Resonating Methods	102
	5.1	Basics	· · ·	
		5.1.1	High-frequency package and substrate materials	
		5.1.2	Measurement techniques comparison	
		5.1.3	Resonating techniques	
		5.1.4	Resonance parameters measurements	
		5.1.5	Split-Cylinder technique	
	5.2	Impro	vements in the resonance parameters measurement	
		5.2.1	Resonance parameters estimation	
		5.2.2	Optimal parameters and accuracy	
	5.3	Measu	rement results	
	-	5.3.1	Split-Cylinder technique	
		5.3.2	Considerations	
\mathbf{R}^{i}	ihlioo	ranhv		121

List of Tables

2.1	port architectures. The simulated amplifier has $ S_{31} = S_{42} = 40 \text{ dB}$
	gain and $ S_{31}/S_{13} = S_{42}/S_{24} = 60$ dB isolation; the receiver's channels are supposed to have 60 dB signal-to-noise ratio
3.1	Performance comparison between two different load configurations 53
4.1	Y-factor technique strengths and weaknesses
4.2	Hot/cold source technique strengths and weaknesses
4.3	Cold source technique strengths and weaknesses
5.1	Typical properties of plastic substrates
5.2	General properties of substrate materials
5.3	Summary of dielectric substrates measurement categories, compared
	in terms of typical uncertainties

List of Figures

1.1 1.2	Two-port scattering parameters definition. Courtesy of Agilent [1] HP 8405A simplified block schematic. Courtesy of HP [2]	4
1.3	HP 8510 Vector Network Analyzer system and simplified test-set	_
. .	block schematic. Courtesy of HP [3]	7
1.4	Schematic representation of the relevant signal paths during the raw	_
1 5	S-parameters measurement.	7
1.5	Agilent PNA-X four-port test-set simplified block schematic, courtesy of Agilent [4]	8
2.1	Comparison between the complete hardware and the two-state hard-	
	ware error model, evidencing some commercial VNA performances	12
2.2	Generic complete hardware architecture	12
2.3	Generic reduced hardware multiport test-set. $M_A < N$ channels mea-	
	sure the incident waves, while $M_B=N$ read the reflected waves	14
2.4	The port match independence of the unconnected port	17
2.5	Two-state error model	18
2.6	The $(N+2)$ -samplers two-state hardware architecture	22
2.7	The 12-port $(N + 2)$ -samplers Anritsu 37397D VNA has 40 MHz to	
	67 GHz frequency range. The system consists of a 37000D-family two-	
	port VNA (top) coupled to an extension box (bottom) that contains	
	the port switches and auxiliary power supplies. The measurement	
	couplers are contained in six modules (two port each), which are	
	placed as close as possible to the DUT in order to minimize high-	
	frequency losses. The measurement and calibration software runs on	
•	an external computer. Courtesy of Anritsu [5]	23
2.8	Possible calibration scheme for a four-port two-state network ana-	
	lyzer. (a) Unknown thru in the AA case, the same of a complete	
	hardware architecture. (b) Unknown thru in the AB case	23
2.9	Example of two-port calibration	24
2.10	Two-port VNA architectures	25
2.11	Example of merging strategy using a known standard	27
2.12	Example of merging strategy using a unknown reciprocal standard	28

2.13	Miteq 2 – 4 GHz amplifier measurements. Shown is S_{22} parameter. Complete hardware model (left) and two-state model (right)	32
2.14	CMOS balanced amplifier measurement and standard uncertainty comparison. Combined standard uncertainties due to the measure-	
	ment noise for the S_{44} reflection parameter	34
2.15	CMOS balanced amplifier measurement and standard uncertainty comparison. Combined standard uncertainties due to the measurement noise for the S_{34} crosstalk parameter	35
2.16	CMOS balanced amplifier measurement and standard uncertainty comparison. Combined standard uncertainties due to the measurement noise for the S_{31} gain parameter	36
2.17	On-wafer balun measurement and standard uncertainty comparison. Combined standard uncertainties due to the measurement noise for the S_{34} transmission parameter	37
3.1	Large signal P_{in}/P_{out} plot. As the amplifier turns into compression, the gain lowers but the efficiency generally increases	39
3.2	Large-signal and small-signal design comparison	39
3.3	An example of load-pull map. The plotted curves are the constant output power loci interpolated from the measurement points	40
3.4	Microwave passive tuner example. The mismatch created by the slug insertion varies the tuner's reflection coefficient magnitude, while its phase depends on the slug position along the slabling	40
3.5	phase depends on the slug position along the slabline	40
3.6	Basic configuration for the two-port load-pull test-set at Politecnico di Torino [6].	42
3.7	Passive Tuner System with 2nd and 3rd Harmonic Source and Load	
J.,	Tuning. Courtesy of Maury Microwave Co. [7]	43
3.8	Active load block schematic	43
3.9	Harmonic active load block schematic	44
3.10	Active source block schematic	45
3.11	Load-pull and source-pull test-set based on active loops	45
3.12	The differential load-pull system at the Politecnico di Torino. The VNA is a HP8510C with a HP8511A test-set	46
3.13	The mixed-mode active loop principle	46
	An example of multiport scattering parameter calibration. Three one-port standards (Short, Open, Load) are used at port 1, and three	
	known thru standards are connected between 1-3, 1-4, 2-4	48

3.15	Power calibration. A thru standard is connected between ports 1 and	
	3, and Short, Open, Load standards are measured at the auxiliary	
	port 5	48
3.16	Custom-made comb generator block schematic. With a RF source fre-	
	quency of 2 GHz, the useful harmonic content extends up to 12 GHz.	
	The auxiliary source is locked to the VNA $10~\mathrm{MHz}$ reference signal	50
3.17	Time-domain waveform calibration. A thru standard is connected	
	between ports 1 and 3, and the voltage waveform at the auxiliary	
	port 5 is measured by the sampling scope	50
3.18	Schematic representation of the source and load tuners and their	
	mixed-mode parameters	52
3.19	Mixed-mode load-pull bench intended for balanced transmitter char-	
	acterization	56
3.20	STLC2150 internal block schematic	56
3.21	STLC2150 Load-pull maps for the differential-mode reflection coeffi-	
	cient at fundamental frequency $\Gamma_{LD}(f_0)$	57
3.22	STLC2150 second harmonic common-mode reflection coefficient tun-	
	$ing (\Gamma_{LC}(2f_0) = 0.9). \dots \dots \dots \dots \dots \dots \dots \dots$	57
3.23	1 ,	
	flection coefficient $\Gamma_{LD}(f_0)$ tuning	58
3.24	1 /	-0
	1 dB compression point of the differential-mode gain G_D	59
3.25	TC226 differential-mode power sweep at fundamental. The load is	۲0
2.00	tuned to the optimum differential-mode reflection coefficient	59
3.26	TC226 differential-mode output waveforms while sweeping the second	
	harmonic differential-mode load. The differential load at fundamental	60
	is tuned to the maximum output power point	UU
4.1	Effect of the internal noise in an amplifier. The signal-to-noise ratio	
	at the output (b) is lower than the one at the input (a). Courtesy of	
	Agilent [8]	62
4.2	The NIST coaxial (GPC-7) cryogenic standard [9]	63
4.3	Block schematic of the Agilent 346A/B/C commercial noise diode	
	source. Courtesy of Agilent [10]	63
4.4	Block schematic of the NIST NFRAD radiometer	64
4.5	Total-power isolated radiometer block schematic	65
4.6	Noise circles. Courtesy of Agilent [8]	66
4.7	Graphical representation of the equivalent noise temperature defini-	
	tion. Courtesy of Agilent [11]	67
4.8	Graphical representation of a two-port noisy device	68

4.9	Graphical representation of a two-port noisy amplifier with (right)	
	and without (left) the noise sources referenced to the input port	69
4.10	Model for a two-port noisy amplifier connected to a noisy source	69
4.11	The propagation of the noise contributions in a cascade. Courtesy of	
	Hewlett Packard [12]	72
4.12	Y-factor measurement principle	72
4.13	DUT noise parameter extraction by the Y-factor method. Courtesy	
	of Hewlett–Packard [13]	73
4.14	Hot/cold and cold source measurement principle. Courtesy of Agilent	
	[8]	74
4.15	Typical hot/cold source measurement test-set	75
4.16	SPARRAD system block schematic	77
4.17	SPARRAD system picture	79
4.18	Scattering parameters calibration at P1 and P2. For clarity, unused	
	connections are not drawn	79
4.19	Scattering parameters calibration at P3. For clarity, unused connec-	
	tions are not drawn	80
4.20	Noise parameter measurement, ambient terminations	80
4.21	Noise parameter measurement, non-ambient terminations (internal	
	noise diode or external sources)	81
4.22	Model for the noise parameter measurement	83
4.23	Minimum noise temperature T_{min} vs. frequency. NIST data courtesy	
	of Dazhen Gu	85
4.24	Optimum reflection coefficient G_{opt} vs. frequency. NIST data cour-	
	tesy of Dazhen Gu	85
	Block schematic of the SPARYF system	87
4.26	Basic block schematic for the tuner section measurement	87
4.27	Main signal paths for the tuner section measurement. The schematic	
	is a reduction of Fig. 4.25; for clarity, unused connections are not	
	drawn	88
4.28	Main signal paths for the DUT S-parameters measurement. The	
	schematic is a reduction of Fig. 4.25; for clarity, unused connections	
	are not drawn	88
4.29		
	schematic is a reduction of Fig. 4.25; for clarity, unused connections	
	are not drawn	88
4.30	Calibration at Ports 1, 2. The schematic is a reduction of Fig. 4.25;	
	for clarity, unused connections are not drawn	90
4.31	Calibration at Ports 3, 4. The schematic is a reduction of Fig. 4.25;	
	for clarity, unused connections are not drawn	91

4.32	Calibration at Ports 1, 3. The schematic is a reduction of Fig. 4.25;	
	for clarity, unused connections are not drawn	91
4.33	Parameters of interest during the scattering parameters measurement.	93
4.34	Noise receiver calibration model	95
4.35	Available gain comparison for five different tuner positions	99
4.36	50 Ω noise figure comparison	99
4.37	DUT used in the Γ_{opt} and R_n test	100
4.38	Comparison between measurement and simulation of Γ_{opt} and R_n	100
5.1	An example of transmission-mode cavity resonator	
5.2	Measured quality factor ($f_0 = 10 \text{ GHz}$) vs. coupling losses	
5.3	Examples of measured resonance curves	
5.4	Lumped-element electrical model of a cavity resonator	
5.5	The Split-Cylinder cavity resonator	
5.6	Transmission-mode cavity resonator model	110
5.7	Simulation of the effect of the normalized frequency span ξ on the	
	resonant frequency and Q factor accuracy. The resonance parameters	
	were $Q = 10000$, $f_0 = 10$ GHz and peak magnitude $S_{21pk} = -50$ dB;	
	201 frequency points were used; no crosstalk and no cable delay are simulated. The fitting maximum degree is 3	111
5.8	Simulation of the effect of uncompensated cables on the quality factor	114
0.0	estimation. The simulated TE_{01p} resonance mode has $p=23$, $Q=$	
	100, $f_0 = 10$ GHz and peak magnitude $S_{21pk} = -50$ dB; crosstalk has	
	-80 dB magnitude . The cable dielectric has $\epsilon_r = 2.1$. 201 frequency	
	points were used and the fitting maximum degree is 41	115
5.9	Simulation of the combined worst-case effect of mismatches and long	
	cables. The simulated TE_{01p} resonance mode has $p = 23$, $Q = 100$,	
	$f_0 = 10 \text{ GHz}$ and peak magnitude $S_{21pk} = -50 \text{ dB}$; crosstalk has	
	−80 dB magnitude. 201 frequency points were used	115
5.10	Simulation of the effect of noise. Realistic conditions were simu-	
	lated. The resonance has $f_0 = 10$ GHz and peak magnitude -50 dB;	
	crosstalk has -80 dB magnitude. 201 frequency points were used in	
	a normalized frequency span of $\xi = 3$. 500 different noise realizations	110
- 11	were simulated with a fitting maximum degree of 3	
	NIST 10 GHz 60 mm cavity resonator measurement.	118
5.12	NIST 10 GHz 60 mm cavity resonator measurement comparison. The	
	measurement data are the same used in Fig. 5.11. The black error	
	bars are the measurement results, the gray ones are the computed uncertainties. 200 iterations were used for each measurement	112
5 12	Split-Cylinder method permittivity and loss tangent results	
σ . $\tau \sigma$	phi-cymidel meinod permininiyi and 1055 tangent lesuits	$\mathbf{L}\mathbf{L}\mathcal{J}$

5.14	Split-Cylinder method permittivity and loss tangent results with the	
	NIST magnitude-only method	120

Chapter 1

Introduction

The Radio Frequency and Microwave electronic field is certainly a minor part of the whole electronics industry. Still, high-frequency electronics have continuously grown during the past three decades, and the instrumentation has tracked the increased demand for speed and accuracy. Faster measurements have been made possible by the progresses in the electronic industry, while accuracy improved thanks to the gradual refinement in the instrumentation calibration and measurement techniques.

This trend has greatly profited by the widespread diffusion of wireless communication systems, as the associated demand for better devices and large-scale production greatly pushed the high-frequency limit and cut costs. Recently, the high-speed digital electronics world pushed the clock frequencies by far above 1 GHz, facing with measurements typical of RF and microwave devices.

1.1 The high-frequency measurement problem

Modern high-frequency measurements share a common denominator: complexity.

Complex test-sets are needed in most applications, since it is often required to measure multiple performances at the same time, and this is particularly true in large-signal measurements. Multiport small-signal measurements either require time-consuming repeated two-port measurements, or impose the use of expensive multiport test-sets. The second solution gained advantage due to more accurate results, but the cost urges instrumentation designers to find out simpler hardware solutions, which sometimes require additional efforts to grant a satisfactory accuracy.

As the frequency increases, the measurement is affected by non-negligible systematic effects due to the test system's non-idealities. For example, the direct measurement of a voltage or a current at such frequencies is not achievable, due to the test probes loading effect. Above 1 GHz, accuracy improvements are not primarily obtained by increasing the measuring system resolution, but are achieved

by removing the systematic sources of uncertainty in a more effective way. Thus, the system calibration gains crucial importance in high-frequency measurements. Conceptually, microwave measurements involve three steps:

- 1. Given an application, a consistent error model, suited to the actual instrumentation hardware, has to be found. The model defines the relationships that link the quantities of interest to the readings. Their parameters are called error coefficients.
- 2. The error coefficients are computed during the system's calibration, by the measurement of known devices (calibration standards) or by comparison with reference instruments. This step is usually performed just before the measurement session, and after a proper instrument warm-up.
- 3. Finally, the device's parameters are extracted (de-embedded) from the raw measurements by the knowledge of the error coefficients.

Quantities of interest 1.2

One peculiarity of high-frequency measurement is that the quantities of interest can be directly measured only in rare cases. This is particularly true for common quantities, like voltages and currents. Therefore, it is mandatory to define the quantities that can be measured, then relate the parameters of interest to them. In other words, we need a convenient way to represent the measurand behavior, which suits well to the high-frequency measurement constraints.

The preferred representation makes use of traveling waves, which express the propagation of a sinusoidal signal along a transmission line, and define the performances of a device in terms of power flow and scattering parameters [14]. Anyway, the usual electrical quantities are not abandoned, as one can define the modal voltage and current phasors in a mono-modal transmission line of real characteristic impedance $Z_{\infty} = 1/Y_{\infty}$ and propagation constant k_z :

$$V(z) \equiv V^{+}(z) + V^{-}(z)$$
 (1.1)

$$I(z) \equiv Y_{\infty}V^{+}(z) - Y_{\infty}V^{-}(z) \tag{1.2}$$

where V^+ and V^- are called progressive and regressive voltages. Their dependence with z is

$$V^{+}(z) = V_{0}^{+} e^{-jk_{z}z}$$

$$V^{-}(z) = V_{0}^{-} e^{+jk_{z}z}.$$
(1.3)

$$V^{-}(z) = V_0^{-} e^{+jk_z z}. (1.4)$$

The traveling waves a (forward) and b (reverse) are defined as

$$a \equiv \frac{V^+}{\sqrt{Z_{\infty}}} \tag{1.5}$$

$$b \equiv \frac{V^{-}}{\sqrt{Z_{\infty}}},\tag{1.6}$$

so that their norm has dimension of power¹ and expresses the power that propagates in the forward and reverse direction:

$$P^{+} \equiv |a|^{2} = \frac{|V^{+}|^{2}}{Z_{\infty}} \tag{1.7}$$

$$P^{-} \equiv |b|^{2} = \frac{|V^{-}|^{2}}{Z_{\infty}}, \tag{1.8}$$

and the power absorbed in a device becomes

$$P = |a|^2 - |b|^2. (1.9)$$

This rigorously holds only with a real characteristic impedance [15].

The use of traveling waves leads to a convenient representation of a linear N-port device, in terms of the scattering parameters S_{ij} :

$$\begin{bmatrix}
b_1 \\
b_2 \\
\vdots \\
b_N
\end{bmatrix} = \begin{bmatrix}
S_{11} & S_{12} & \dots & S_{1N} \\
S_{21} & \ddots & & S_{2N} \\
\vdots & & \ddots & \vdots \\
S_{N1} & S_{N2} & \dots & S_{NN}
\end{bmatrix} \begin{bmatrix}
a_1 \\
a_2 \\
\vdots \\
a_N
\end{bmatrix}$$
(1.10)

where b_i are the reflected (scattered) waves and a_i the incident ones (i = 1...N). The matrix S establishes a unique relationship that fully describes a linear device with no independent sources. Fig. 1.1 sketches the two-port S-matrix parameters.

The scattering parameter representation is also used for linear devices with internal sources, like a one-port signal generator. In this case, an independent term c is added, leading to:

$$\boldsymbol{b} = \boldsymbol{S}\boldsymbol{a} + \boldsymbol{c} \tag{1.11}$$

$$\boldsymbol{c} = \begin{bmatrix} c_1 \\ c_2 \\ \vdots \\ c_N \end{bmatrix} \tag{1.12}$$

¹For convenience, V^+ and V^- are expressed as effective (root-mean-square) voltages, otherwise, a factor 1/2 would appear in (1.7), (1.8), (1.9) and derived equations.

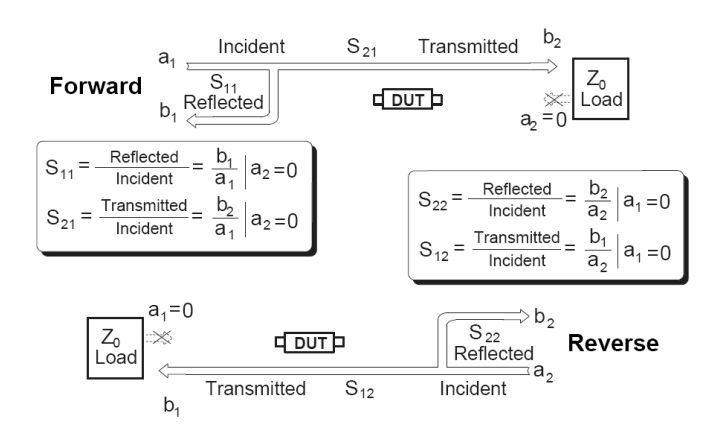


Figure 1.1. Two-port scattering parameters definition. Courtesy of Agilent [1].

c represents the independent wave generated by the device, and it should be understood as the *excess* wave vector leaving the device's ports rather than $c = b|_{a=0}$, since the required condition a = 0 cannot be always satisfied. The magnitude $|c_i|^2$ is the *excess* power that the device scatters at port i.

The traveling wave variables are not restricted to deterministic signals. The representation of the electrical noise internal to active and passive devices is advantageous when using noise waves [16–18]. In this case, the wave variables represent non-deterministic signals. Still, the deterministic excess noise power density generated at port i can be computed as $\overline{|c_i|^2}$, where the overline means statistical expectation.

The use of spectral power density is due to the broad-band nature of noise. In high-frequency linear active devices, the generated noise is mainly *shot* noise, which has a flat spectrum over several decades [19]. It has similar properties as the Johnson-Nyquist noise [20, 21], both being white Gaussian noise signals. The noise temperature spectrum T(f) for a passive device is

$$k_B T(f) = \frac{hf}{e^{\frac{hf}{\left(k_B T_{phy}\right)}} - 1} \tag{1.13}$$

where k_B is the Boltzmann's constant, h is Plank's constant and T_{phy} is the physical device temperature. At microwave frequencies, in most of the cases the noise temperature can be well approximated by $T(f) \approx T_{phy}$, and the approximation will be always used in the following.

The second-order statistical properties of a noise wave vector are given by its

correlation matrix:

$$\boldsymbol{C} = \overline{\boldsymbol{c}} \boldsymbol{c}^{\dagger} = \begin{bmatrix} \overline{|c_{1}|^{2}} & \overline{c_{1}c_{2}^{*}} & \dots & \overline{c_{1}c_{N}^{*}} \\ \overline{c_{2}c_{1}^{*}} & \ddots & \overline{c_{2}c_{N}^{*}} \\ \vdots & & \ddots & \vdots \\ \overline{c_{N}c_{1}^{*}} & \overline{c_{N}c_{2}^{*}} & \dots & \overline{|c_{N}|^{2}} \end{bmatrix}$$

$$(1.14)$$

where the dagger (†) means transpose complex conjugate. As can be noted, this correlation matrix is hermitian, so that $C_{ij} = C_{ji}^*$. While the diagonal elements represent power densities, the off-diagonal ones are cross-correlation spectra, and are complex numbers.

Passive devices, kept at a uniform temperature T_{phy} , have a particular noise correlation matrix. The result is known as Bosma's theorem [22]:

$$C = k_B T_{vhu} \left(I - SS^{\dagger} \right). \tag{1.15}$$

1.3 RF instrumentation

RF and microwave measurement systems are coarsely divided into two groups:

scalar instruments, which are sensible to the signal intensity, *i.e.* its power. These instruments are either based on non-linear components, like a square-law diode, or on electro-thermal effects, like the bolometers, that can convert the high-frequency power in a DC signal.

vectorial instruments, which can measure the intensity of two isofrequential signals and their relative phase. These instruments are generally more complex than the previous ones, but they provide a phase information that is often of crucial importance.

The first famous vectorial instrument was the HP 8405A vectorial voltmeter in the mid 1960s. The 8405 was used to sample two voltages in the 1 MHz to 1 GHz frequency range, displaying on analog meters the voltage intensities and relative phase. The simplified block schematic is shown in Fig. 1.2, and this architecture is still the foundation of modern network analyzers. The probes were designed to have high impedance (100 k Ω) and low parallel capacitance (2.5 pF), thus minimizing the loading effects. The phase-lock system tracks the sinusoidal signal at the input of channel A, and adjusts the Voltage Tuned Oscillator frequency to have a 20 kHz IF output. The frequency conversion is made by two Schottky diode samplers placed in the probes. The sampling pulses are generated by a step-recovery diode [23, 24] driven by the Local Oscillator (LO) operating in the 0.98-2 MHz range. This avoids the use of a high-frequency LO, at the expense of a greater conversion loss.

Vector Network Analyzers (VNA) are made of three key components.

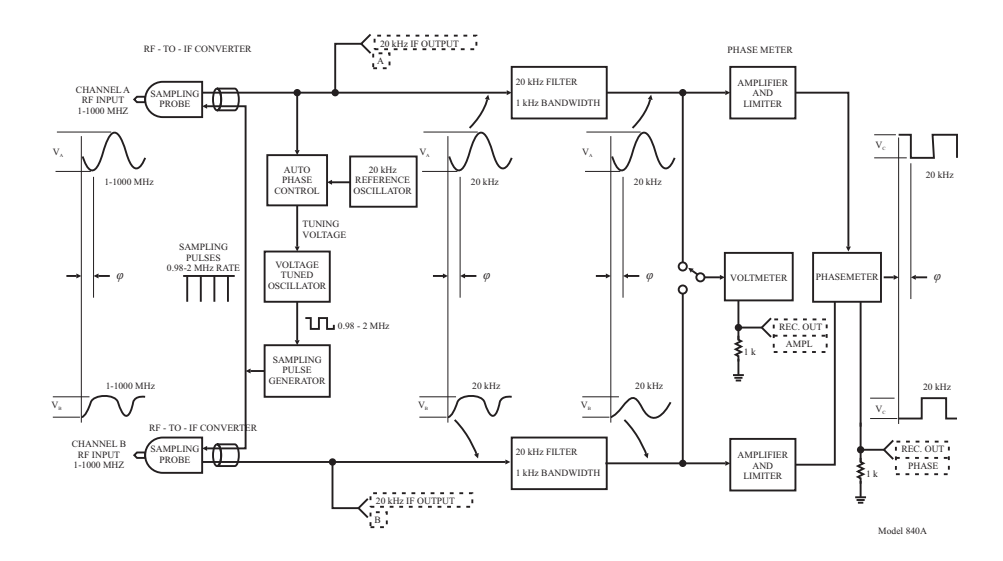


Figure 1.2. HP 8405A simplified block schematic. Courtesy of HP [2].

- 1. A signal source, which provides the RF stimulus signal.
- 2. A test-set, which contains the test hardware for the device under test (DUT) incident and reflected waves measurements. The test-set is therefore the key component in high-frequency measurements.
- 3. A vectorial receiver, that measures, in magnitude and phase, the sampled signals from the test-set.

Moreover, a processing unit and a user interface with graphical display complete the set-up.

The HP 8410 and later the HP 8510 vector network analyzer systems are representative examples of such division, since each component is contained in a separate enclosure (Fig. 1.3). The HP 8515 two-port test-set is based on broadband directional bridges and splitters, and the frequency range is 45 MHz to 26.5 GHz. Like directional couplers, the bridges separate out the incident and reflected waves at each DUT port, but have greater bandwidth. The coupled signals $(a_{\rm m1}, b_{\rm m1}, b_{\rm m2}$ and $a_{\rm m2})$ are then down-converted to an intermediate frequency (IF) of 20 MHz by four microwave samplers, which share the same local oscillator (LO) signal.

The HP 8510 analog phase lock system closely resembles the one of the HP 8405, with substantial improvements and digital pre-tune. Both are based on samplers, and the phase lock is performed on the reference signal, at the intermediate frequency, by acting on the local oscillator frequency.

The external RF stimulus is switched, internally to the test-set, by a pin-diode switch. The signal paths for the raw measurement of the DUT S-matrix are shown in

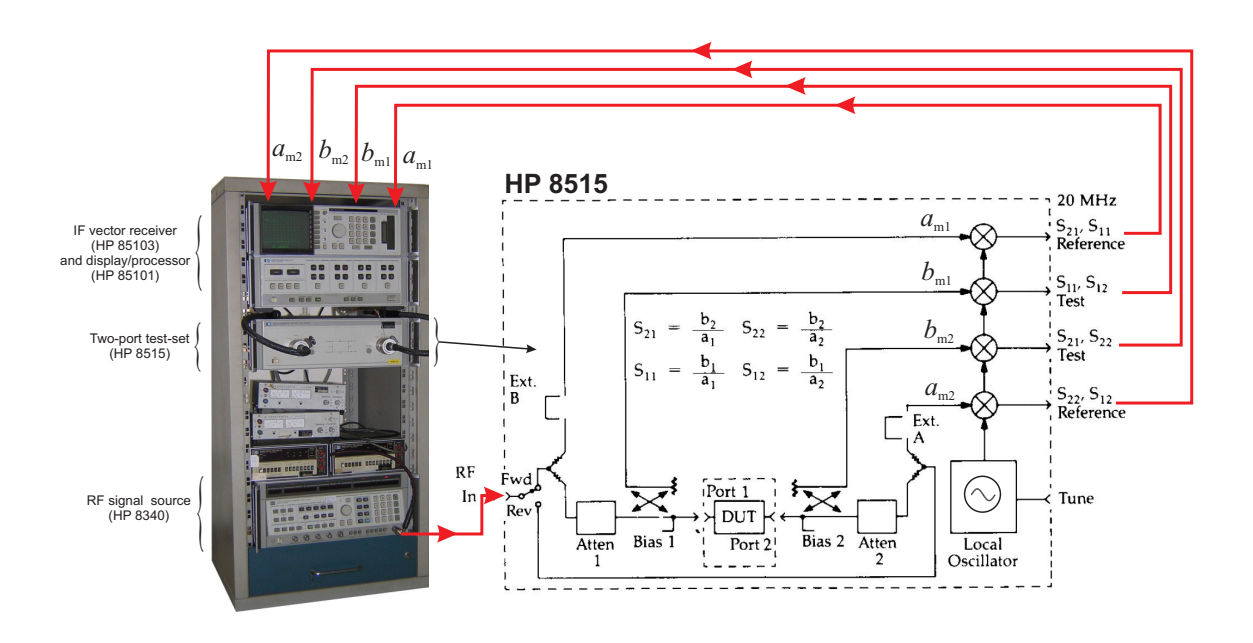


Figure 1.3. HP 8510 Vector Network Analyzer system and simplified test-set block schematic. Courtesy of HP [3].

Fig. 1.4. The raw measurements are affected by systematic effects (finite directivity,

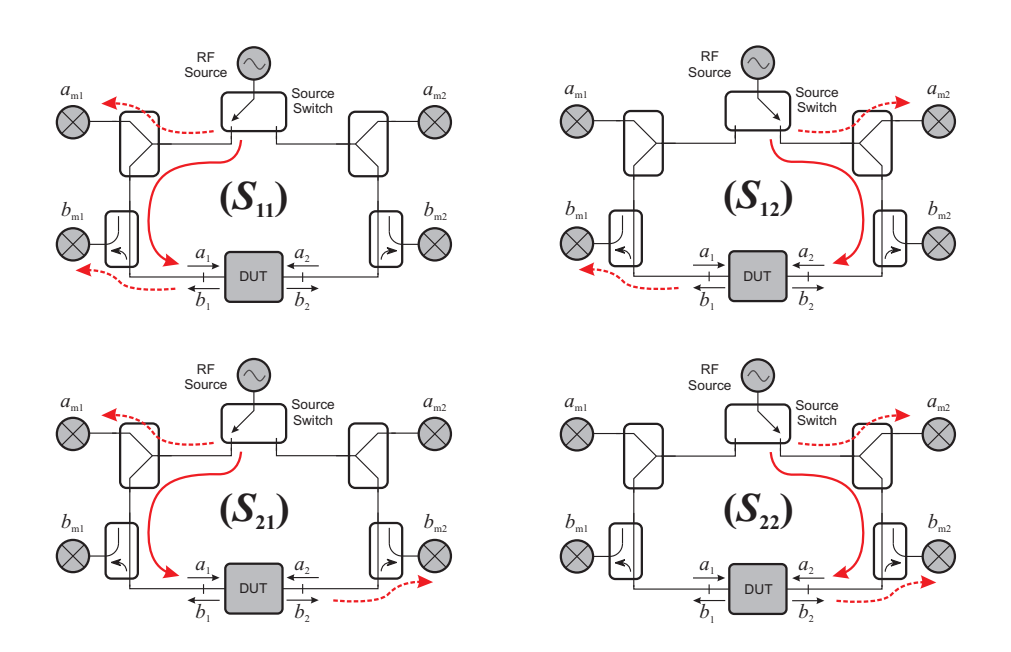


Figure 1.4. Schematic representation of the relevant signal paths during the raw S-parameters measurement.

coupling flatness, etc.) due to the imperfect realization of the test-set components. Therefore, the system calibration is mandatory to correct for these errors.

As the characterization needs for devices with more than two ports grew, multiport vector network analyzer were devised. A modern multiport test-set, belonging to the PNA-X VNA, is sketched in Fig. 1.5. Basically, this test-set is a four-port

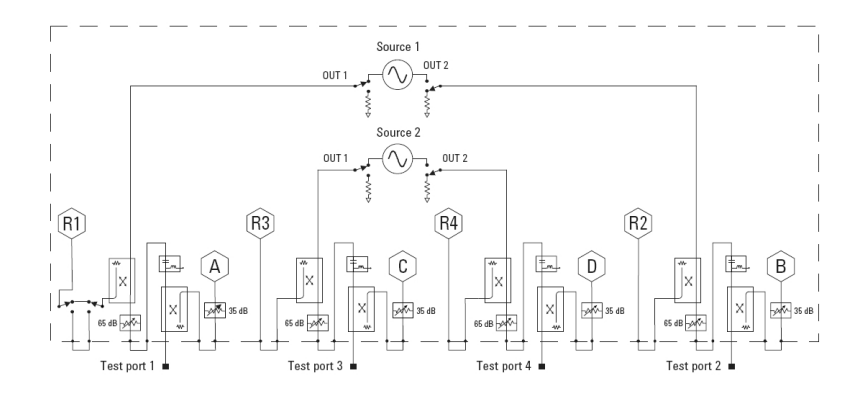


Figure 1.5. Agilent PNA-X four-port test-set simplified block schematic, courtesy of Agilent [4].

extension of the two-port HP 8515. Each port has two directional bridges in order to sample the incident (R1, R2, R3 and R4 receiver channels) and reflected (A, B, C and D channels) waves. Each receiver channel is mixer-based, so that the down-conversion process is made by a mixer driven by a high-frequency local oscillator. Due to the need for a local oscillator at microwave frequencies, the set-up is more expensive, but the mixers conversion loss is by far lower than the samplers' one, and thus the instrument dynamic range is increased (140 dB dynamic range with a 1 Hz IF bandwidth).

The RF stimulus comes from two RF sources, the first can drive ports 1 and 2, the second ports 3 and 4. A single source with a SP4T RF switch could be used as well, as done in most four-port VNAs. The second source, in this case, is needed for advanced non-linear measurement functionalities of the instrument.

The multiport measurement process is similar to the two-port one. When port 1 is driven, the raw $S_{11}^{raw} = A/R1$, $S_{21}^{raw} = B/R1$, $S_{31}^{raw} = C/R1$ and $S_{41}^{raw} = D/R1$ can be acquired. Similarly, the remaining raw parameters are measured with RF drive to port 2, 3 and 4.

Compared to the two-port case, multiport raw measurements are even more affected by systematic errors, since the set-up is more complex and thus good hardware symmetry in the branches is harder to achieve.

Chapter 2

Small-signal Multiport Measurement Techniques

Original contributions to the multiport vector network analyzer calibration theory are presented in this Thesis. The research work started at the Politecnico di Torino during 2006, and continued through the entire Doctorate course, leading to the formulation of a new multiport error model, which was proved and implemented on various commercial instrumentation.

This Chapter's first aim is to present a unified approach to the error model definition of microwave multiport test-sets. A comparison between present and new solutions will be drawn. Finally, an analysis of the measurement noise effects on the multiport scattering parameters will be presented.

2.1 Basics

Small-signal characterization requires the device to respond linearly to an excitation signal. For passive devices, the behavior is almost linear even if the drive signal amplitude is widely varied. Active devices require additional care when driving the input ports to avoid saturation at the outputs.

Early multiport measurements were performed by two-port vector network analyzers connected at turn to the DUT ports, while matching the remaining ports with 50 Ω loads [25]. The procedure has the advantage of being very low-cost, but the measurement time steeply increases with the number of ports. Moreover, taking into account the effect of imperfect matches of the auxiliary loads requires more complex calibration schemes [26–28], and it becomes practically unsuitable for on-wafer measurements.

The scattering matrix S of a N-port device has been defined in (1.10) as

$$b = Sa$$
.

This is a linear system in the N^2 unknowns S_{ij} . Its solution requires:

- ullet N independent driving conditions (typically, the test signal is applied to the N DUT ports in turn) and
- the knowledge of the actual incident (a_k) and reflected (b_k) wave vectors for each driving condition k.

By stacking the different measurement equations, it is possible to grow the linear system

$$\underbrace{\begin{bmatrix} \mathbf{b}_1 & \mathbf{b}_2 & \dots & \mathbf{b}_N \end{bmatrix}}_{\mathbf{B}} = \mathbf{S} \underbrace{\begin{bmatrix} \mathbf{a}_1 & \mathbf{a}_2 & \dots & \mathbf{a}_N \end{bmatrix}}_{\mathbf{A}}, \tag{2.1}$$

from which the scattering matrix is computed as

$$S = BA^{-1}. (2.2)$$

This procedure is similar to the so-called *switch error correction*, as it corrects for imperfections in the RF signal source switch, *e.g.* non perfect isolation that causes signal leakage to the non-driven ports.

As seen in the previous Chapter, a_k and b_k cannot be directly measured. Therefore, they should be computed from the measured waves a_{mk} and b_{mk} and from the calibration coefficients, depending on the error model.

The VNA error models are based on one underlying assumption: the measurement system is completely linear. Thus, the actual waves are simply a linear combination of the measured ones weighted by the error coefficients. This rigorously holds for all the error models treated in this Thesis.

Despite of its simple form, the structure of (2.1) gives remarkable informations about the small-signal measurement problem.

- 1. A single scattering parameter S_{ij} cannot be computed merely from the measurements at ports i and j. Its computation, actually, requires the full set of measurements at all the N ports and for all the N source positions.
- 2. The scattering matrix computation is completely insensitive to any non-zero factor that multiplies both A and B:

$$B = SA \longleftrightarrow (\alpha B) = S(\alpha A),$$

provided that $\alpha \neq 0$. This justifies the error coefficients normalization, as the scattering calibration problem can be rigorously solved by normalizing all the error coefficients to one term, unknown but non-zero. This will be proved in Section 2.4.

3. Similarly to the previous point, \boldsymbol{A} and \boldsymbol{B} can be right-multiplied by any non-singular matrix \boldsymbol{R} :

$$B = SA \longleftrightarrow (BR) = S(AR),$$

provided that $\det(\mathbf{R}) \neq 0$. This allows the use of ratioed measurements, like $b_{\rm m2}/a_{\rm m1}$, which is natively performed in the VNA and spares N measurements each time the DUT is characterized. Section 2.4 will show this in detail.

4. It may appear that the S-matrix computation in (2.1) requires 2N measurements for each driving condition, leading to a total of $2N^2$ measurements. This is a rather redundant solution, since solving the system (1.10) involves N^2 independent equations, without any constraint on the number of measurements. The minimum number of measurements depends on the test-set architecture and on the error model, as will be shown.

The cost and complexity of a multiport VNA can be effectively parametrized by two numbers.

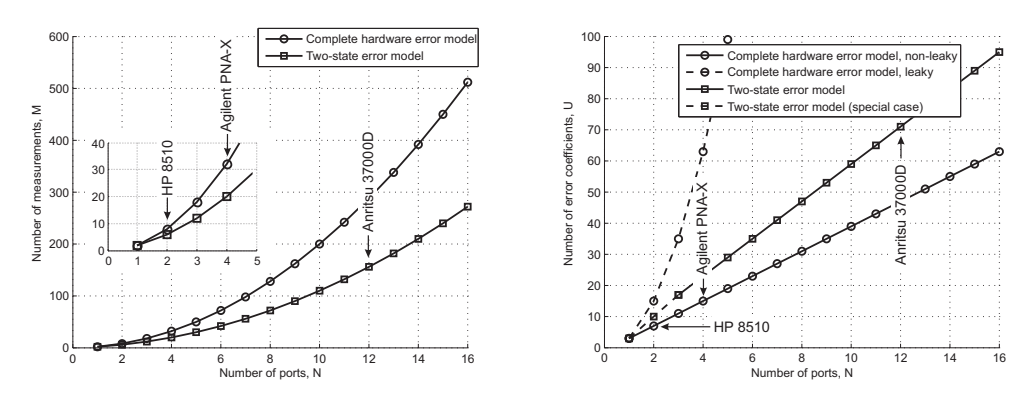
The total number of measurements, M. It relates to the hardware cost (number of receiver channels), as well as to the measurement speed. The measurements number is proportional to the number of DUT scattering parameters S_{ij} , that grows with the square of the number of ports, *i.e.* $M = O(N^2)$.

The number of error coefficients, U. It sets the error model complexity, and is indicative of the calibration standards measurements to be performed during the calibration, although their amount strongly depends on the calibration scheme. Typically, $U = O(N^2)$ for leaky error models, that account for crosstalk between the measurement channels, and U = O(N) for non-leaky error models, which assume negligible crosstalk.

As an example, a comparison between two VNA error models is made in Fig. 2.1. The error models will be analyzed in this Chapter, for now it is sufficient to say that the "complete hardware" error model is the one traditionally used, and the "two-state" model is a newly developed one.

2.2 Error models

A brief overview of the present multiport error model definitions is presented in Section 2.2.1. Section 2.2.2 draws the modeling for multiport VNA with a reduced number of measuring channels, while Section 2.2.3 presents a new, efficient, model for such hardware.



(a) Total number of measurements (M) vs. (b) Total number of error coefficients (U) vs. number of ports (N).

Figure 2.1. Comparison between the complete hardware and the two-state hardware error model, evidencing some commercial VNA performances.

2.2.1 Complete hardware architecture – Traditional error model

The multiport measurement problem was rigorously assessed only a decade ago [29,30]. The hardware solution, sketched in Fig. 2.2, uses two measurement channels for each DUT port, thus 2N readings are taken for each source position, leading to $M=2N^2$. The test-set is said to have a *complete hardware architecture*, since all the waves can be measured.

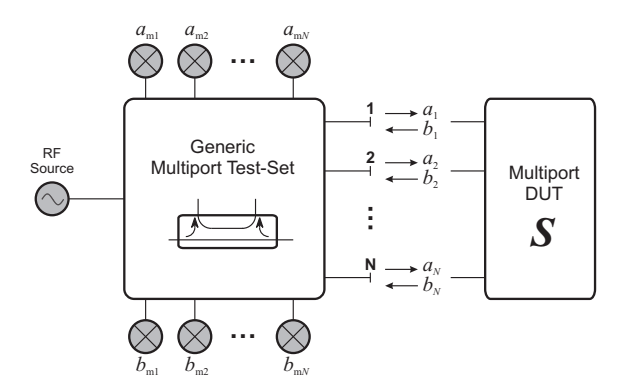


Figure 2.2. Generic complete hardware architecture.

The measurement channels are labeled $a_{\rm m1}, a_{\rm m2}, \ldots a_{\rm mN}$ and $b_{\rm m1}, b_{\rm m2}, \ldots b_{\rm mN}$ since they primarily respond to the a and b waves, respectively. In this way, the

number of $a_{\rm m}$ channels is $M_A = N$, as well as the number of $b_{\rm m}$ channels $M_B = N$. The reflected waves are typically measured by directional couplers or directional bridges, while the incident ones may be measured by directional couplers or power splitters, as seen for example in the PNA-X test-set of Fig. 1.5.

The measuring system is completely linear, thus a linear relationship holds between the actual and measured quantities:

$$\begin{bmatrix} \mathbf{a} \\ \mathbf{b} \end{bmatrix} = \begin{bmatrix} -\mathbf{H} & \mathbf{L} \\ -\mathbf{M} & \mathbf{K} \end{bmatrix} \begin{bmatrix} \mathbf{a}_{\mathrm{m}} \\ \mathbf{b}_{\mathrm{m}} \end{bmatrix}, \tag{2.3}$$

being

$$\boldsymbol{a}_{\mathrm{m}} = \begin{bmatrix} a_{\mathrm{m}1} \\ a_{\mathrm{m}2} \\ \vdots \\ a_{\mathrm{m}N} \end{bmatrix}, \quad \boldsymbol{b}_{\mathrm{m}} = \begin{bmatrix} b_{\mathrm{m}1} \\ b_{\mathrm{m}2} \\ \vdots \\ b_{\mathrm{m}N} \end{bmatrix}. \tag{2.4}$$

The matrices H, L, M and K contain the error coefficients and are, in general, full matrices. In this case, the error model is named leaky since crosstalk may be present between the measurement channels, and the number of error coefficients is $U_L = 4N^2 - 1$; the -1 is due to normalization [29]. A partially leaky error model imposes more restrictive conditions to the crosstalk, and may model more effectively many actual on-wafer measurement set-ups. The number of error coefficients is reduced, but still $U_{PL} = O(N^2)$ [31].

Typically, the crosstalk is negligible and non-leaky error models are used. This leads to a sensible reduction of the error coefficients number, as the matrices \boldsymbol{H} , \boldsymbol{L} , \boldsymbol{M} and \boldsymbol{K} become diagonal, and the number of error coefficients becomes $U_{NL} = 4N-1$ [29,32]. Therefore, the two measured waves at each port uniquely depend on the actual incident and reflected waves at the same port, and the error model can be rewritten in a scalar form as

$$a_i = -h_i a_{mi} + l_i b_{mi} \tag{2.5}$$

$$b_i = -m_i a_{mi} + k_i b_{mi} \tag{2.6}$$

where i is the port number and h_i , l_i , m_i , k_i are the error coefficients (the diagonal ones).

2.2.2 Reduced hardware architecture – Multistate error model

The complete hardware architecture is the multiport extension of the two-port four-sampler VNA. As such, it has great advantages during the system calibration. Any two-port calibration can be performed between any couple of ports, and different

two-port calibrations can be mixed together to accomplish the multiport calibration problem [32, 33].

Simplified hardware solutions, with less than 2N measurement channels, are attractive, though. In first place, a substantial cost reduction is achieved. As a by-product, the measurement signal-to-noise ratio may be increased due to lower attenuation along the signal paths, since the signal goes through less components.

The number of incident wave measuring channels can be set less to the number of ports $(M_A < N)$, as sketched in Fig. 2.3. The reflected waves should be measured with a complete set of directional couplers, so $M_B = N$. In this case, the incident

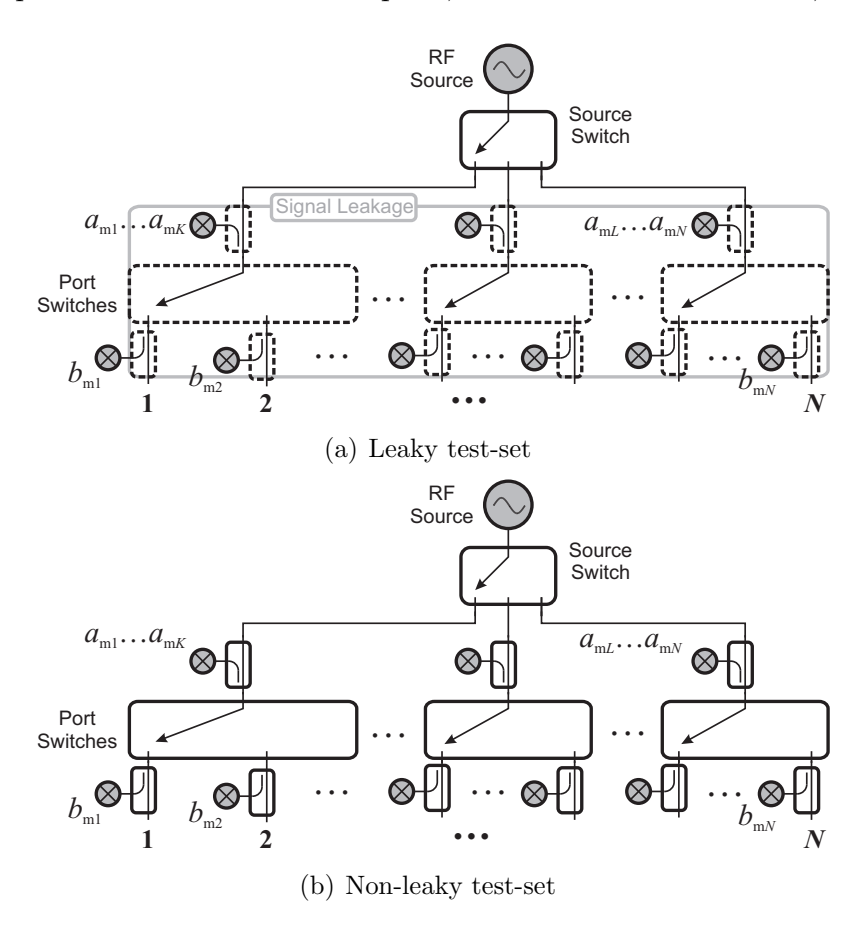


Figure 2.3. Generic reduced hardware multiport test-set. $M_A < N$ channels measure the incident waves, while $M_B = N$ read the reflected waves.

wave channels are shared between groups of ports by a multi-throw RF switch (the port switch). The minimum number of a channels is $M_A = 1$, since in the one-port case, the reflectometer needs two channels.

Both the leaky and non-leaky architectures have a number of measuring channels

which is $M_A + M_B < 2N$. The total number of measurements is thus $M = (M_A + M_B)N < 2N^2$.

The fundamental difference from the traditional multiport VNA error model is the presence of switches (the *port switches*) in between the incident and reflected waves couplers. For a correct modeling, one should consider that the port switches vary their port match from position to position. Thus, the error model has to account for the state changes, so the model is called *multistate*.

Moreover, the number of error coefficients depends on the number of port switch states, which will be named P. The number of switch combinations is very high, theoretically. As example, if the VNA has two a-wave measuring channels ($M_A = 2$), and the two port switches have three trows each (the number of ports is thus $N = 3 \cdot 2 = 6$), the port switches can toggle in up to $3 \cdot 3 = 9$ different combinations. A good design choice is thus to define a switching sequence in order to minimize the switch states number P. As there are N ports, P is in practice limited to N, since there is no practical reason to set the port switches in more than N predefined positions. The absolute minimum is reached when $M_A = N$, since no port switch is present and thus P = 1. This corresponds to the complete hardware architecture model.

The multistate error model defines a linear relationship between the actual and measured waves for each port state $p = 1 \dots P$:

$$\begin{bmatrix} \mathbf{a}^{(p)} \\ \mathbf{b}^{(p)} \end{bmatrix} = \begin{bmatrix} -\mathcal{H}^{(p)} & \mathcal{L}^{(p)} \\ -\mathcal{M}^{(p)} & \mathcal{K}^{(p)} \end{bmatrix} \begin{bmatrix} \mathbf{a}_{m}^{(p)} \\ \mathbf{b}_{m}^{(p)} \end{bmatrix},$$
(2.7)

where $\mathcal{H}^{(p)}$, $\mathcal{L}^{(p)}$, $\mathcal{M}^{(p)}$ and $\mathcal{K}^{(p)}$ are full matrices of dimension

$$\mathcal{H}^{(p)} \longrightarrow (N \times M_A)$$
 $\mathcal{L}^{(p)} \longrightarrow (N \times N)$
 $\mathcal{M}^{(p)} \longrightarrow (N \times M_A)$
 $\mathcal{K}^{(p)} \longrightarrow (N \times N).$

In this way, P independent error models, one for each switch position, are defined. Furthermore, each error model can be normalized independently to the others.

Leaky error model

The leakage requires that $\mathcal{H}^{(p)}$, $\mathcal{L}^{(p)}$, $\mathcal{M}^{(p)}$ and $\mathcal{K}^{(p)}$ are full matrices. Therefore, each state is associated with $2 \cdot NM_A + 2 \cdot NN - 1$ error coefficients, where the "-1" is due to normalization. This leads to a total number of unknowns

$$U_L = (2NM_A + 2N^2 - 1)P. (2.8)$$

When $M_A = N$ it becomes P = 1 and $U_L = 4N^2 - 1$, as in the complete hardware model.

Non-leaky error model

In this case, no crosstalk between the measuring channels and no leakage in the switches is present. Thus, the overall number of error coefficients is drastically reduced, since each measured wave is linearly related only to the physical waves at the same port. This implies that most of the elements of $\mathcal{H}^{(p)}$, $\mathcal{L}^{(p)}$, $\mathcal{M}^{(p)}$ and $\mathcal{K}^{(p)}$ are zero:

$$\mathcal{H}_{ij}^{(p)} = \begin{cases} \mathcal{H}_{ii}^{(p)} & i = j \\ 0 & i \neq j \end{cases} \longrightarrow M_A \text{ error coefficients}$$
 (2.9)

$$\mathcal{L}_{ij}^{(p)} = \begin{cases}
\mathcal{L}_{ii}^{(p)} & i = j \\
0 & i \neq j
\end{cases} \longrightarrow N \text{ error coefficients}$$
(2.10)

$$\mathcal{M}_{ij}^{(p)} = \begin{cases} \mathcal{M}_{ii}^{(p)} & i = j \\ 0 & i \neq j \end{cases} \longrightarrow M_A \text{ error coefficients}$$
 (2.11)

$$\mathcal{K}_{ij}^{(p)} = \begin{cases}
\mathcal{K}_{ii}^{(p)} & i = j \\
0 & i \neq j
\end{cases} \longrightarrow N \text{ error coefficients.}$$
(2.12)

(2.13)

Thus, the number of error coefficients per state becomes $2 \cdot N + 2 \cdot M_A - 1$, due to normalization. The overall number of error coefficients becomes

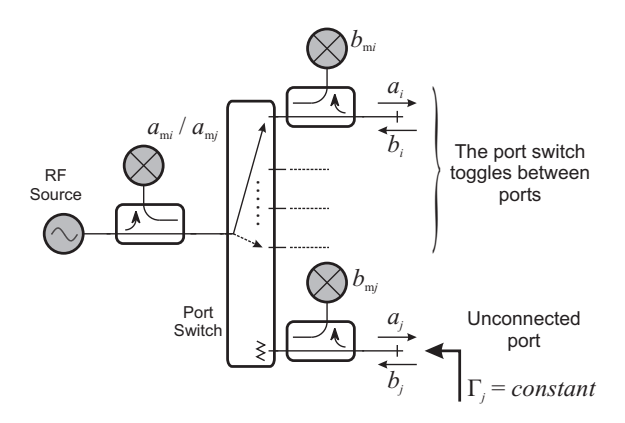
$$U_{NL} = (2N + 2M_A - 1)P. (2.14)$$

The usual $U_{NL} = 4N - 1$ calibration coefficients is found for the complete hardware model, where $M_A = N$ and P = 1.

Multiport (N+1)-samplers network analyzers have been introduced to address the low-cost target. In this case, $M_A = 1$ and thus P = N. This class can be regarded as an extension of the two-port three-samplers VNA. As with the threesamplers network analyzers, the multiport (N+1)-samplers ones are constrained to rigid calibration schemes in order to compute the $U_{NL} = 2N^2 + N$ calibration coefficients. This problem was addressed by Heuermann with the GSOLT calibration, where only perfectly known standards are used [34]. This seriously reduces the on-wafer applications, as these are better suited to partially known standards.

2.2.3 Reduced hardware architecture – Two-state error model

The multistate non-leaky model can be drastically simplified and reduced in the number of error coefficients with a careful analysis. In particular, if the port switches are repeatable, the absence of leakage implies that the non-connected ports' match remains constant, independently on the switch position. That is to say, if one port is not connected by its port switch, the reflection coefficient, looking into that VNA port, is independent on what happens on the other ports, as Fig. 2.4 sketches.



The port match independence of the unconnected port.

In practice, this is easily satisfied, and two hardware states can be defined:

State A, the signal source is connected to port i, thus both the incident and reflected waves can be measured. The same error model as the complete hardware architecture holds in this case, namely equations (2.5) and (2.6).

State B, the signal source is not connected to port j, and only the reflected wave $(b_{\rm m})$ can be measured. In this case, the following holds [35]:

$$a_j = g_j \hat{b}_{mj}$$

$$b_j = f_j \hat{b}_{mj}.$$

$$(2.15)$$

$$(2.16)$$

$$b_j = f_j \hat{b}_{mj}. (2.16)$$

Alternatively, a_j could be derived from b_j knowing the VNA port j reflection coefficient $\Gamma_j = g_j/f_j$, which remains constant independently on the switch position.

Figure 2.5 illustrates the model basics.

The crucial difference with the multistate error model is that the former P calibration models are not independent anymore. A unique model is used, with a single normalization. The total two-state error coefficient number becomes

$$U_{AB} = 6N - 1. (2.17)$$

Interestingly, the N=2 ports case is a degenerate configuration. $U_{AB}=11$ unknowns are predicted, against the well-known ten-term error model [36]. The missing term is due to a further normalization that apply only in the two-port case [35]. The detailed discussion is carried out in Section 2.3.2.

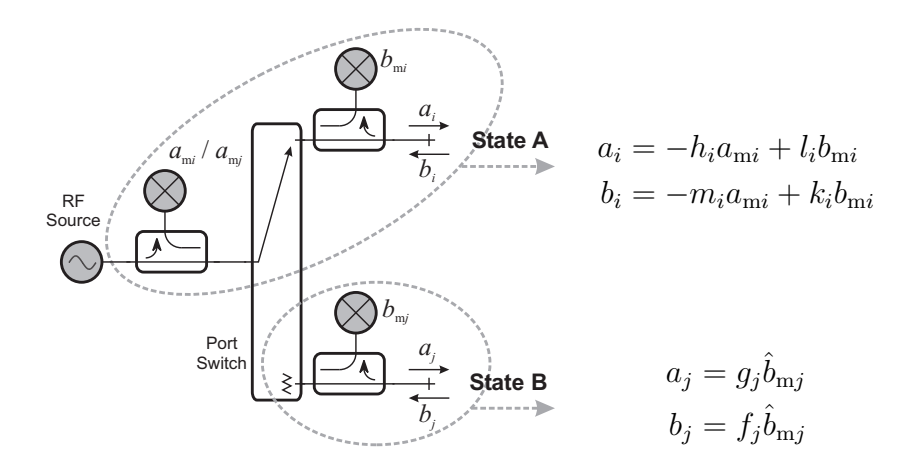


Figure 2.5. Two-state error model.

2.3 Non-leaky two-state multiport calibration

The state A and state B error model equations can be written in matrix form as

$$\boldsymbol{a} = \boldsymbol{L}\boldsymbol{b}_{\mathrm{m}} - \boldsymbol{H}\boldsymbol{a}_{\mathrm{m}} \tag{2.18}$$

$$\boldsymbol{b} = \boldsymbol{K}\boldsymbol{b}_{\mathrm{m}} - \boldsymbol{M}\boldsymbol{a}_{\mathrm{m}} \tag{2.19}$$

$$\boldsymbol{a} = \boldsymbol{G}\hat{\boldsymbol{b}}_{m} \tag{2.20}$$

$$\boldsymbol{b} = \boldsymbol{F}\hat{\boldsymbol{b}}_{m} \tag{2.21}$$

where the matrices \boldsymbol{H} , \boldsymbol{L} , \boldsymbol{M} , \boldsymbol{K} , \boldsymbol{F} and \boldsymbol{G} are diagonal, respectively containing the h_i , l_i , m_i , k_i , f_i and g_i error coefficients, (2.18) and (2.19) are the same equations as (2.3) and

$$\hat{\boldsymbol{b}}_{\mathrm{m}} = \begin{bmatrix} \hat{b}_{\mathrm{m}1} \\ \hat{b}_{\mathrm{m}2} \\ \vdots \\ \hat{b}_{\mathrm{m}N} \end{bmatrix}. \tag{2.22}$$

Due to the state independence, the measured wave vectors contain non-zero elements only in specific places. For example, if the signal source drives port 1, it becomes:

$$\boldsymbol{a}_{\mathrm{m}} = \begin{bmatrix} a_{\mathrm{m}1} \\ 0 \\ \vdots \\ 0 \end{bmatrix}, \quad \boldsymbol{b}_{\mathrm{m}} = \begin{bmatrix} b_{\mathrm{m}1} \\ 0 \\ \vdots \\ 0 \end{bmatrix}, \quad \hat{\boldsymbol{b}}_{\mathrm{m}} = \begin{bmatrix} 0 \\ \hat{b}_{\mathrm{m}2} \\ \vdots \\ \hat{b}_{\mathrm{m}N} \end{bmatrix}. \tag{2.23}$$

Port 1 is in state A, thus only a_{m1} and b_{m1} can be measured. Instead, the remaining ports are in state B, so \hat{b}_{mi} are measured with $i = 2 \dots N$.

Connecting the RF source to all the ports and stacking the results, the following measured waves matrices are found in state A

$$\mathbf{A}_{m} = \begin{bmatrix} a_{m1,1} & 0 \\ & \ddots & \\ 0 & a_{mN,N} \end{bmatrix}, \mathbf{B}_{m} = \begin{bmatrix} b_{m1,1} & 0 \\ & \ddots & \\ 0 & b_{mN,N} \end{bmatrix},$$
(2.24)

where $a_{mi,s}$ is the a_{mi} wave with signal source to port s, while for state B it follows that

$$\hat{\boldsymbol{B}}_{m} = \begin{bmatrix} 0 & \hat{b}_{m1,2} & \dots & \hat{b}_{m1,N} \\ \hat{b}_{m2,1} & 0 & \ddots & \vdots \\ \vdots & \ddots & \ddots & \hat{b}_{mN-1,N} \\ \hat{b}_{mN,1} & \dots & \hat{b}_{mN,N-1} & 0 \end{bmatrix}.$$
(2.25)

The actual waves' matrices are then found as

state A:
$$\hat{A} = LB_{\rm m} - HA_{\rm m}$$
 $\hat{B} = KB_{\rm m} - MA_{\rm m}$ (2.26)
state B: $\hat{A} = G\hat{B}_{\rm m}$ $\hat{B} = F\hat{B}_{\rm m}$, (2.27)

state B:
$$\hat{A} = G\hat{B}_{\mathrm{m}}$$
 $\hat{B} = F\hat{B}_{\mathrm{m}}$, (2.27)

thus

$$\tilde{\mathbf{A}} = \begin{bmatrix} l_1 b_{m1,1} - h_1 a_{m1,1} & 0 \\ & \ddots & \\ 0 & & l_N b_{mN,N} - h_N a_{mN,N} \end{bmatrix}$$
(2.28)

$$\tilde{\mathbf{B}} = \begin{bmatrix} k_1 b_{\text{m1,1}} - m_1 a_{\text{m1,1}} & 0 \\ & \ddots & \\ 0 & k_N b_{\text{mN,N}} - m_N a_{\text{mN,N}} \end{bmatrix}$$
(2.29)

$$\tilde{\mathbf{A}} = \begin{bmatrix}
l_1 b_{m1,1} - h_1 a_{m1,1} & 0 \\
 & \ddots & \\
 & 0 & l_N b_{mN,N} - h_N a_{mN,N}
\end{bmatrix} (2.28)$$

$$\tilde{\mathbf{B}} = \begin{bmatrix}
k_1 b_{m1,1} - m_1 a_{m1,1} & 0 \\
 & \ddots & \\
 & 0 & k_N b_{mN,N} - m_N a_{mN,N}
\end{bmatrix} (2.29)$$

$$\hat{\mathbf{A}} = \begin{bmatrix}
0 & f_1 \hat{b}_{m1,2} & \cdots & f_1 \hat{b}_{m1,N} \\
f_2 \hat{b}_{m2,1} & 0 & \ddots & \vdots \\
 & \vdots & \ddots & \ddots & f_{N-1} \hat{b}_{mN-1,N} \\
f_N \hat{b}_{mN,1} & \cdots & f_N \hat{b}_{mN,N-1} & 0
\end{bmatrix} (2.30)$$

$$\hat{\mathbf{B}} = \begin{bmatrix}
0 & g_1 \hat{b}_{m1,2} & \cdots & g_1 \hat{b}_{m1,N} \\
g_2 \hat{b}_{m2,1} & 0 & \ddots & \vdots \\
 & \vdots & \ddots & \ddots & g_{N-1} \hat{b}_{mN-1,N} \\
g_N \hat{b}_{mN,1} & \cdots & g_N \hat{b}_{mN,N-1} & 0
\end{bmatrix} (2.31)$$

$$\hat{\boldsymbol{B}} = \begin{bmatrix} 0 & g_1 b_{m1,2} & \dots & g_1 b_{m1,N} \\ g_2 \hat{b}_{m2,1} & 0 & \ddots & \vdots \\ \vdots & \ddots & \ddots & g_{N-1} \hat{b}_{mN-1,N} \\ g_N \hat{b}_{mN,1} & \dots & g_N \hat{b}_{mN,N-1} & 0 \end{bmatrix}.$$
(2.31)

It can be noted that the matrix couples \hat{A} , \hat{B} and \hat{A} , \hat{B} are element-wise independent. Both express the incident and reflected waves state at the DUT ports: the first one describes the ports in state A, the latter the state B ports. Since both models should map the same waves state (B = SA), the following conditions should hold

$$\mathbf{A} = \tilde{\mathbf{A}} + \hat{\mathbf{A}} \tag{2.32}$$

$$\boldsymbol{B} = \tilde{\boldsymbol{B}} + \hat{\boldsymbol{B}}. \tag{2.33}$$

In practice, the state A and state B measurement channels can be regarded as two different cameras. Both are pointed to the same landscape, but the first one focuses only a small part of it (the diagonal). The remaining part is focused by the second camera. Since the landscape is the same, its picture can be obtained by the superposition of the two subsets.

Finally, the calibration equation is found from (2.26), (2.27), (2.32) and (2.33) as [35]

$$KB_{\rm m} - MA_{\rm m} + F\hat{B}_{\rm m} = S(LB_{\rm m} - HA_{\rm m} + G\hat{B}_{\rm m}).$$
 (2.34)

The calibration equation reduces to the complete hardware model one if no state B ports are present $(M_A = N, P = 1)$:

$$KB_{\rm m} - MA_{\rm m} = S(LB_{\rm m} - HA_{\rm m}), \qquad (2.35)$$

which was originally published in [29] as

$$KS_{\rm m} - M = S(LS_{\rm m} - H), \tag{2.36}$$

having set $S_{\rm m} = B_{\rm m} A_{\rm m}^{-1}$, which is the usual procedure for the switch error correction, as will be shown in Section 2.4.

2.3.1 General multiport formulation for the error coefficients computation

Let us consider the error coefficients not normalized, so that the calibration problem consists of 6N unknowns. In order to solve for the 6N error coefficients h_i , l_i , m_i , k_i , f_i and g_i , the calibration equation (2.34) should be rewritten in a scalar form. A N-port standard S gives a linear system of N^2 equations in 6N unknowns like

$$-\sum_{p=1}^{N} (1 - \delta_{pj}) S_{ip} g_p \hat{b}_{mp,j} + (1 - \delta_{ij}) f_i \hat{b}_{mi,j} - S_{ij} l_j b_{mj,j} + + \delta_{ij} k_i b_{mi,j} + S_{ij} h_j a_{mj,j} - \delta_{ij} m_i a_{mi,j} = 0 (i = 1 ... N, j = 1 ... N).$$
(2.37)

The measurements of multiple N-port standards, belonging to a proper calibration sequence, can be stacked together to form an homogeneous system

$$Cu = 0 (2.38)$$

where the 6N unknowns' vector is

$$u = \begin{bmatrix} -\operatorname{diag}(\boldsymbol{H}) \\ \operatorname{diag}(\boldsymbol{L}) \\ \operatorname{diag}(\boldsymbol{G}) \\ -\operatorname{diag}(\boldsymbol{M}) \\ \operatorname{diag}(\boldsymbol{K}) \\ \operatorname{diag}(\boldsymbol{F}) \end{bmatrix}.$$
 (2.39)

The trivial solution (u = 0) is obviously rejected. In order to find a non-trivial solution, the error coefficients have to be normalized. The usual choice is to normalize by k_1 , this leads to a set of 6N - 1 coefficients

$$\frac{h_i}{k_1}, \frac{l_i}{k_1}, \frac{m_i}{k_1}, \frac{k_i}{k_1}, \frac{f_i}{k_1}, \frac{g_i}{k_1}$$
 $(i = 1, \dots, N).$

After that, the system (2.38) can be written as

$$Nu' = n \tag{2.40}$$

where $n \neq 0$ is the column of C corresponding to k_1 , and N is the remaining part of C. The 6N-1 normalized error coefficients in u' can be computed either by elimination or in the least-squares sense.

An alternative approach is to find a basis for the non-trivial solution (i.e. the null space of C) directly from (2.38) by singular-value decomposition, and then imposing the normalization $k_1 = 1$ to the solution vector.

2.3.2 Multiport calibration using one-port and two-port standards

The possibility of using commercially-available one- and two-ports standards during the multiport VNA calibration is very attractive in a two-states hardware. The goal is to dynamically merge different two-ports techniques to suit the user's calibration constraints.

General criteria were found by Ferrero and Sampietro for the complete hardware architecture [30]. These criteria cannot be applied in a (N+1)-samplers VNA since they rely on a complete set of reflectometers during the measurement of a two-port standard. Nevertheless, this condition could be met sometimes if the number of

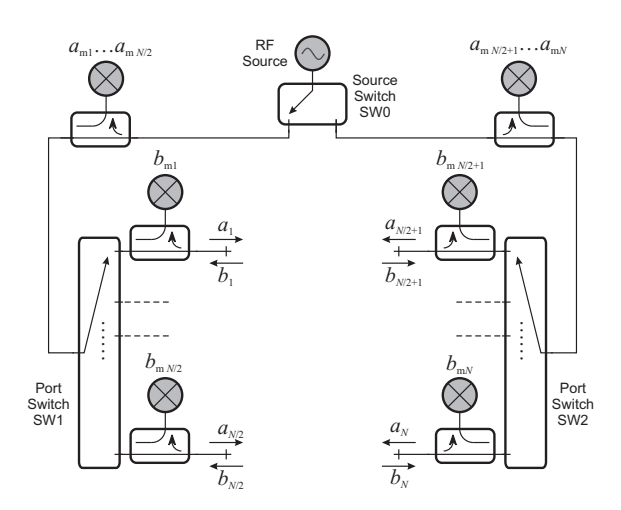


Figure 2.6. The (N+2)-samplers two-state hardware architecture.

incident-wave receivers is increased. A particularly convenient hardware configuration uses a two-state architecture with (N+2) measurement channels, thus $M_A = 2$. An example of this VNA system is sketched in Fig. 2.6.

Commercially-available test-sets were introduced only recently [5]. The test-set is divided into two banks, providing high symmetry. Moreover, good modularity is achieved, since a conventional two-port VNA contains the source and incident waves readings, while an extension box includes the port switches and the reflected waves couplers (see Fig. 2.7).

Both the left and the right bank have one port that can be set in state A. Thus, there are couples of ports that can be set in state A at the same time, and any common two-port calibration can be performed at these ports couples.

A convenient solution to the multiport calibration problem is not directly based on the calibration system (2.40). Instead, one- or two-port calibration problems are first locally performed at groups of ports, then the different groups are merged together [37]. Two four-port examples are sketched in Fig. 2.8, both lead to a consistent calibration. The first group (port 1 on the left bank and port 3 on the right one) is calibrated by a LRM [38] procedure. The second (ports 2 and 4) uses a QSOLT [39] calibration. The two groups are merged together by a unknown thru calibration [40].

The problem of finding a consistent multiport calibration sequence has been treated for the complete hardware model in [30] and [32]. The results can be applied in a two-state architecture, provided that the measurements are performed with both ports in state A.

A general treatment that combines both state A and state B measurements is



Figure 2.7. The 12-port (N+2)-samplers Anritsu 37397D VNA has 40 MHz to 67 GHz frequency range. The system consists of a 37000D-family two-port VNA (top) coupled to an extension box (bottom) that contains the port switches and auxiliary power supplies. The measurement couplers are contained in six modules (two port each), which are placed as close as possible to the DUT in order to minimize high-frequency losses. The measurement and calibration software runs on an external computer. Courtesy of Anritsu [5].

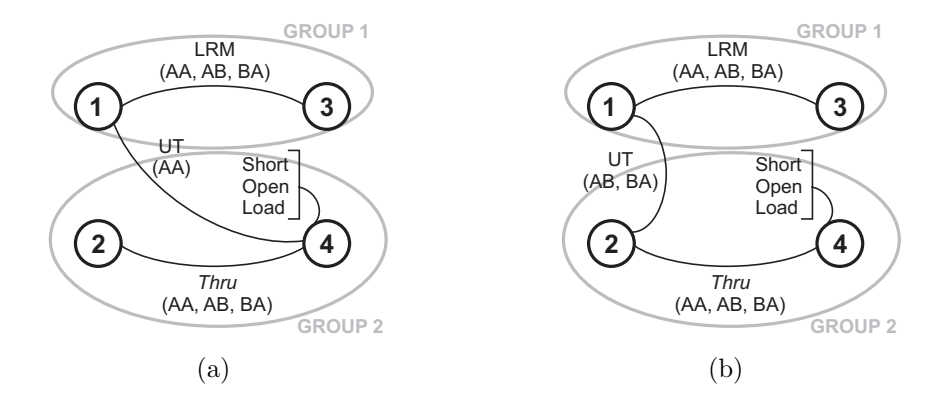


Figure 2.8. Possible calibration scheme for a four-port two-state network analyzer. (a) Unknown *thru* in the AA case, the same of a complete hardware architecture.

(b) Unknown thru in the AB case.

still lacking. However, as a matter of facts, its usefulness is more theoretical than practical, as the user can arrange the ports in order to perform the key two-port calibrations with both ports in state A (case AA), while the state B measurements

(cases AB and BA) can be used to merge previously calibrated groups of ports. To this purpose, three core problems are addressed:

- 1. how to calibrate a couple of ports using a two-port calibration to compute both the state A and the state B error coefficients;
- 2. how to merge an uncalibrated port to a calibrated group using a fully known two-port standard;
- 3. how to merge together two independently calibrated groups using an unknown but reciprocal two-port standard.

For ease of notation, the error model equations are rewritten as

state A:
$$\begin{bmatrix} a_i \\ b_i \end{bmatrix} = \mathbf{E}_i \begin{bmatrix} a_{\text{m}i} \\ b_{\text{m}i} \end{bmatrix} \qquad \mathbf{E}_i = \begin{bmatrix} -h_i & l_i \\ -m_i & k_i \end{bmatrix}$$
(2.41) state B:
$$\begin{bmatrix} a_j \\ b_j \end{bmatrix} = \mathbf{e}_j \hat{b}_{\text{m}j} \qquad \mathbf{e}_j = \begin{bmatrix} g_j \\ f_j \end{bmatrix}$$
(2.42)

and, in the examples, a eight port (N + 2)-samplers two-state VNA will be used: ports 1, 2, 3 and 4 belong to the left bank and ports 5, 6, 7 and 8 to the right one.

One and Two-port calibrations

The two-port calibration is performed between between ports x and y, both can be set in state A (Fig. 2.9). In case AA, the problem reduces to that of a two-port

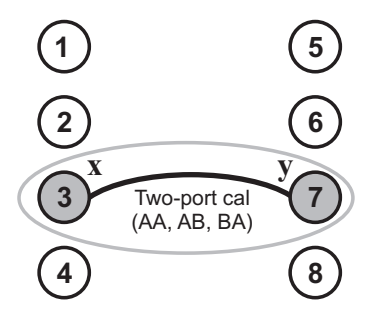


Figure 2.9. Example of two-port calibration.

four sampler VNA architecture (Fig. 2.10(a)), while in the AB/BA cases it becomes a three samplers architecture (forward/reverse case, respectively, Fig. 2.10(b)). In the first case, it is well known that any two-port calibration¹ can be performed, even

¹Possible choices are, for instance, thru-short-delay (TSD) [41], thru-reflect-line (TRL) [42], multiline TRL [43], line-reflect-match (LRM) [38], line-short-match (LSM) [38], short-open-load-thru (SOLT) [44], quick SOLT (QSOLT) [39] or short-open-load-reciprocal (SOLR) [40].

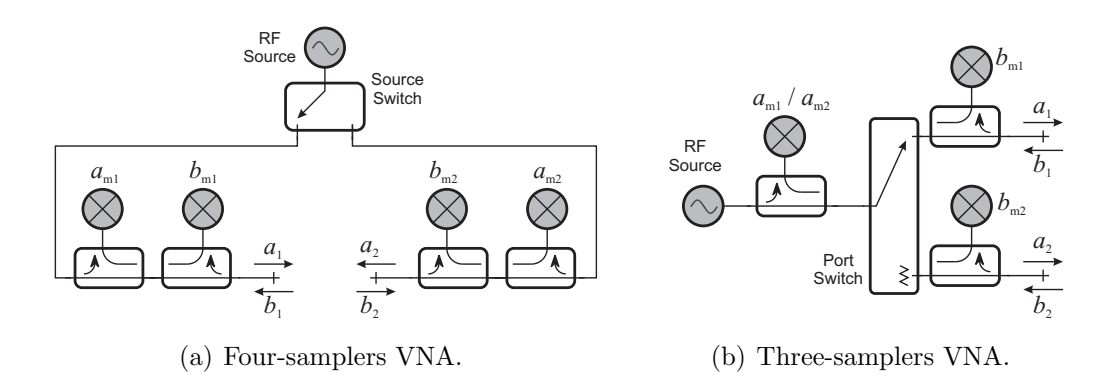


Figure 2.10. Two-port VNA architectures.

employing partially known standards. Therefore, seven calibration coefficients can be solved, so, assuming that k_x is chosen as the two-port calibration normalization, the state A coefficients h_x/k_x , l_x/k_x , m_x/k_x and h_y/k_x , k_y/k_x , l_y/k_x , m_y/k_x are obtained.

The same considerations apply in the case of a one port calibration at port x, where the three state A coefficients h_x/k_x , l_x/k_x , m_x/k_x can be solved by measuring three known different standards.

However, the state B error coefficients f_x/k_x and g_x/k_x can be computed only by the measurement of a two-port device. Let its transmission matrix be

$$\begin{bmatrix} b_x \\ a_x \end{bmatrix} = \mathbf{T} \begin{bmatrix} a_y \\ b_y \end{bmatrix}, \quad \mathbf{T} = \frac{1}{S_{yx}} \begin{bmatrix} S_{xy}S_{yx} - S_{xx}S_{yy} & S_{xx} \\ -S_{yy} & 1 \end{bmatrix}$$
(2.43)

where S_{ij} are the device's scattering-parameters.

When the standard is measured with both ports in state A (case AA), the following holds

$$\boldsymbol{X}\frac{\boldsymbol{E}_{x}}{k_{x}}\begin{bmatrix} a_{\text{m}x} \\ b_{\text{m}x} \end{bmatrix} = \boldsymbol{T}\frac{\boldsymbol{E}_{y}}{k_{x}}\begin{bmatrix} a_{\text{m}y} \\ b_{\text{m}y} \end{bmatrix}, \qquad (2.44)$$

being $\boldsymbol{X} = \begin{bmatrix} 0 & 1 \\ 1 & 0 \end{bmatrix}$ a 2 × 2 permutation matrix. Switching the RF source signal drive from port x to port y allows to stack (2.44) as

$$\boldsymbol{X} \frac{\boldsymbol{E}_{x}}{k_{x}} \begin{bmatrix} a_{\text{mx},x} & a_{\text{mx},y} \\ b_{\text{mx},x} & b_{\text{mx},y} \end{bmatrix} = \boldsymbol{T} \frac{\boldsymbol{E}_{y}}{k_{x}} \begin{bmatrix} a_{\text{my},x} & a_{\text{my},y} \\ b_{\text{my},x} & b_{\text{my},y} \end{bmatrix}$$
(2.45)

where $a_{mx,s}$ indicates a_{mx} measured with RF drive through port s. Equation (2.45) can be used to compute the state A error coefficients at port y from the measurement of a known two-port standard and from the knowledge of the port x state A error

coefficients as

$$\frac{\boldsymbol{E}_{y}}{k_{x}} = \boldsymbol{T}^{-1} \boldsymbol{X} \frac{\boldsymbol{E}_{x}}{k_{x}} \begin{bmatrix} a_{\text{mx},x} & a_{\text{mx},y} \\ b_{\text{mx},x} & b_{\text{mx},y} \end{bmatrix} \begin{bmatrix} a_{\text{my},x} & a_{\text{my},y} \\ b_{\text{my},x} & b_{\text{my},y} \end{bmatrix}^{-1}$$
(2.46)

This is the case, for example, of the QSOLT calibration, where a one-port calibration determines the port x state A coefficients, and the measurement of a thru device completes the calibration in case AA [39].

Toggling port y in state B while port x remains in state A (case AB) and measuring a two-port standard gives two additional equations:

$$T\frac{e_y}{k_x}\hat{b}_{my,x} = X\frac{E_x}{k_x} \begin{bmatrix} a_{mx,x} \\ b_{mx,x} \end{bmatrix}.$$
 (2.47)

The two-port transmission matrix T is known, either from the standard definition, or by a previous measurement in case AA if the two-port device is only partially known. Thus, the port y state B calibration coefficients can be computed as

$$\begin{bmatrix} g_y/k_x \\ f_y/k_x \end{bmatrix} = \frac{1}{\hat{b}_{mu,x}} \mathbf{T}^{-1} \mathbf{X} \begin{bmatrix} -h_x/k_x & l_x/k_x \\ -m_x/k_x & 1 \end{bmatrix} \begin{bmatrix} a_{mx,x} \\ b_{mx,x} \end{bmatrix}$$
(2.48)

Similarly, the BA case leads to two additional equations in e_x and E_y :

$$Xe_x\hat{b}_{\mathrm{m}x,y} = TE_y \begin{bmatrix} a_{\mathrm{m}y,y} \\ b_{\mathrm{m}y,y} \end{bmatrix},$$
 (2.49)

from which, the port x calibration coefficients become

$$\begin{bmatrix} g_x/k_x \\ f_x/k_x \end{bmatrix} = \frac{1}{\hat{b}_{\text{m}x,y}} \mathbf{X} \mathbf{T} \begin{bmatrix} -h_y/k_x & l_y/k_x \\ -m_y/k_x & k_y/k_x \end{bmatrix} \begin{bmatrix} a_{\text{m}y,y} \\ b_{\text{m}y,y} \end{bmatrix}.$$
(2.50)

In conclusion, except for the normalization constant k_x , all the calibration coefficients at ports x and y can be computed by a two-port calibration, provided that case AA is feasible.

A final remark should regard the special case of a two-port VNA based on four samplers, which can be operated either as a real four-samplers VNA (case AA, Fig. 2.10(a)), or as a three samplers one (cases AB/BA, Fig. 2.10(b)) if one reading is omitted. As well known, the four samplers VNA is described by the eight-term error model, while the three samplers one uses the twelve-term error model, or the ten-term if crosstalk is omitted [36]. The number of error coefficients predicted by the two-state model is instead 6N - 1 = 11, but it can be shown that a further normalization can reduce it to ten [35], if only measurements in cases AB/BA are of interest.

During the measurement in the AB, or forward, case, (2.48) holds, while (2.50) regards the measurement in the BA, or reverse, case. The two equations involve 11 terms, but actually they are coupled only by the normalization factor $1/k_x$. As (2.50) is invariant to multiplication of the left and right sides by a common non-zero parameter, one can multiply by k_x/k_y , thus eliminating one error coefficient:

$$\begin{bmatrix} g_x/k_y \\ f_x/k_y \end{bmatrix} = \frac{1}{\hat{b}_{\text{mx},y}} \mathbf{X} \mathbf{T} \begin{bmatrix} -h_y/k_y & l_y/k_y \\ -m_y/k_y & 1 \end{bmatrix} \begin{bmatrix} a_{\text{my},y} \\ b_{\text{my},y} \end{bmatrix}$$
(2.51)

Therefore, in the forward and reverse measurements, only ten error coefficients are involved:

$$\frac{h_x}{k_x}$$
, $\frac{l_x}{k_x}$, $\frac{m_x}{k_x}$, $\frac{f_x}{k_x}$, $\frac{g_x}{k_x}$ and $\frac{h_y}{k_y}$, $\frac{l_y}{k_y}$, $\frac{m_y}{k_y}$, $\frac{f_y}{k_y}$, $\frac{g_y}{k_y}$,

which can be easily mapped onto the ten-term model formulation, as shown in [35].

Merging an uncalibrated port by means of a known device

A known two-port device, measured in cases AA and AB, is enough to merge an uncalibrated port y to a previously calibrated group of ports. The group includes port x, and has been calibrated using k_x as normalization constant (Fig. 2.11).

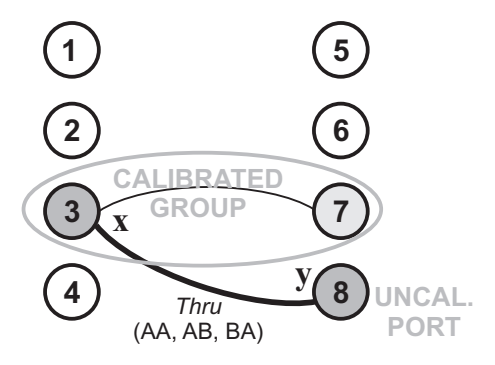


Figure 2.11. Example of merging strategy using a known standard.

A known two-port device is connected between ports x and y, and, from (2.45), its AA measurement is used to compute the port y state A coefficients as

$$\frac{\boldsymbol{E}_{y}}{k_{x}} = \boldsymbol{T}^{-1} \boldsymbol{X} \frac{\boldsymbol{E}_{x}}{k_{x}} \begin{bmatrix} a_{\text{m}x,x} & a_{\text{m}x,y} \\ b_{\text{m}x,x} & b_{\text{m}x,y} \end{bmatrix} \begin{bmatrix} a_{\text{m}y,x} & a_{\text{m}y,y} \\ b_{\text{m}y,x} & b_{\text{m}y,y} \end{bmatrix}^{-1}.$$
 (2.52)

When port y is in state B (case AB), the state B error coefficients are computed using (2.48).

Merging two subsets by means of a unknown reciprocal device

Previous calibrations have determined two calibrated subsets, one is normalized by k_x , the other by k_y . A reciprocal (unknown thru) device is connected between ports x and y, and the two sets should be merged with unique normalization constant k_x (Fig. 2.12).

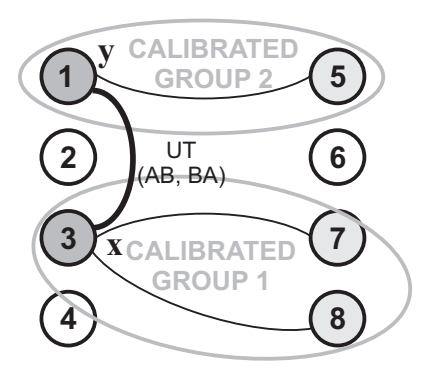


Figure 2.12. Example of merging strategy using a unknown reciprocal standard.

The AA case is trivial, being the same of a two-port VNA [40].

The AB and BA cases are instead of great interest, since they allow to perform an unknown thru within the same port bank. From (2.47) and (2.49) the following holds

$$\boldsymbol{T}\frac{\boldsymbol{e}_{y}}{k_{y}}\hat{b}_{\mathrm{m}y,x} = \begin{pmatrix} k_{x} \\ k_{y} \end{pmatrix} \boldsymbol{X}\frac{\boldsymbol{E}_{x}}{k_{x}} \begin{bmatrix} a_{\mathrm{m}x,x} \\ b_{\mathrm{m}x,x} \end{bmatrix}$$
(2.53)

$$T\frac{E_y}{k_y} \begin{bmatrix} a_{\text{m}y,y} \\ b_{\text{m}y,y} \end{bmatrix} = \left(\frac{k_x}{k_y}\right) X\frac{e_x}{k_x} \hat{b}_{\text{m}x,y}$$
 (2.54)

where the unknown to be computed is k_x/k_y . Stacking together (2.53) and (2.54) leads to

$$TM_y = \left(\frac{k_x}{k_y}\right) XM_x \tag{2.55}$$

where M_y and M_x are fully known

$$\mathbf{M}_{y} = \begin{bmatrix} \frac{\mathbf{e}_{y}}{k_{y}} \hat{b}_{\mathrm{m}y,x} & \frac{\mathbf{E}_{y}}{k_{y}} \begin{bmatrix} a_{\mathrm{m}y,y} \\ b_{\mathrm{m}y,y} \end{bmatrix} \end{bmatrix}, \quad \mathbf{M}_{x} = \begin{bmatrix} \frac{\mathbf{E}_{x}}{k_{x}} \begin{bmatrix} a_{\mathrm{m}x,x} \\ b_{\mathrm{m}x,x} \end{bmatrix} & \frac{\mathbf{e}_{x}}{k_{x}} \hat{b}_{\mathrm{m}x,y} \end{bmatrix}. \quad (2.56)$$

The two-port standard reciprocity imposes $\det(\mathbf{T}) = 1$, thus the unknown is found as

$$\frac{k_x}{k_y} = \pm \sqrt{-\frac{\det(\boldsymbol{M}_y)}{\det(\boldsymbol{M}_x)}}$$
 (2.57)

and the sign ambiguity is solved by a prior coarse knowledge of the device's phase.

The AB/BA unknown thru procedure is based on two fully calibrated subsets, *i.e.* both state A and state B error coefficients have been computed. Thus, the procedure fails if the port y subset derives from a one-port calibration, since the port y state B coefficients cannot be determined. As a consequence, this demonstrates that the unknown thru calibration is not directly applicable in a two-port three-samplers VNA.

2.4 Non-leaky two-state multiport de-embedding

After a proper calibration sequence, the 6N-1 error coefficients are found, except for an arbitrary normalization constant $(e.g. k_1)$:

$$\frac{h_i}{k_1}, \frac{l_i}{k_1}, \frac{m_i}{k_1}, \frac{k_i}{k_1}, \frac{f_i}{k_1}, \frac{g_i}{k_1}$$
 $(i = 1 \dots N).$

The calibration equation (2.34) is written as

$$\frac{\mathbf{K}}{k_1}\mathbf{B}_{\mathrm{m}} - \frac{\mathbf{M}}{k_1}\mathbf{A}_{\mathrm{m}} + \frac{\mathbf{F}}{k_1}\hat{\mathbf{B}}_{\mathrm{m}} = \mathbf{S}\left(\frac{\mathbf{L}}{k_1}\mathbf{B}_{\mathrm{m}} - \frac{\mathbf{H}}{k_1}\mathbf{A}_{\mathrm{m}} + \frac{\mathbf{G}}{k_1}\hat{\mathbf{B}}_{\mathrm{m}}\right)$$
(2.58)

and the N-port scattering matrix is computed as (de-embedding equation)

$$S = \left(\frac{\mathbf{K}}{k_1}\mathbf{B}_{\mathrm{m}} - \frac{\mathbf{M}}{k_1}\mathbf{A}_{\mathrm{m}} + \frac{\mathbf{F}}{k_1}\hat{\mathbf{B}}_{\mathrm{m}}\right) \left(\frac{\mathbf{L}}{k_1}\mathbf{B}_{\mathrm{m}} - \frac{\mathbf{H}}{k_1}\mathbf{A}_{\mathrm{m}} + \frac{\mathbf{G}}{k_1}\hat{\mathbf{B}}_{\mathrm{m}}\right)^{-1}$$
(2.59)

from which the well known property that the normalization constant plays no role is evidenced [45], as anticipated in Section 2.1.

While the total number of measurements in the complete hardware model is $2N^2$, the two-state one amounts to M = N(N+1). For each source drive position, N reflected waves and a single incident one are acquired. Thus, the new hardware is cheaper and faster than the traditional one.

Further reduction of N measurements can be done using ratioed measurements, *i.e.* the readings are normalized by the driving port measured incident wave, as anticipated in Section 2.1. In this case, both sides of (2.58) are multiplied by the matrix

$$\mathbf{R} = \mathbf{A}_{\mathbf{m}}^{-1} = \begin{bmatrix} \frac{1}{a_{\mathbf{m}1,1}} & 0 \\ & \ddots & \\ 0 & \frac{1}{a_{\mathbf{m}N,N}} \end{bmatrix}, \tag{2.60}$$

which contains the incident waves readings, leading to

$$S = \left(\frac{K}{k_1} B_{\rm m} A_{\rm m}^{-1} - \frac{M}{k_1} + \frac{F}{k_1} \hat{B}_{\rm m} A_{\rm m}^{-1}\right) \left(\frac{L}{k_1} B_{\rm m} A_{\rm m}^{-1} - \frac{H}{k_1} + \frac{G}{k_1} \hat{B}_{\rm m} A_{\rm m}^{-1}\right)^{-1}, (2.61)$$

where only ratioed measurements, like $b_{\text{m}i,i}/a_{\text{m}i,i}$ or $\hat{b}_{\text{m}j,i}/a_{\text{m}i,i}$, are present.

The same reduction is also possible in the traditional hardware case, and N measurements are spared.

2.4.1 Switch error correction

The peculiarity of the two-states model resides in the switch error correction procedure, which corrects for non perfectly independent signal drives.

The complete hardware model operates the switch error correction to the measured quantities. As originally published in [29], the DUT scattering matrix is computed as

$$\mathbf{S} = \left(\frac{\mathbf{K}}{k_1} \mathbf{S}_{\mathrm{m}} - \frac{\mathbf{M}}{k_1}\right) \left(\frac{\mathbf{L}}{k_1} \mathbf{S}_{\mathrm{m}} - \frac{\mathbf{H}}{k_1}\right)^{-1},\tag{2.62}$$

having set $S_{\rm m} = B_{\rm m} A_{\rm m}^{-1}$, which is the usual procedure for the switch error correction.

In the two-state model, the procedure cannot be applied on the measured waves matrices, due to lack of measurement equations. Instead, the switch correction is performed on the actual waves in the de-embedding equation (2.59).

2.4.2 Accuracy considerations – Comparison with the complete hardware model

Accuracy is always of primary concern. The new hardware architecture is less expensive and faster than the traditional one due to the reduced receiver's channels. Is its measurement accuracy somewhat reduced, too?

A rigorous multiport accuracy analysis is lacking for both the complete hardware model and the two-state one. Actually, the connector repeatability was analyzed by Sanpietro and Ferrero in [46], who focused on the three-port thru loop calibration [47]. The error coefficients uncertainties were estimated from multiple calibration standards' connections, and their effects on the scattering matrix measurement were evaluated.

The overall uncertainty in the DUT scattering matrix, which is sometimes addressed to as *residual uncertainty*, is due to type-B uncertainties in the error coefficients computation and to the measurement noise (type-A uncertainties).

The former depend on the calibration standard definition uncertainty due to mechanical tolerances or imperfect modeling and (mainly) on the particular calibration sequence and technique [48,49]. Moreover, the error coefficients computation is affected by the connectors' repeatability and the instrumentation noise during the standards' measurements.

The propagation of the measurement noise in the final N-port measurement was addressed. To that purpose, the calibration coefficients were considered error-free, and thus the two-state model uncertainty contributions due to the measurement noise are easily derived from the deembedding equation (2.58) as

$$d\mathbf{S} = \left(\left(\frac{\mathbf{K}}{k_1} - \mathbf{S} \frac{\mathbf{L}}{k_1} \right) d\mathbf{B}_{m} - \left(\frac{\mathbf{M}}{k_1} - \mathbf{S} \frac{\mathbf{H}}{k_1} \right) d\mathbf{A}_{m} + \left(\frac{\mathbf{F}}{k_1} - \mathbf{S} \frac{\mathbf{G}}{k_1} \right) d\hat{\mathbf{B}}_{m} \right) \left(\frac{\mathbf{A}}{k_1} \right)^{-1}$$
(2.63)

being $\frac{\mathbf{A}}{k_1} = \frac{\mathbf{L}}{k_1} \mathbf{B}_{\mathrm{m}} - \frac{\mathbf{H}}{k_1} \mathbf{A}_{\mathrm{m}} + \frac{\mathbf{G}}{k_1} \hat{\mathbf{B}}_{\mathrm{m}}$ the incident-waves matrix, which acts as a normalization constant for $\mathrm{d}\mathbf{B}_{\mathrm{m}}$, $\mathrm{d}\mathbf{A}_{\mathrm{m}}$ and $\hat{\mathbf{B}}_{\mathrm{m}}$.

In practice, the measurement noise can be considered independent, white, Gaussian with variance σ :

$$\delta b_{\rm mi} \sim N(0,\sigma), \, \delta a_{\rm mi} \sim N(0,\sigma), \, \delta \hat{b}_{\rm mi} \sim N(0,\sigma) \quad (i=1,\ldots,N)$$
 (2.64)

The noise variance can be easily estimated, as a function of frequency, from the measured background noise. Moreover, in many cases the matrix $\frac{\mathbf{A}}{k_1}$ is diagonal, having the diagonal elements $|A_{ii}|^2 = P_i$ equal to the port i driving power.

The uncertainty propagation equation (2.63) reduces to the following in the complete architecture model:

$$d\mathbf{S} = \left(\left(\frac{\mathbf{K}}{k_1} - \mathbf{S} \frac{\mathbf{L}}{k_1} \right) d\mathbf{B}_{m} - \left(\frac{\mathbf{M}}{k_1} - \mathbf{S} \frac{\mathbf{H}}{k_1} \right) d\mathbf{A}_{m} \right) \left(\frac{\mathbf{A}}{k_1} \right)^{-1}.$$
 (2.65)

In this case, $d\mathbf{B}_{\mathrm{m}}$ and $d\mathbf{A}_{\mathrm{m}}$ are full matrices.

A two-port case study

Interesting results were found when comparing two measurement sets of a two-port high gain amplifier, both taken with the same instrument. The two-port four-samplers VNA was calibrated by a LRM procedure, and the state A and state B error coefficients were computed as described in the previous Section 2.3.2. The first set was acquired with AA measurements, as in a complete hardware architecture. The second one used AB/BA measurements, like a three samplers VNA.

Differences in the amplifier S_{22} parameter were found, as shown in Fig. 2.13. The complete hardware model S_{22} measurement is considerably noisier. Since the VNA settings (IF bandwidth, number of averages...) were the same and the calibration verification showed no discrepancies, the difference should depend on how the measurement noise affects the deembedding.

In both cases, the S_{22} parameter is computed from (2.1) as

$$S_{22} = \frac{b_2'' a_1' - b_2' a_1''}{a_2'' a_1' - a_2' a_1''}$$
(2.66)

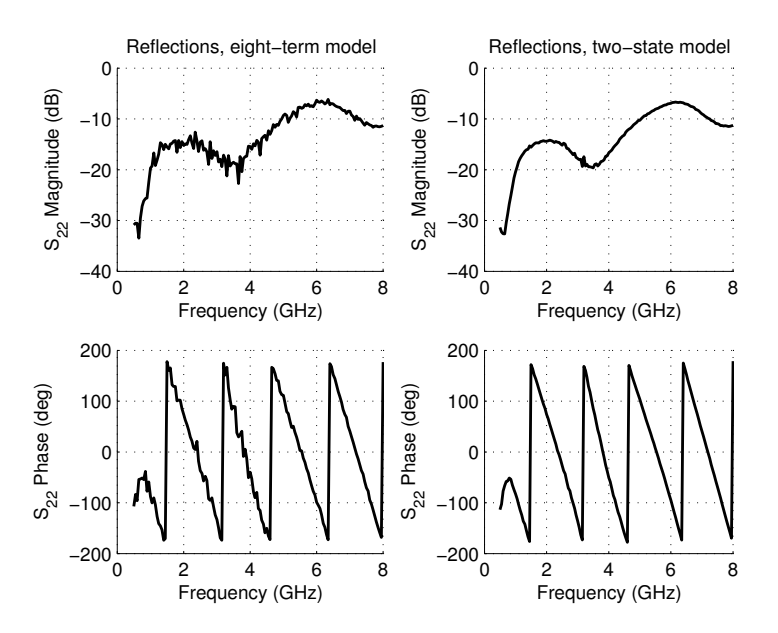


Figure 2.13. Miteq 2-4 GHz amplifier measurements. Shown is S_{22} parameter. Complete hardware model (left) and two-state model (right).

where the prime and double prime refer to the first and second port drive, respectively.

In the two-state hardware model, (2.66) is rewritten as

$$S_{22} = \frac{\frac{b_2''}{a_1''} - \frac{b_2'}{a_1'} \Gamma_1 \frac{b_1''}{a_2''}}{1 - \Gamma_1 \Gamma_2 \frac{b_2'}{a_1'} \frac{b_1''}{a_2''}}$$
(2.67)

where the ratioed quantities $\frac{b_2''}{a_1''}$, $\frac{b_2'}{a_1'}$ and $\frac{b_2''}{a_1''}$ are put into evidence and $\Gamma_i = a_i/b_i$ (in state B it becomes $\Gamma_i = g_i/f_i$). Instead, in the complete hardware model a_1 is computed from the measurements $a_{\rm m1}$ and $b_{\rm m1}$ and

$$S_{22} = \frac{\frac{b_2''}{a_1''} - \frac{b_2'}{a_1'} \frac{a_1''}{a_2''}}{1 - \frac{a_2'}{a_1'} \frac{a_1''}{a_2''}}$$
(2.68)

In both cases, the numerator consists of the raw $S_{22}^{raw} = \frac{b_2''}{a_1''}$ corrected by the product of the raw gain $S_{21}^{raw} = \frac{b_2'}{a_1'} \gg 1$ times a term that depends on the model. The way this term is computed determines the effect of the measurement noise in the final S_{22} parameter. The point is that the correction term should be close to

zero for both models, provided that the DUT has high isolation², but the two-state one is substantially less noisy than the complete hardware one.

Suppose that the DUT isolation is so high that both b_1'' in (2.67) and a_1'' in (2.68) are below the measurement noise. Now, if noise could be neglected, $a_1'' \approx \Gamma_1 b_1''$, that is, the a_1 magnitude is diminished by a factor $|\Gamma_1|$, which is low, being the VNA ports well matched ($|\Gamma_1| < -20$ dB). In the two-state model, that's exactly what happens, being the correction term $\Gamma_1 \frac{b_1''}{a_2''}$. In the complete hardware model, the correction term is a_1''/a_2'' , where a_1'' is computed from measurements, and thus its magnitude $|a_1''| \approx |b_1''|$ due to the measurement noise.

In conclusion, the two-state hardware mitigates the effects of the measurement noise in the reverse measurement. The noise advantage gets better as the DUT gain and isolation increase.

A four-port example

The two-port behavior extends to multiport devices as well. The S-matrix uncertainties in the output ports reflection coefficients (i.e. the matrix subset S_{oo}) are greater in the complete hardware model due to the amplified measurement noise.

Simulations were carried out using (2.63) and (2.65), and, consistently, the uncertainty difference was found to increase with the amplifier isolation. Differences up to a factor of 10 were observed, as Tab. 2.1 shows.

Scattering	Combined standard uncertainty					
parameter	Complete HW	Two-state HW				
$ S_{33} = 0.1$	4.5%	0.3%				
$ S_{34} = 0.03$	15%	1.1%				
$ S_{43} = 0.01$	45%	3.5%				
$ S_{44} = 0.1$	4.5%	0.3%				

Table 2.1. Measurement noise uncertainty comparison between the two multiport architectures. The simulated amplifier has $|S_{31}| = |S_{42}| = 40$ dB gain and $|S_{31}/S_{13}| = |S_{42}/S_{24}| = 60$ dB isolation; the receiver's channels are supposed to have 60 dB signal-to-noise ratio.

The actual measurement of a on-wafer CMOS balanced amplifier was then used in a simulation. The active devices had sub-0.1 μ m gate length and were designed for low noise applications, as a part of the Kelvin Project, a partnership between NIST, IBM and RFMD [50]. The on-wafer contacts were four ground-signal-ground pads with 150 μ m pitch; the pad metal was aluminum, being on a silicon substrate. Port 1 and 2 were the inputs; port 3 and 4 the outputs.

²The isolation of an amplifier is the ratio of the forward to the reverse gain: S_{21}/S_{12} .

The simulation is based on (2.63) and (2.65), and uses the actual VNA error coefficients associated with the DUT measurement. For the complete hardware architecture, only the state A error coefficients have been used in (2.65).

The computed type-A combined standard uncertainties due to the measurement noise in the S_{44} and S_{34} parameters are shown in Fig. 2.14 and 2.15, respectively.

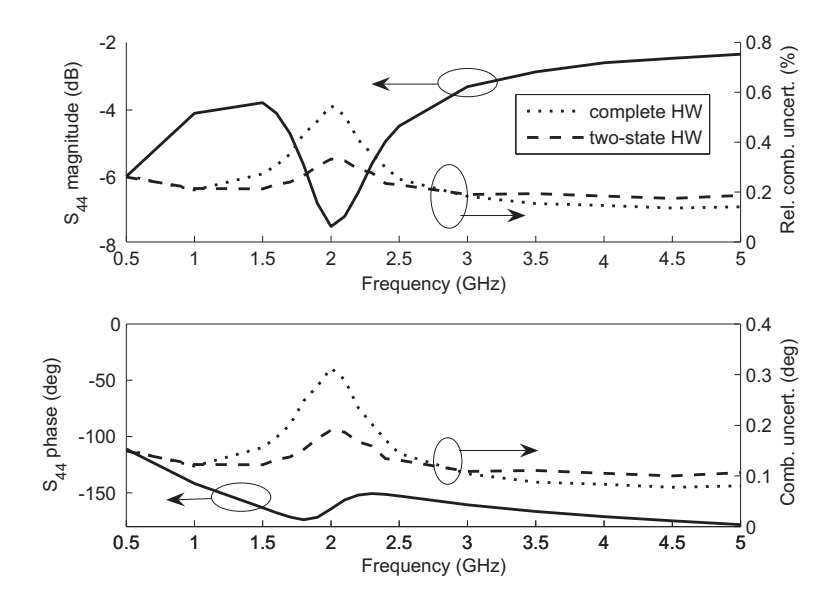


Figure 2.14. CMOS balanced amplifier measurement and standard uncertainty comparison. Combined standard uncertainties due to the measurement noise for the S_{44} reflection parameter.

The uncertainty of the two-state model is about one half the one of the traditional model.

The other parameters, *i.e.* the input reflection coefficients and the forward and reverse gains, have similar uncertainties in the two error models, with a small advantage for the two-states model, as Fig. 2.16 shows.

For passive reciprocal devices, the instrumentation noise generates an uncertainty contribution roughly equal in both error models. The same simulation as above was carried out for a passive on-wafer balun, consisting of a balanced-to-unbalanced transformer on silicon substrate. The two error models have practically the same uncertainty in Fig. 2.17, which shows the S_{34} parameter results. Similar agreement is found for the remaining S-parameters.

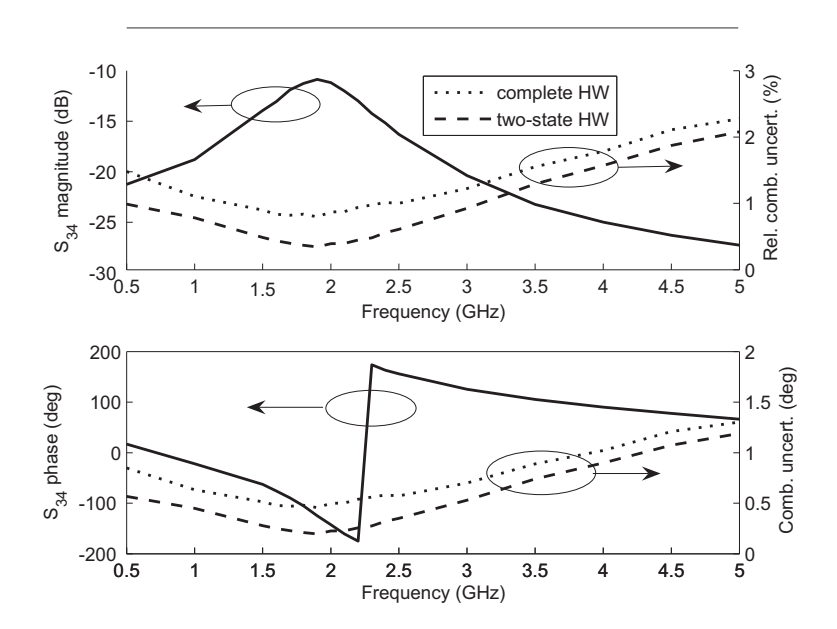


Figure 2.15. CMOS balanced amplifier measurement and standard uncertainty comparison. Combined standard uncertainties due to the measurement noise for the S_{34} crosstalk parameter.

Final comment

The presented results refer only to the type-A uncertainties due to the instrument's noise. The contact repeatability is completely neglected, as well as uncertainties in the error coefficient computation.

In the considered four port amplifier, the aluminum pads had a very poor repeatability due to aluminum oxidation. Special nickel-tip probes are needed in these cases, and it was found that the contact remained stable only for a quarter of hour. Even in the stable period, gain differences of 0.2 dB and reflection variations of up to 3 dB were observed between multiple measurements.

Hence, future work to derive a consistent and exhaustive multiport uncertainty analysis is needed.

2.5 Conclusions

This Chapter aimed to present a comprehensive view of multiport vector network analyzer error models. From the traditional VNA architecture with a full set of reflectometers, the measurement channels have been reduced and the consequences in the error models analyzed.

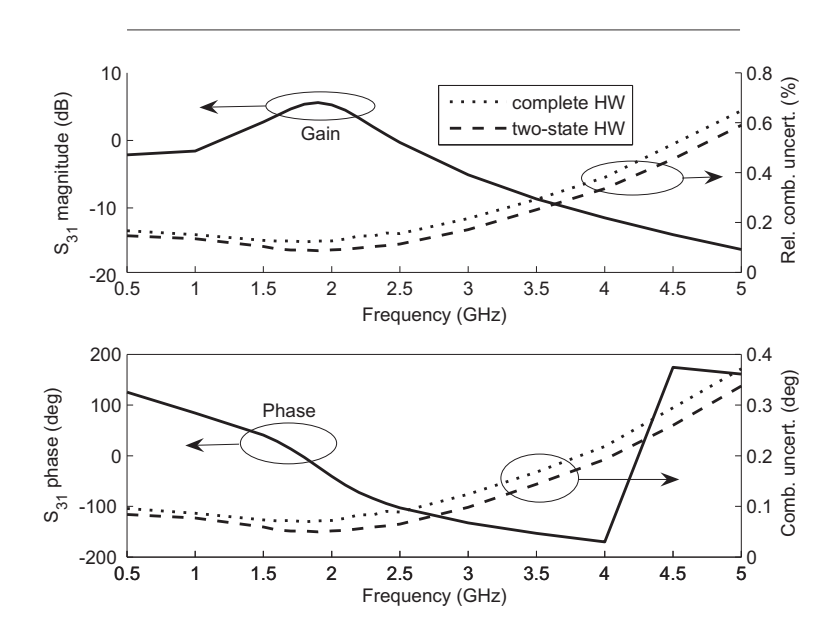


Figure 2.16. CMOS balanced amplifier measurement and standard uncertainty comparison. Combined standard uncertainties due to the measurement noise for the S_{31} gain parameter.

The two-state error model applied to a (N+2)-channel VNA was found as a optimum compromise. From the hardware point of view, the costs are substantially reduced (almost half of the measurement channels) and the measurement speed practically doubled (N(N+1)) measurements against $2N^2$, as in Fig. 2.1(a)). For what matters the calibration flexibility, it remains the same as the complete hardware model and also the number of standard connections is the same, while the number of error coefficients little increases from 4N-1 to 6N-1, as in Fig. 2.1(b).

The elegance of the two-state de-embedding procedure resides in the particular switch error correction. An analysis has been carried out, which shows that the two-state model has advantages in terms of measurement noise in some cases. However, a thorough uncertainty analysis is still lacking (even for the complete hardware multiport case), so no statements can be said on which error model performs better.

As a matter of fact, the two-state (N+2)-channel architecture performs certainly better than the multistate (N+1)-channel one. Fewer error coefficients and standard connections are needed, and, above all, the need of perfectly known calibration standards is avoided.

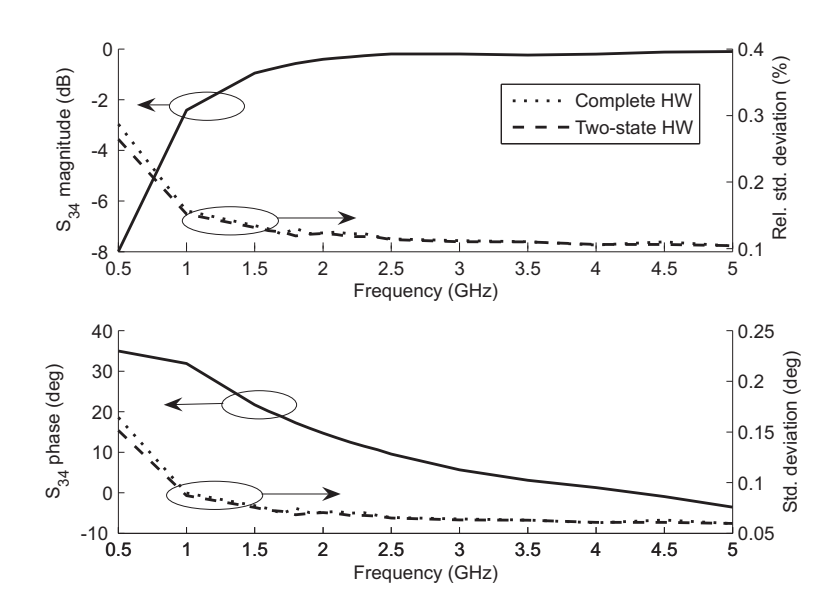


Figure 2.17. On-wafer balun measurement and standard uncertainty comparison. Combined standard uncertainties due to the measurement noise for the S_{34} transmission parameter.

Chapter 3

Large-Signal Multiport Measurement Techniques

This Thesis presents original contributions to the assessment of high-frequency large-signal multiport measurement techniques. The research work was carried on at the Politecnico di Torino, leading to the development of a comprehensive measurement test-set.

This Chapter introduces the large-signal multiport characterization problem and details the multiport measuring system, with focus on the calibration steps.

3.1 Basics

Large-signal measurements are intended for non-linear active devices characterization. When the input signal drive of an amplifier has enough amplitude, the amplifier turns into compression, and the output waveform gets distorted.

Power amplifiers are often operated close to saturation, since at that driving point the efficiency η and the power-added efficiency PAE have maximum values, as in Fig. 3.1. Under large signal conditions, peak power and efficiency improvements are also obtainable by tuning the load connected to the amplifier output. Generally speaking, the large signal optimum load point gives far better performances in terms of output power and efficiency than an output complex-conjugate matching calculated from the DUT small-signal parameters, as Fig. 3.2 shows.

Load-pull and source-pull techniques are devoted to large-signal characterization. They are based on an experimental search of the optimum operating conditions: the load (or source) reflection coefficient is varied while monitoring all the interesting performances, until the optimal point is found. In practice, the load (or source) reflection coefficient is set at multiple positions across the Smith Chart, and at each point the relevant measurements are performed. The collected data are used to

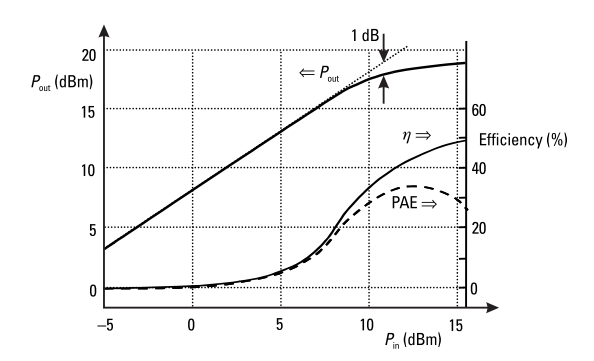


Figure 3.1. Large signal P_{in}/P_{out} plot. As the amplifier turns into compression, the gain lowers but the efficiency generally increases.

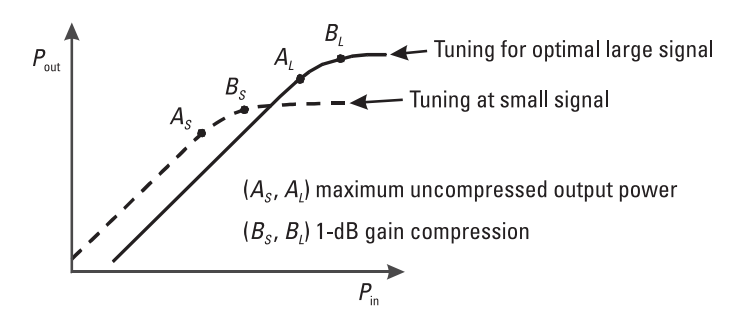


Figure 3.2. Large-signal and small-signal design comparison.

generate a map, which shows the constant-performance curves versus the reflection coefficient value, as in Fig. 3.3, from which the optimum point is easily identified.

Being what-you-see-is-what-you-get techniques, these methods do not rely on any assumptions on the non-linear behavior or on electrical DUT models, thus the measurement data can be readily used in actual power amplifier designs. The design time and development costs are substantially cut, since, basically, the designer tasks consist on synthesizing the matching networks that provide the optimal loading conditions with minimum loss.

The easiest way to tune the DUT terminations at microwave frequencies is using passive tuners, which principle is sketched in Fig 3.4.

A simple load- and source-pull test-set is sketched in Fig. 3.5, where two passive tuners are used to vary both the source and the load reflection coefficients. The DUT is biased by a power supply and two bias tees. The RF measurements are taken by two power meters; the first one directly measures the DUT output power, while the second is connected to the input directional coupler and samples the DUT

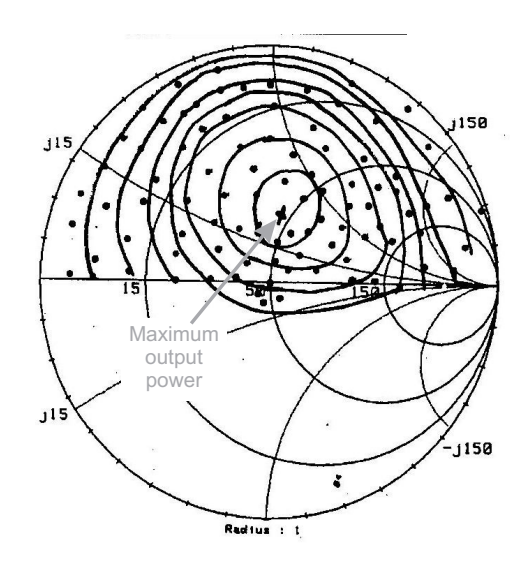


Figure 3.3. An example of load-pull map. The plotted curves are the constant output power loci interpolated from the measurement points.

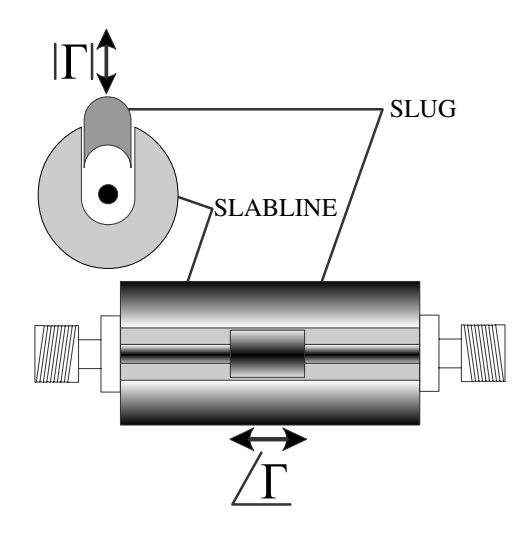


Figure 3.4. Microwave passive tuner example. The mismatch created by the slug insertion varies the tuner's reflection coefficient magnitude, while its phase depends on the slug position along the slabline.

input incident power. The DUT large-signal stimulus comes from a driver amplifier, which increases the RF generator signal power.

In such test-set, the measurement accuracy is limited by the components' nonidealities. In particular, the input coupler coupling should be well characterized, and

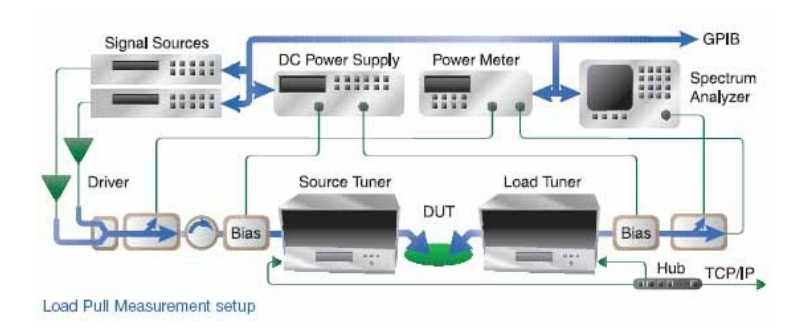


Figure 3.5. Basic load- and source-pull test-set made of commercially-available instruments. Courtesy of Focus Microwaves.

its directivity needs to be as high as possible, otherwise the incident power reading will be affected by the DUT input reflected power.

Moreover, losses associated with the tuners and the bias tees should be accounted for in order to extract the actual DUT output power. As the tuner is varied, its loss changes, and thus one should pre-characterize it in order to establish a map between the slug positions and the tuner's S-parameters magnitude and phase, from which the tuner reflection coefficient and loss can be computed. The pre-characterization phase is a time-consuming procedure and, above all, requires tight mechanical repeatability. Unfortunately, the measurement uncertainty due to the tuners' repeatability is not negligible at all in many cases. A thorough investigation of the repeatability effects was carried out by Teppati in [51], demonstrating the lacks of this technique.

Advanced load-pull benches are well-established in the microwave laboratory at the Politecnico di Torino for more than one decade. Compared to commercial products, the main advantages are

- 1. the tuner pre-characterization is avoided, and the system calibration lasts few minutes;
- 2. the systematic effects due to the components' non-idealities are removed by vectorial calibration techniques;
- 3. the quantities of interest are measured in real-time.

The basic set-up is shown in Fig. 3.6. The key feature is the use of two reflectometers connected to a vectorial measurement system, which is typically based on a HP8510C VNA. The architecture is similar to a two-port VNA with a complete set of reflectometers; the difference consists on the use of high-power directional couplers instead of directional bridges. The great advantage is that the test-set allows for a rigorous vectorial calibration at the DUT planes.

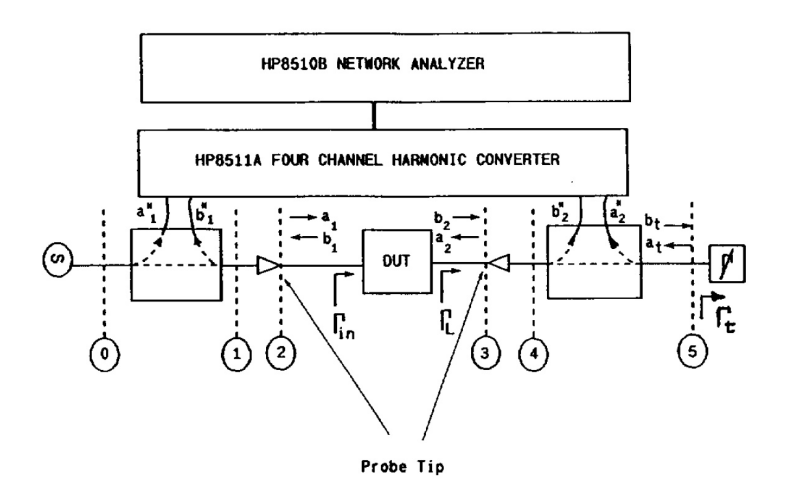


Figure 3.6. Basic configuration for the two-port load-pull test-set at Politecnico di Torino [6].

Being devoted to absolute measurements, the test-set requires a power calibration. This is performed either at the DUT planes or at one external port by a calibrated RF power meter [6], as it will be shown.

During the measurement, the DUT is driven in the forward direction only, while the variable tuner terminates the output port reflectometer (plane 5), and thus it can vary the load reflection coefficient at plane 3. The quantities of interest are the input and output powers

$$P_{in} \equiv |a_1|^2 - |b_1|^2$$
 (3.1)
 $P_{out} \equiv |b_2|^2 - |a_2|^2$ (3.2)

$$P_{out} \equiv |b_2|^2 - |a_2|^2 \tag{3.2}$$

from which the DUT operating gain can be computed

$$G_{op} \equiv \frac{P_{in}}{P_{out}}. (3.3)$$

Moreover, very important figures of merit are the already introduced efficiency η and the power-added efficiency (PAE), defined as

$$\eta \equiv \frac{P_{out}}{P_{bias}} \tag{3.4}$$

$$\eta \equiv \frac{P_{out}}{P_{bias}}$$

$$PAE \equiv \frac{P_{out} - P_{in}}{P_{bias}}.$$
(3.4)

where P_{bias} is the total DC bias power.

Efficiency of power amplifiers can be improved by providing proper terminations at the fundamental and harmonic frequencies for both load and source. The second harmonic load tuning can improve efficiency by a few percentage points. The third harmonic has a lower effect, and tuning at higher harmonics is typically not effective.

While the fundamental tuning can be accomplished by passive tuners, at harmonics passive tuners have limitations. In particular, the independent tuning of all the frequency components is extremely difficult, as moving the reflection coefficient at the fundamental has an impact on the harmonic reflection coefficients, due to the tuners' broad-band nature. Therefore, diplexers, triplexers or other frequency-selective devices should be used to limit the tuners' frequency dependence, as in Fig. 3.7.

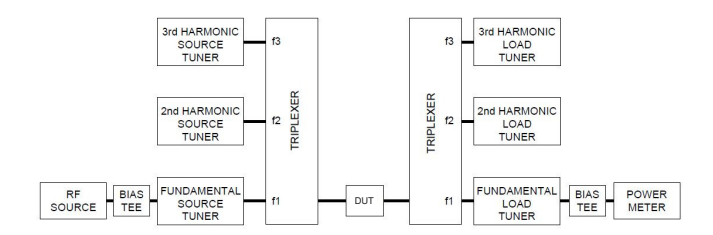


Figure 3.7. Passive Tuner System with 2nd and 3rd Harmonic Source and Load Tuning. Courtesy of Maury Microwave Co. [7].

An alternative solution, born at the Politecnico di Torino in 1982 [52], is the use of active loads, which principle is sketched in Fig. 3.8. The wave incident into the

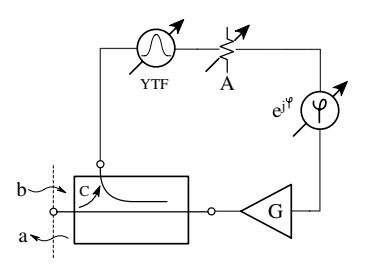


Figure 3.8. Active load block schematic.

load (b) is sampled by the loop coupler, and fed to a cascade made of a tunable bandpass filter (YTF), an electronic attenuator, a phase shifter and a power amplifier. Therefore, the wave reflected by the load (a), which is the power amplifier output signal, can be varied in both amplitude and phase, and the synthesized reflection coefficient becomes

$$\Gamma_L = \frac{a}{b} \approx c \cdot A \cdot e^{j\phi} \cdot G.$$
 (3.6)

Active loads can synthesize reflection coefficient up to and even more than unity magnitude, since losses are effectively compensated by the amplifier's gain, which simply cannot be done with passive tuners. There is a limit, however. If the overall loop gain $(c \cdot A \cdot G)$ is increased up to approach the coupler's directivity value, auto-oscillation may occur. Therefore, the overall loop gain should not be increased above 0 dB

A further advantage of active loads consists on being very frequency-selective due to the presence of the band-pass tunable filter. The YTF (YIG, Yttrium iron garnet, tunable filter) can be tuned over a wide frequency range, and provides a sharp resonance with 3 dB bandwidth of about 20 MHz. Outside this bandwidth, the attenuation is so high that the loop gain is negligible, and the load behaves like a 50 Ω termination ($\Gamma \approx 0$). This is required in order to avoid possible loop oscillations due to the loop coupler's out-of-band poor directivity, but one can take advantage of the selectivity and combine two loops for multi-frequency (harmonic) tuning, as in Fig. 3.9. Moreover, harmonic active loops are particularly effective in

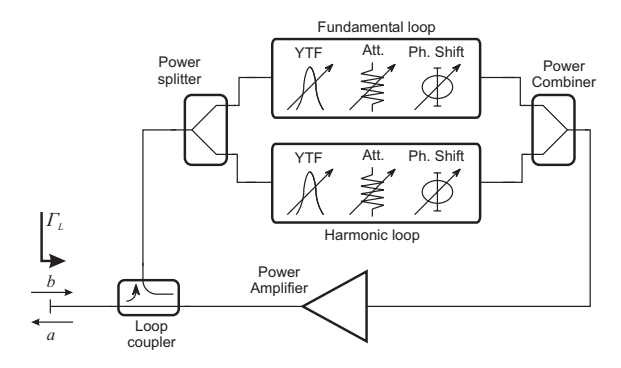


Figure 3.9. Harmonic active load block schematic.

synthesizing highly reflective loads, which provide the best efficiency improvements.

The active load technique can be effectively used as variable source termination as well, and the set-up becomes the one in Fig. 3.10. The power amplifier is used both to provide the necessary active loop gain, and to increase the RF source signal. The active loop band-pass filter is typically tuned at harmonic frequencies, as there are no efficiency improvements at the fundamental frequency.

A two-port test-set based on active loops is shown in Fig. 3.11. The measurement reflectometers are integrated in the active terminations, being the loop couplers in between the reflectometers and the DUT ports. In this way, the reflectometers' losses are included in the loops, thus improving the loops stability [53]. If the loop

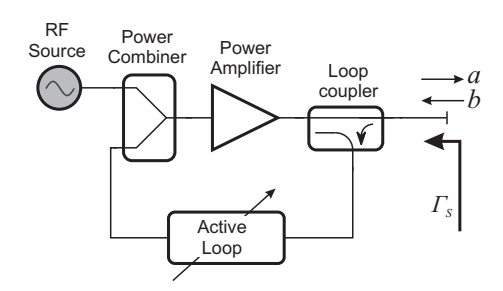


Figure 3.10. Active source block schematic.

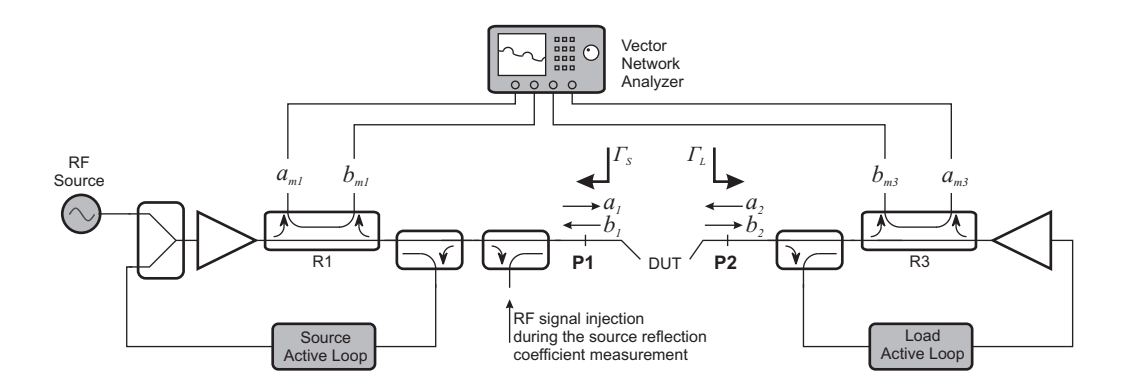


Figure 3.11. Load-pull and source-pull test-set based on active loops.

couplers were behind the reflectometers, the active load reflection coefficient should have been increased in order to compensate the losses, and thus the closed loop stability would have been degraded.

A recent trend is the growth of multiport balanced devices (e.g. with two inputs and two outputs), either amplifiers or transmitters/oscillators. This imposes new measurement challenges, since current load-pull benches are restricted to two ports. Usually, balanced DUT performances are expressed in terms of mixed-mode parameters, which combine both differential-mode and common-mode responses [54,55].

Episodic efforts had addressed the balanced load-pull characterization [56, 57]. The fundamental problem of implementing a balanced load and defining the actual quantities of interest was addressed in this Thesis. A complete four-ports balanced source- and load-pull system was first presented by Teppati, Ferrero, Garelli and Bonino in [58].

3.2 Mixed-mode load-pull bench

The four-port load-pull measurement system can be considered as an extension of the two-port one. The main differences consist on the source and load terminations, which become two-port devices, as in Fig. 3.12.

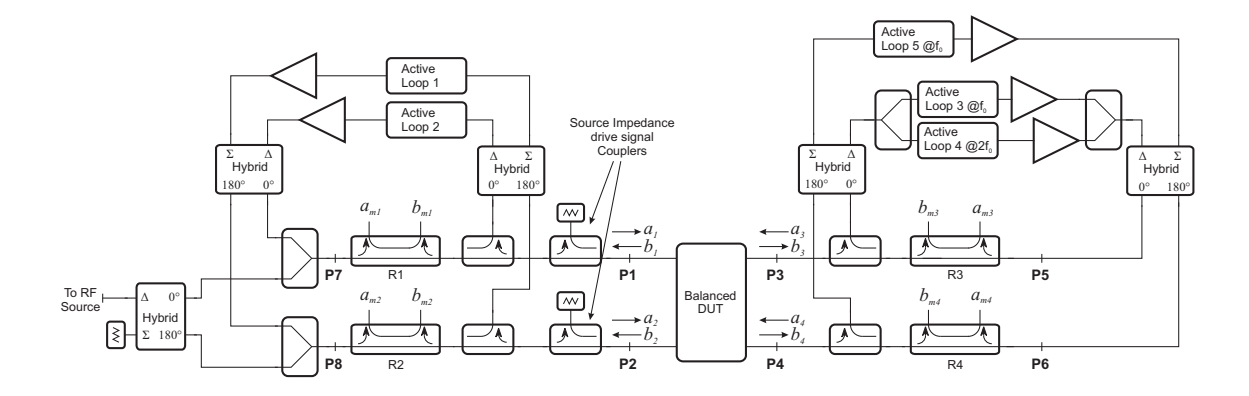


Figure 3.12. The differential load-pull system at the Politecnico di Torino. The VNA is a HP8510C with a HP8511A test-set.

The test-set consists of four double directional couplers (reflectometers) that sample the incident and reflected waves at each port. A HP8510C VNA then reads the eight waves at turn, selecting them by a SP8T coaxial switch (not shown).

The test-set uses two mixed-mode active loads, one connected to the DUT outputs (ports 3 and 4) and the other to the DUT inputs (ports 1 and 2). Both are

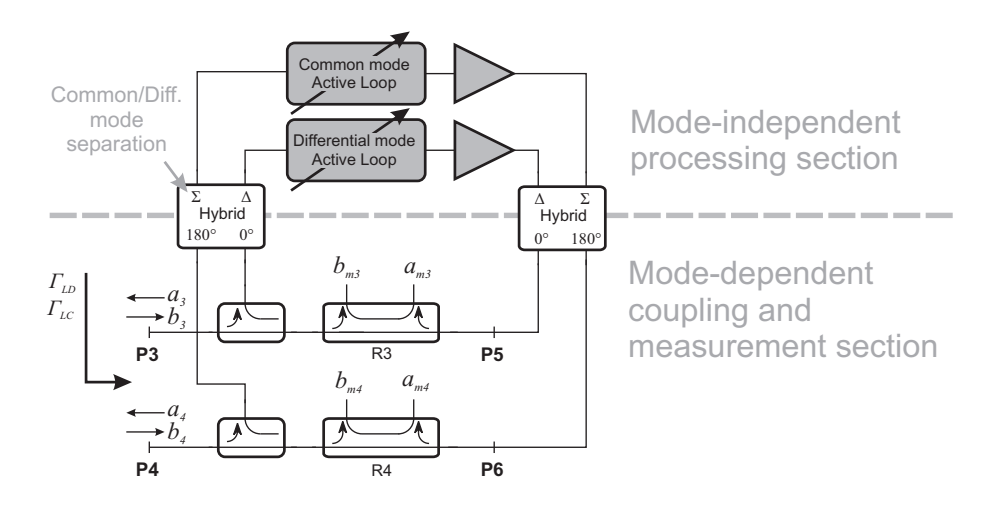


Figure 3.13. The mixed-mode active loop principle.

devoted to tune the DUT loading conditions, in terms of common- and differential-mode reflection coefficients. The basic principle of each load is sketched in Fig. 3.13 [59,60]. The two loop couplers sample the incident waves into the load, and the common- and a differential-mode components are split by the first 3 dB, 180° hybrid. The modal components are independently processed by two active loops and amplifiers, and then the signals are recombined by the second hybrid. Finally, the recombined signals are fed back to the DUT, and constitute the load reflected waves [60].

The source load also comprises the stimulus section. The DUT differential drive is made by a 3 dB 180° hybrid connected to the signal source. The drive power is then varied by acting on the source.

3.2.1 Error model and calibration

The test-set is properly described by a complete hardware architecture model, as presented in the previous Chapter, Sec. 2.2.1. This model, through the use of a complete set of reflectometers, is characterized by error coefficients insensitive to the load and source tuning, as demonstrated in [38,61]. This is a great advantage, since the system's calibration does not require a pre-characterization of the load and the source reflection coefficients. Thus, the actual waves are expressed in terms of the measurements by (2.5) and (2.6).

A suitable scattering calibration (one example is shown in Fig. 3.14) will determine 4N-1=15 error coefficients

$$\frac{h_i}{k_1}, \frac{l_i}{k_1}, \frac{m_i}{k_1}, \frac{k_i}{k_1}$$
 $(i = 1, \dots, N).$

The mixed-mode source and load are disconnected during the calibration, and the RF drive is applied using a SP4T switch. This does not affect the calibration accuracy, since the disconnected connectors are placed either behind the reflectometers (no effect at all), or on the coupled arms of the loop couplers (the effect is widely mitigated by the low coupling).

The calibration normalization free parameter (k_1) is used for the absolute power and time-reference calibration. Its magnitude sets the power-scaling coefficient, so that the actual power incident into port i is easily computed as

$$P_i^+ = |a_i|^2 = |k_1|^2 \left| -\frac{h_i}{k_1} a_{mi} + \frac{l_i}{k_1} b_{mi} \right|^2.$$
 (3.7)

If a direct connection of the power meter to port i were possible, the unknown $|k_1|$ would be easily computed from the measured P_i^+ . Instead, particularly for on-wafer applications, the system takes advantage of an external coaxial port (the

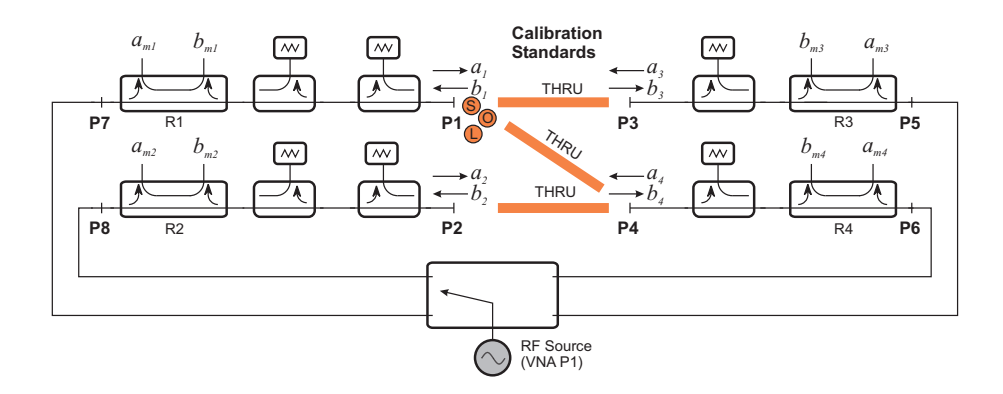


Figure 3.14. An example of multiport scattering parameter calibration. Three one-port standards (Short, Open, Load) are used at port 1, and three known *thru* standards are connected between 1-3, 1-4, 2-4.

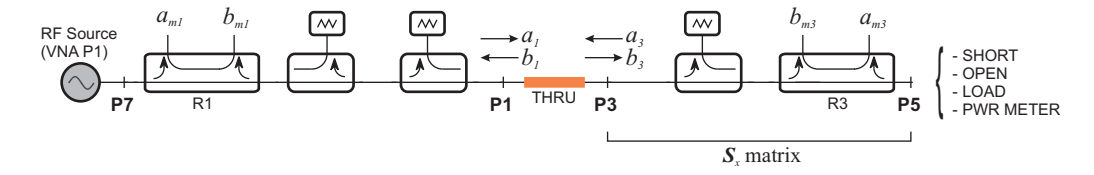


Figure 3.15. Power calibration. A thru standard is connected between ports 1 and 3, and Short, Open, Load standards are measured at the auxiliary port 5.

example in Fig. 3.15 uses port 5), to which the power meter is connected. A one-port short-open-load calibration is performed at the external port (port 5), and the newly computed error coefficients h_5/k_5 , l_5/k_5 and m_5/k_5 are then referenced to port 1, as described in [6], obtaining

$$\frac{h_5}{k_1}$$
, $\frac{l_5}{k_1}$, $\frac{m_5}{k_1}$.

Finally, $|k_1|$ is computed using (3.7) as

$$|k_1|^2 = \frac{P_5^+}{\left| -\frac{h_5}{k_1} a_{m5} + \frac{l_5}{k_1} b_{m5} \right|^2}.$$
 (3.8)

where P_5^+ is the power meter reading at port 5, and the measured waves are $a_{\rm m5} = b_{\rm m3}, b_{\rm m5} = a_{\rm m3}$.

Time-domain waveform calibration

The waveform calibration determines the correct phase of k_1 at the harmonic frequencies by an additional measurement from a calibrated sampling oscilloscope or

microwave transition analyzer (MTA). The MTA can be regarded as a sampling oscilloscope, which can automatically compute the waveform's spectral components, in magnitude and phase [62]. This kind of instrument is currently out of production, thus modern sampling oscilloscopes are being used. Since the vector error correction procedure are implemented in the frequency domain, the time-domain calibrated measurement should be expanded in spectral components, which can be computed by the Discrete Fourier Transform, or by the scalar projection of the time-domain signal on the phasors' basis functions [63].

The measured time-domain signal v(t) can be approximated as a truncated Fourier series

$$v(t) = \sum_{n=1}^{N_{ph}} \Re(V_n \cdot e^{j2\pi \cdot nf_0 \cdot t})$$
(3.9)

where N_{ph} is the number of phasors to be used, and $V_n = V_{Rn} + jV_{In}$ is the complexvalued phasor at frequency nf_0 . If the measured waveform consists on N_s uniformly spaced samples at time intervals ΔT , the phasors' real and imaginary parts become

$$\sum_{n=1}^{N_{ph}} \left[V_{Rn} \cos(2\pi \cdot nf_0 \cdot m\Delta T) - V_{In} \sin(2\pi \cdot nf_0 \cdot m\Delta T) \right] = v(m\Delta T), \qquad (3.10)$$

$$(m = 1, \dots, N_s)$$

which can be regarded as a linear system in the V_{Rn} and V_{In} unknowns. The phasors' real and imaginary parts are then computed in the least-squares sense, being the number of time points (N_s) greater than the number of unknowns $(2N_{ph})$ [63].

In previous two-port time-domain load-pull systems at the Politecnico di Torino, the MTA has been used as a phase-calibrated measurement channel [64]. The current multiport test-set is based on a different approach. The harmonic phasors are measured by the VNA, that receives as reference signal a phase-coherent harmonic set produced by a stable comb generator, as shown in Fig. 3.16.

During the scattering parameter calibration, or during the DUT S-matrix measurement, the VNA phase lock is set to the RF source signal (A1 channel). The VNA phase lock is then switched to the comb generator output (A2 channel) during the harmonic phase calibration and the DUT harmonic measurement, while the RF source signal is fixed to the fundamental frequency f_0 . In this way, the VNA reference signal has a stable phase relationship with the DUT harmonics, since both share the same source.

The VNA measurements are considerably faster than the MTA or sampling oscilloscope ones, but the system still requires a harmonic phase calibration. The time-reference calibration is performed after the power calibration, using the same thru connection as in Fig. 3.15, while the RF sinusoidal source is substituted by the

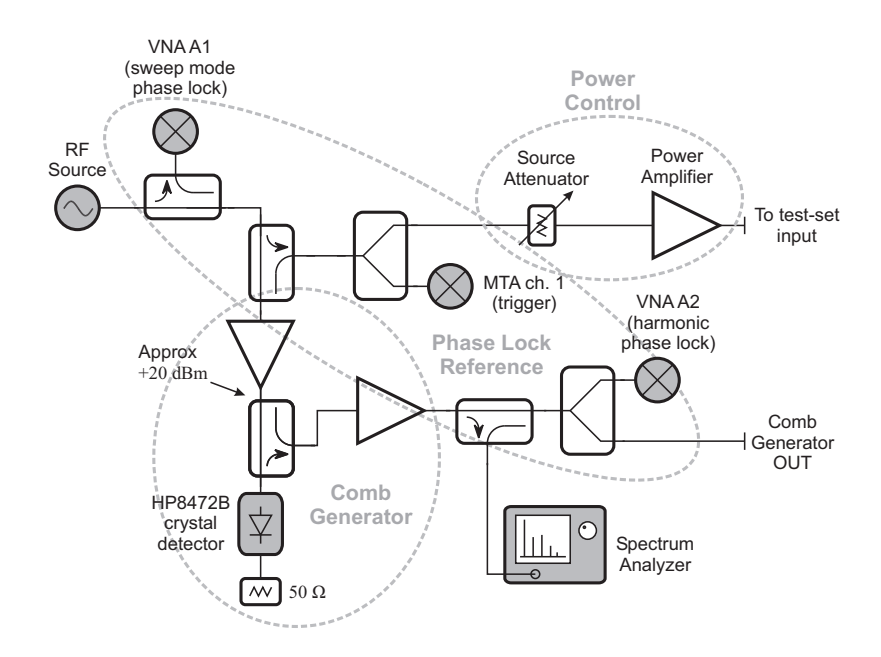


Figure 3.16. Custom-made comb generator block schematic. With a RF source frequency of 2 GHz, the useful harmonic content extends up to 12 GHz. The auxiliary source is locked to the VNA 10 MHz reference signal.

comb generator and the sampling scope is connected to the external port, as shown in Fig. 3.17.

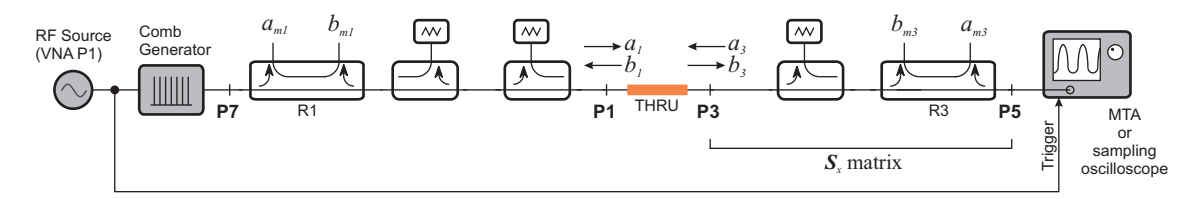


Figure 3.17. Time-domain waveform calibration. A thru standard is connected between ports 1 and 3, and the voltage waveform at the auxiliary port 5 is measured by the sampling scope.

The measured time-domain voltage waveform at plane 5 is used to compute the respective harmonic phasors $V_n = V_{Rn} + jV_{In}$ using (3.9). The voltage phasors relate to the port 5 waves by (1.1), (1.5) and (1.6), and it becomes

$$V_n = \sqrt{2}\sqrt{Z_\infty} \left[a_5(nf_0) + b_5(nf_0)\right], \quad (n = 1, \dots, N_{ph})$$
 (3.11)

where the $\sqrt{2}$ factor is due to conversion from RMS to peak voltages. The phase¹

The k_1 magnitude could be computed as well, but, in this case, the power meter has higher

of k_1 is computed from the VNA measurements and calibration coefficients as

$$\angle k_{1}(nf_{0}) = \angle \left[\frac{\frac{1}{\sqrt{2}}\sqrt{Y_{\infty}} \cdot V_{n}}{\left(\frac{l_{5}(nf_{0})}{k_{1}(nf_{0})} + \frac{k_{5}(nf_{0})}{k_{1}(nf_{0})}\right) b_{m5}(nf_{0}) - \left(\frac{h_{5}(nf_{0})}{k_{1}(nf_{0})} + \frac{m_{5}(nf_{0})}{k_{1}(nf_{0})}\right) a_{m5}(nf_{0})} \right].$$

$$(3.12)$$

3.2.2 Real-time measurements

The system measures 2N = 8 waves at the reflectometer's outputs at each frequency of interest. A complete DUT measurement typically includes five harmonic components, leading to 40 measurements, and is performed in less than a couple of seconds.

The substantial difference between multiport load-pull and two-port load-pull is the increased number of parameters of interest. For example, while in the two-port case the DUT input reflection coefficient is defined as $\Gamma_{in} = b_1/a_1$, in the four-port case it becomes a 2×2 matrix Γ_{in} that expresses the scattering of a_1 , a_2 to b_1 , b_2 and thus has four parameters. Moreover, the matrix Γ_{in} is non-linear with the source drive signals, thus a rigorous computation by alternating different drive conditions (like the scattering matrix case) is not feasible.

To overcome this problem, the DUT performances can be expressed in terms of measurable quantities, which are strictly derived from the actual incident and reflected waves. In the multiport case, most of these quantities become dependent on the drive signal.

In their simplest form, when the port reference impedance is set to 50 Ω , the mixed-mode waves are computed from the single-ended ones as [54]

$$a_{D1} = \frac{1}{\sqrt{2}}(a_1 - a_2), \quad a_{C1} = \frac{1}{\sqrt{2}}(a_1 + a_2)$$
 (3.13)

$$b_{D1} = \frac{1}{\sqrt{2}}(b_1 - b_2), \quad b_{C1} = \frac{1}{\sqrt{2}}(b_1 + b_2)$$
 (3.14)

$$a_{D2} = \frac{1}{\sqrt{2}}(a_3 - a_4), \quad a_{C2} = \frac{1}{\sqrt{2}}(a_3 + a_4)$$
 (3.15)

$$b_{D2} = \frac{1}{\sqrt{2}}(b_3 - b_4), \quad b_{C2} = \frac{1}{\sqrt{2}}(b_3 + b_4).$$
 (3.16)

This sets the differential mode reference impedance $Z_D = 100 \Omega$ and the common-mode one $Z_C = 25 \Omega$. The general case, where the reference impedances are unequal, is presented in [55].

accuracy than the sampling oscilloscope or MTA.

Typical parameters of interest are the differential- and common- mode DUT output and input powers (at the fundamental or harmonic frequencies)

$$P_{outD} = |b_{D2}|^2 - |a_{D2}|^2, P_{outC} = |b_{C2}|^2 - |a_{C2}|^2, (3.17)$$

$$P_{inD} = |a_{D1}|^2 - |b_{D1}|^2, P_{inC} = |a_{C1}|^2 - |b_{C1}|^2, (3.18)$$

$$P_{inD} = |a_{D1}|^2 - |b_{D1}|^2, P_{inC} = |a_{C1}|^2 - |b_{C1}|^2, (3.18)$$

where b_{D2} and b_{C2} are the differential- and common-mode reflected waved at the DUT outputs, a_{D2} , a_{C2} the incident ones, and b_{D1} , a_{D1} and b_{C1} , a_{C1} the differentialand common-mode waves at the DUT input, respectively.

The main DUT performances are the power gains

$$G_D = \frac{P_{outD}}{P_{inD}}, \qquad G_C = \frac{P_{outC}}{P_{inC}}.$$
 (3.19)

Load tuner measurement

The source and load mixed-mode active tuners are designed for operation in linearity, thus they are fully described by 2×2 scattering matrices. In Fig. 3.18 the schematic models of the source and load tuners are sketched.

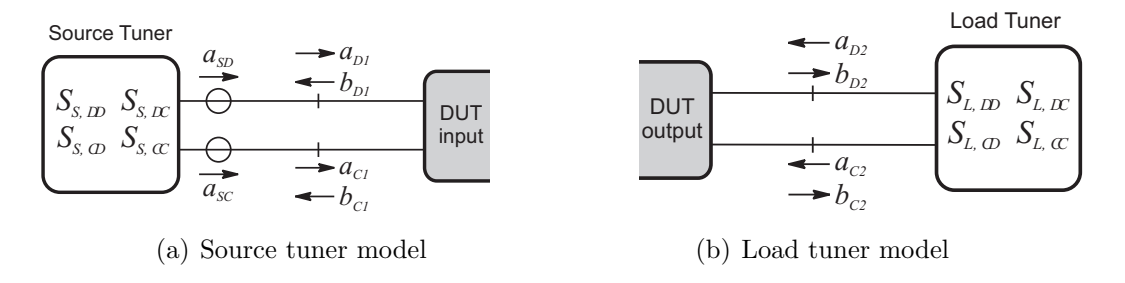


Figure 3.18. Schematic representation of the source and load tuners and their mixed-mode parameters.

As in Fig. 3.18(b), the load tuner is described by four scattering parameters

$$\begin{bmatrix} a_{D2} \\ a_{C2} \end{bmatrix} \equiv \underbrace{\begin{bmatrix} S_{L,DD} & S_{L,DC} \\ S_{L,CD} & S_{L,CC} \end{bmatrix}}_{\mathbf{S}_{L}} \begin{bmatrix} b_{D2} \\ b_{C2} \end{bmatrix}$$
(3.20)

which are varied acting on the tuner active loops.

Since the DUT imposes the driving condition to the two-port load, its scattering matrix cannot be measured in real time.

Actually, the DUT output powers P_{outD} , P_{outC} depend on only two –not four– parameters:

$$P_{outD} = |b_{D2}|^2 - |a_{D2}|^2 = |b_{D2}|^2 (1 - |\Gamma_{LD}|^2)$$
(3.21)

$$P_{outC} = |b_{C2}|^2 - |a_{C2}|^2 = |b_{C2}|^2 (1 - |\Gamma_{LC}|^2),$$
 (3.22)

where the differential- and common-mode load reflection coefficients are defined as

$$\Gamma_{LD} \equiv \frac{a_{D2}}{b_{D2}}, \qquad \Gamma_{LC} \equiv \frac{a_{C2}}{b_{C2}}.$$
(3.23)

Unlike the four load scattering parameters, Γ_{LD} and Γ_{LC} can be measured in realtime, with the DUT plugged on, from the calibrated incident and reflected waves at ports 3,4. Moreover, their knowledge is exhaustive in defining the DUT output power dependence.

The mixed-mode load separates the differential- and common-mode components by two 180° hybrids. It is interesting to analyze the effects of the hybrids' nonidealities, which result in an imperfect modal separation. A detailed analysis of such contributions was presented in [59]. From (3.20), the differential- and common-mode load reflection coefficients depend on the load S-parameters as

$$\Gamma_{LD} = S_{L,DD} + S_{L,DC} \frac{b_{C2}}{b_{D2}}$$

$$\Gamma_{LC} = S_{L,CC} + S_{L,CD} \frac{b_{D2}}{b_{C2}}.$$
(3.24)

$$\Gamma_{LC} = S_{L,CC} + S_{L,CD} \frac{b_{D2}}{b_{C2}}.$$
 (3.25)

and it is clear that any mode-conversion effects $(S_{L,DC}, S_{L,CD})$ have influence on Γ_{LD} and Γ_{LC} .

However, a perfect independence of the two reflection coefficients (i.e. $S_{L,DC}$ = $S_{L,CD} = 0$) is not strictly required, since the quantities of interest (P_{outD}, P_{outC}) depend on the actual Γ_{LD} and Γ_{LC} values, which are measurable. The statement was proved by a simple experiment. An AD8351 balanced amplifier mounted on its evaluation board was measured at 2 GHz with two different load configurations:

- 1. The true mixed-mode load (MM), as in Fig. 3.12, is used.
- 2. A two-port load made of two independent single-ended active loads (SE) is used.

In both cases, Γ_{LD} and Γ_{LC} were measured and set to the same values, and the results are shown in Tab. 3.1. The performances are pretty unchanged in the

Load	Γ_{LD}		Γ_{LC}		P_{outD}	P_{outC}	G_D
setting	' '						
1) MM	0.67	162°	0.43	118°	-8.0	-18.4	-0.7
2) SE	0.68	162°	0.40	123°	-8.1	-18.1	-0.7

Table 3.1. Performance comparison between two different load configurations.

two cases, and the small differences are due to the imperfect alignment of the two conditions.

In any case, a mixed-mode load with good mode independence greatly simplifies the tuning and thus reduces the measurement time.

Source tuner measurement

The DUT source termination in Fig. 3.18(a) is described by

$$\begin{bmatrix} a_{D1} \\ a_{C1} \end{bmatrix} \equiv \underbrace{\begin{bmatrix} S_{S,DD} & S_{S,DC} \\ S_{S,CD} & S_{S,CC} \end{bmatrix}}_{\mathbf{S}_{S}} \begin{bmatrix} b_{D1} \\ b_{C1} \end{bmatrix} + \underbrace{\begin{bmatrix} a_{SD} \\ a_{SC} \end{bmatrix}}_{\mathbf{a}_{S}}$$
(3.26)

and depends on four scattering parameters and two source terms.

Source tuning at the fundamental frequency can be used to achieve higher power transfer to a mismatched DUT, but is generally of minor interest. Harmonic source tuning has instead wider impacts on the DUT performances like the power-added efficiency (PAE) [65].

The harmonic source tuner measurement may take advantage of the harmonic signals generated by the DUT non-linear input ports, which act as drive signals incident into the source tuner, provided that the RF source has very low harmonic content. In this way, two source parameters can be measured at each harmonic frequency excluding the fundamental one, namely the source differential- and common-mode reflection coefficients

$$\Gamma_{SD} \equiv \frac{a_{D1}}{b_{D1}}, \qquad \Gamma_{SC} \equiv \frac{a_{C1}}{b_{C1}}.$$
(3.27)

Time-domain waveforms measurement

Power amplifier designers are familiar with voltage or current waveforms, which give direct informations on the signal distortion, and are of great importance in the design work. By a proper waveform engineering, it is possible to increase the amplifier efficiency be some percentage points [66–68]. The "engineering" part consists, basically, on tuning the harmonic load and source reflection coefficients, which have a direct effect on the waveform's shape [69].

The (peak) voltage and input current phasors at each DUT port i can be computed from the port's waves a_i and b_i by

$$V_i(nf_0) = \sqrt{2}\sqrt{Z_{\infty}}[a_i(nf_0) + b_i(nf_0)]$$
 (3.28)

$$I_i(nf_0) = \sqrt{2}\sqrt{Y_\infty}[a_i(nf_0) - b_i(nf_0)]$$
 (3.29)

which are easily derived from (1.1), (1.5) and (1.6). Similarly to (3.9), the respective time-domain waveforms are computed as

$$v_i(t) = \sum_{n=1}^{N_{ph}} \Re(V_i(nf_0) \cdot e^{j2\pi \cdot nf_0 \cdot t})$$
(3.30)

$$i_i(t) = \sum_{n=1}^{N_{ph}} \Re(I_i(nf_0) \cdot e^{j2\pi \cdot nf_0 \cdot t}).$$
 (3.31)

Since balanced operation mode is of interest, the differential- and common-mode voltages and currents can be computed as [54]

$$v_{D1}(t) = v_1(t) - v_2(t) i_{D1}(t) = \frac{1}{2}[i_1(t) - i_2(t)] (3.32)$$

$$v_{D2}(t) = v_3(t) - v_4(t) i_{D2}(t) = \frac{1}{2}[i_3(t) - i_4(t)] (3.33)$$

$$v_{D2}(t) = v_3(t) - v_4(t)$$
 $i_{D2}(t) = \frac{1}{2}[i_3(t) - i_4(t)]$ (3.33)

$$v_{C1}(t) = \frac{1}{2}[v_1(t) + v_2(t)] \qquad i_{C1}(t) = i_1(t) + i_2(t)$$
(3.34)

$$v_{C1}(t) = \frac{1}{2}[v_1(t) + v_2(t)] \qquad i_{C1}(t) = i_1(t) + i_2(t)$$

$$v_{C2}(t) = \frac{1}{2}[v_3(t) + v_4(t)] \qquad i_{C2}(t) = i_3(t) + i_4(t).$$
(3.34)

3.3 Measurement results

3.3.1 Oscillators and transmitters

Load-pull measurements on self-generating devices are typically intended to find the load condition that sinks the maximum power, or that operates the power stage with the lowest distortion in order to satisfy demanding spectral masks.

Since only two ports are involved, a subset of Fig. 3.12 is used, as sketched in Fig. 3.19. The VNA phase lock is derived from the output differential signal, since the DUT and the VNA internal RF source do not share a common stable phase reference. The spectrum analyzer can be used to measure the level of spurious signals close to the carrier, or the modulation spectral regrowth.

A Bluetooth radio tranceiver model STLC2150 from STMicroelectronics was first measured. The device block schematic is shown in Fig 3.20. The device was configured as a balanced transmitter with no modulation, with frequency $f_0 =$ 2.402 GHz. The measurement were devoted to find the maximum differential output power and the minimum power of a spurious signal with frequency about 370 kHz above the carrier.

The differential-mode reflection coefficient at the fundamental frequency was tuned, and the output power and spurious signal suppression measured. The results are in Fig 3.21.

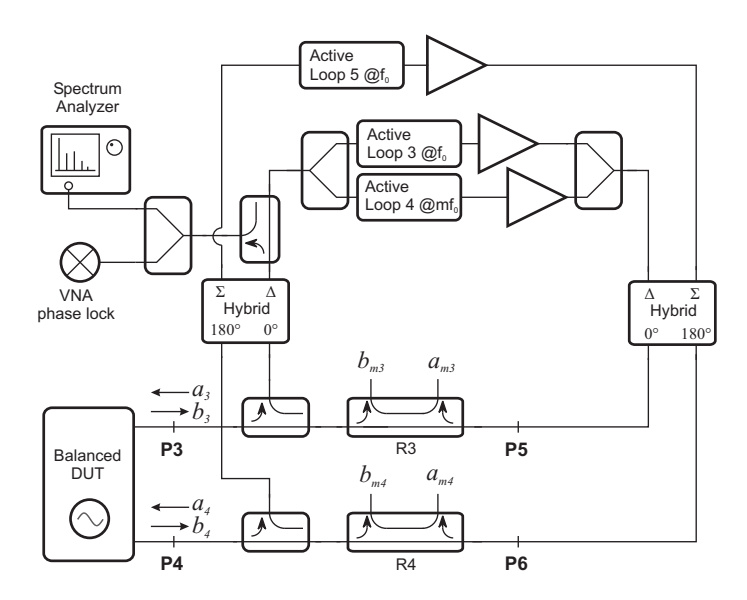


Figure 3.19. Mixed-mode load-pull bench intended for balanced transmitter characterization.

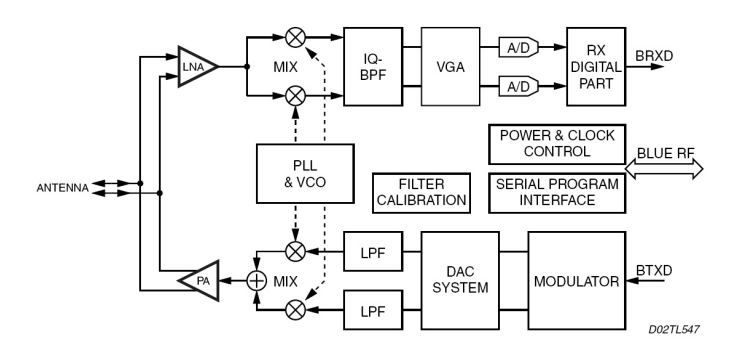


Figure 3.20. STLC2150 internal block schematic.

Further investigations showed that the spurious signal was heavily affected by the second harmonic common-mode reflection coefficient $\Gamma_{LC}(2f_0)$. A high magnitude (about 0.9) reflection coefficient was set, and its phase swept from -180° to +180°. A flat minimum was found at about -90° (Fig. 3.22), which was enough to satisfy the mask requirements for the device.

A highly mismatched transmitter for the 2.4 GHz ISM (industrial-scientific-medical) band was measured. In this case, the goal was to find the differential-mode load corresponding to the maximum power output, which, for highly mismatched devices, tends to be a steep function of the reflection coefficient, as Fig. 3.23 shows.

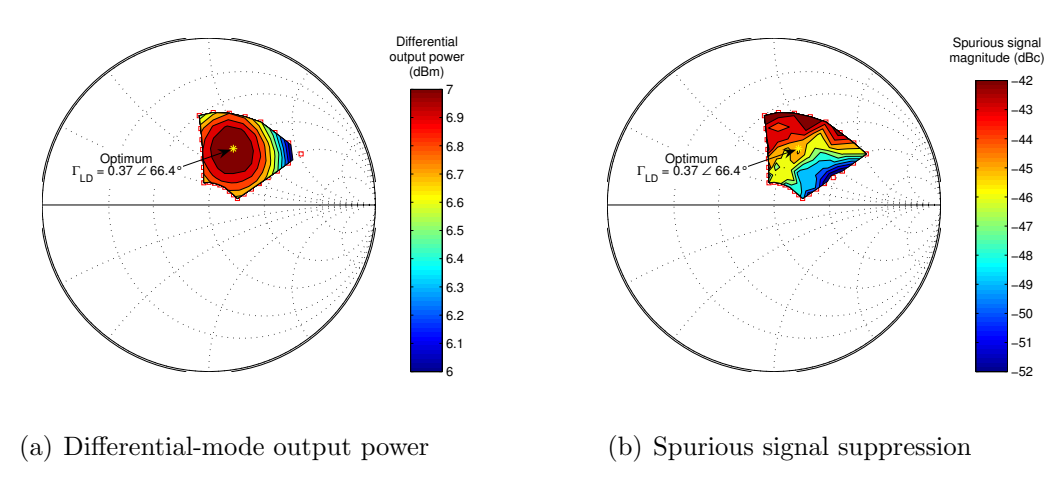


Figure 3.21. STLC2150 Load-pull maps for the differential-mode reflection coefficient at fundamental frequency $\Gamma_{LD}(f_0)$.

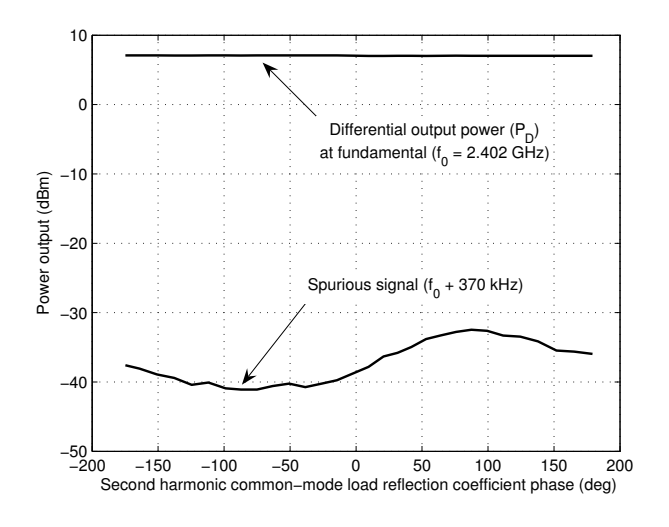


Figure 3.22. STLC2150 second harmonic common-mode reflection coefficient tuning ($|\Gamma_{LC}(2f_0)| = 0.9$).

3.3.2 Balanced Amplifiers

Balanced amplifiers have widespread diffusion both as low-noise amplifier and as power amplifiers, due to linearity advantages over the single-ended counterparts. A balanced connection is rather immune to electrical noise that might couple along the traces, and typically doubles the output voltage swing in low-voltage devices.

Recently, wideband balanced amplifiers are becoming more and more used as

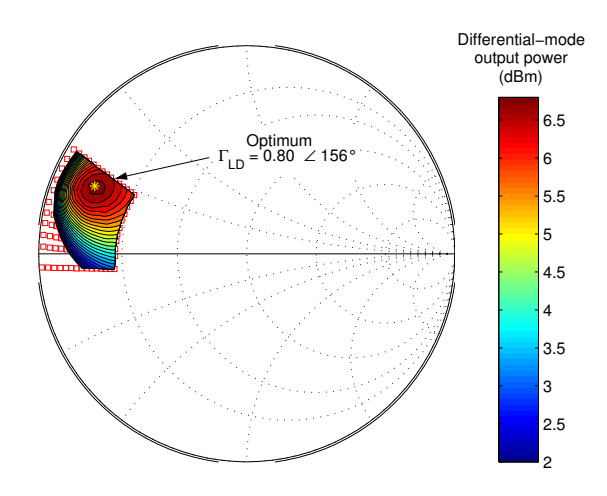


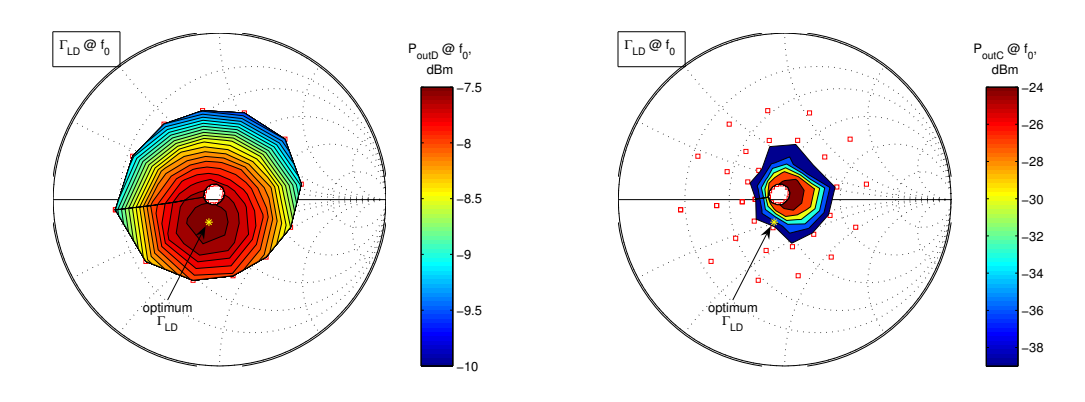
Figure 3.23. Mismatched transmitter fundamental frequency differential-mode reflection coefficient $\Gamma_{LD}(f_0)$ tuning.

drivers for high-speed and high-resolution analog-to-digital converters (ADC) or as buffers for digital-to-analog converters (DAC), which have balanced analog input or outputs. The main advantages over conventional passive baluns (e.g. a 1:4 transformer with center-tap) reside on the wider bandwidth, in the intrinsic isolation between the source or load and the converter, and, in some cases, on the possibility of electronically adjusting the gain in order to increase the analog section dynamic range.

The drawbacks are the internally generated noise and poorer linearity when compared to passive solutions. As a matter of fact, with the latest analog CMOS or high-speed bipolar technologies, the drawbacks are widely compensated by the advantages, as amplifiers with a spurious-free dynamic range (SFDR) in excess of 80 dB, noise figures lower than 10 dB and bandwidth by far greater than 1 GHz are available.

The performances of an Agilent TC226P balanced amplifier mounted on a connectorized evaluation board were measured, with focus on its non-linear behavior The measurements were performed at 2 GHz and the harmonic content was measured up to 10 GHz. Fig. 3.24 shows the results for the fundamental differential-mode load tuning. The device maximum power is reached slightly off the 100 Ω load condition, and interestingly the common-mode content drops down when reaching the optimum load condition. This fact is confirmed by the power sweep performed at the optimum load, shown in Fig. 3.25.

Fig. 3.26 shows the waveform-shaping results obtained when tuning the second harmonic differential load. In this case, the TC226 device was found to be very well



- (a) Differential-mode output power $P_{outD}(f_0)$
- (b) Common-mode output power $P_{outC}(f_0)$

Figure 3.24. TC226 differential-mode load map at fundamental (2 GHz) and at 1 dB compression point of the differential-mode gain G_D .

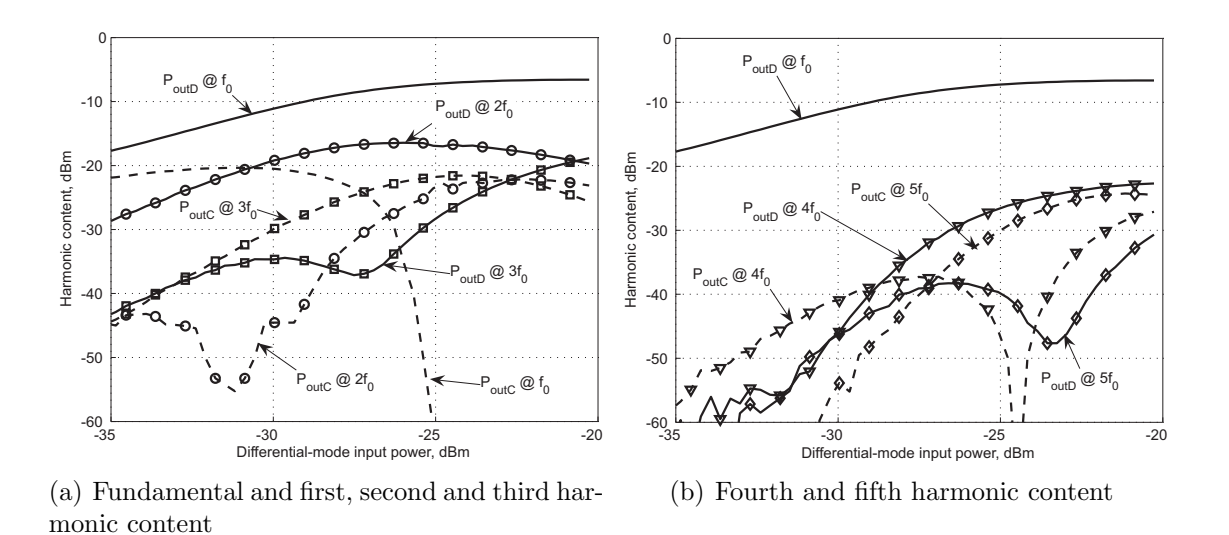


Figure 3.25. TC226 differential-mode power sweep at fundamental. The load is tuned to the optimum differential-mode reflection coefficient.

balanced. An additional tuning of the harmonic common mode loads resulted in no significative changes in the performances. This was also confirmed by analyzing the differential-mode voltage waveform, which showed no effects. The reason is found in Fig. 3.25: the second harmonic common-mode output power is 10 dB lower than the differential-mode one.

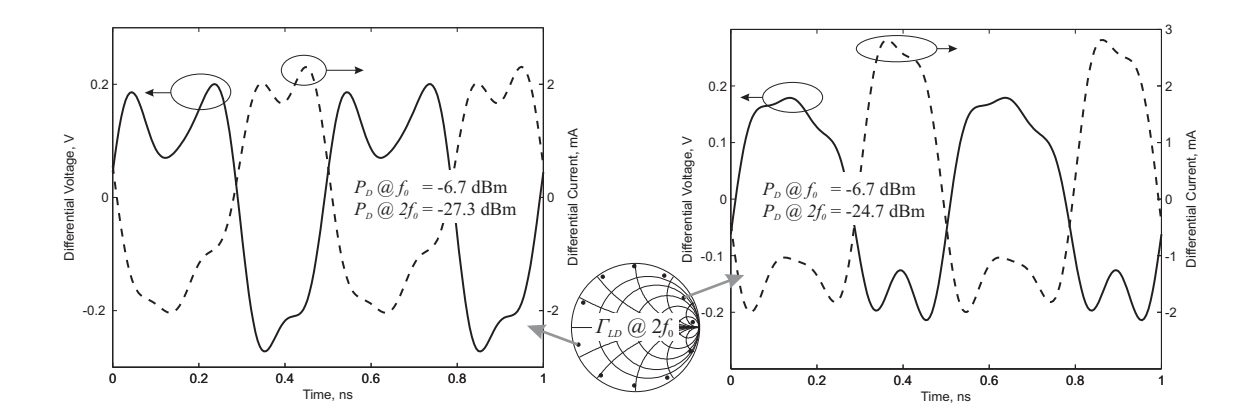


Figure 3.26. TC226 differential-mode output waveforms while sweeping the second harmonic differential-mode load. The differential load at fundamental is tuned to the maximum output power point.

3.4 Conclusions

This Chapter presented a comprehensive solution for multiport non-linear measurements. The main advantages over simpler test-sets consist on

- measurement accuracy, obtained by a rigorous vector and power calibration,
- source and load tuning, which enables straightforward use of well-established load-pull techniques for both the differential- and common-mode performances.

Future development could consist on adding modulation measurement capability, thus characterizing the DUT in terms of intermodulation distortion and spectral regrowth while tuning the load and source impedances.

Chapter 4

Thermal noise Measurement Techniques

The automatic measurement of the scattering and noise parameters of two-port amplifiers is the main subject of this Thesis, and the work lead to the development of two different test-sets.

The first system is based on the NIST NFRAD radiometer and it is described in Section 4.2, while the second is currently in use at the Politecnico di Torino and it is based on cheaper hardware, as outlined in Section 4.3.

Both systems, with completely different approaches, try to overcome some common drawbacks in present literature test-sets.

4.1 Basics

The term *electronic noise* is being used in a multitude of cases, where disturbance effects and interferences with wanted signals are of concern [70].

Besides being affected by externally-generated interferences, electronic circuits have internal sources of noise, that affect the actual output signal-to-noise ratio, as Fig. 4.1 sketches. At high frequencies, the main sources are thermal noise in passives, and shot noise in active linear devices. In both cases, the noise spectrum is relatively flat in frequency, so one generally speaks of thermal noise even for active devices.

Any device emits a certain amount of noise, depending on its physical temperature T_{phy} . A one-port passive device is described by

$$b = \Gamma a + c, \tag{4.1}$$

where c models the generated noise wave. Bosma's theorem states that the noise

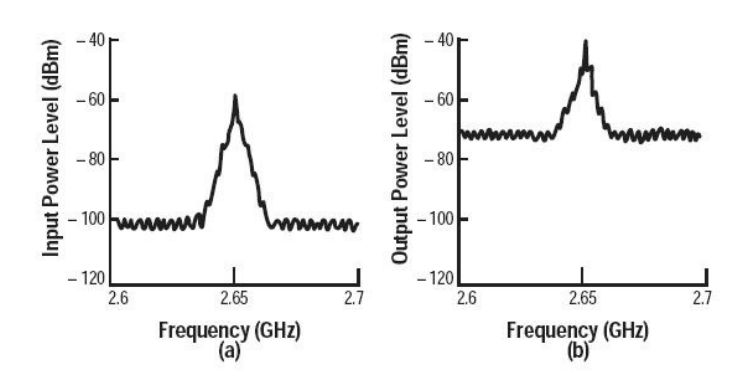


Figure 4.1. Effect of the internal noise in an amplifier. The signal-to-noise ratio at the output (b) is lower than the one at the input (a). Courtesy of Agilent [8].

wave spectral density is [22]

$$\overline{|c|^2} = k_B T (1 - |\Gamma|^2) \tag{4.2}$$

where T relates to T_{phy} by (1.13), although $T \approx T_{phy}$ is a good approximation for our purposes. The available noise power spectral density, *i.e.* the maximum power density that can be extracted from the device, is therefore given by [71]

$$k_B T = \frac{\overline{|c|^2}}{1 - |\Gamma|^2} \tag{4.3}$$

and is clearly linearly increasing with the device temperature. Because of that, the term noise temperature is often used instead of available noise power spectral density.

The generation of known noise temperatures is based on matched loads kept at constant physical temperatures. Primary standards include cryogenic loads, where the load is immersed in boiling liquid nitrogen at $T_{phy} \approx 80$ K (Fig. 4.2), ambient standards, where T_{phy} is stabilized close to the ambient temperature and accurately measured, and hot standards, usually put in an oven at 100 °C or even more, and monitored by thermocouples.

Working standards are mostly based on diode noise sources, due to cost requirements. The noise is generated by a properly designed avalanche diode which is biased at a constant current level (Fig. 4.3). The generated noise when the diode is biased (hot state) has a high spectral density, relatively constant with the frequency, which corresponds to noise temperatures T_h from about 1000 K to 10000 K, depending on the model. If no current flows through the diode (cold state) the device behave like a passive device, and emits noise proportional to its physical temperature, T_{phy} .

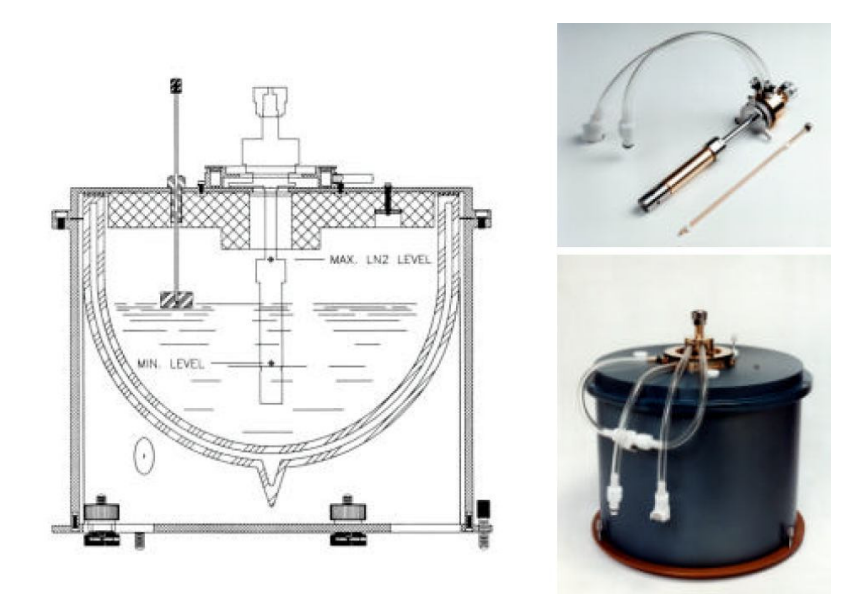


Figure 4.2. The NIST coaxial (GPC-7) cryogenic standard [9].

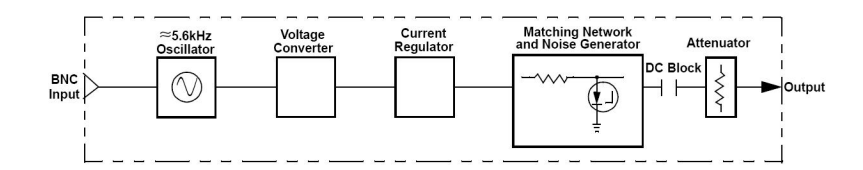


Figure 4.3. Block schematic of the Agilent 346A/B/C commercial noise diode source. Courtesy of Agilent [10].

Diode noise source are often characterized in terms of the excess noise ratio (ENR), that depends on the hot state noise temperature T_h

$$ENR_{dB} = 10\log_{10}\left(\frac{T_h - T_0}{T_0}\right) \tag{4.4}$$

where $T_0 = 290 \text{ K}$ is the reference temperature.

Diode noise source are *transfer* standards, and each source needs to be characterized, as the spread from device to device is significant. Commercial solutions are available [72], as well as calibration services from the primary calibration laboratories.

The National Institute of Standards and Technology (NIST-Boulder) has developed an accurate and relatively fast radiometer for such calibrations, which was named NFRAD [73]. The NFRAD system is a total-power radiometer, *i.e.* a noise

receiver that measures the delivered noise power of one-port coaxial devices and compares it with two noise standards, one cryogenic, one at ambient temperature. The system operates in the frequency range 1–12 GHz, in octave bands, and its block schematic is shown in Fig. 4.4.

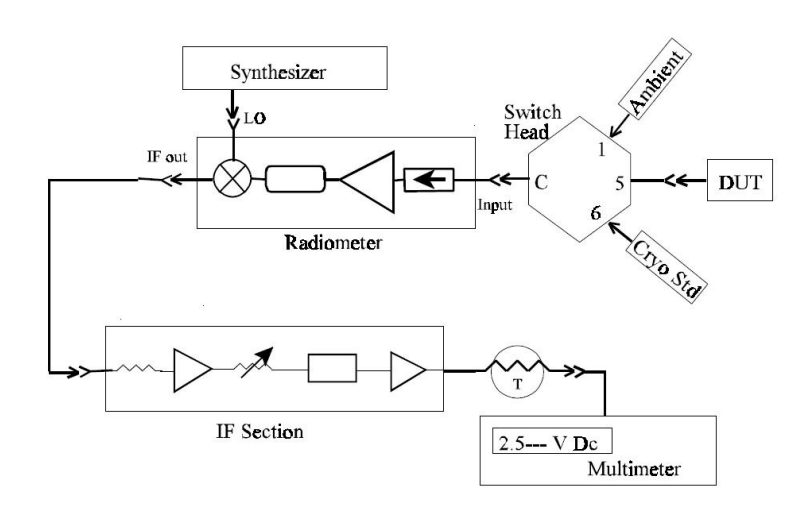


Figure 4.4. Block schematic of the NIST NFRAD radiometer.

The noise receiver down-converts the input noise spectrum close to the local oscillator frequency at an intermediate frequency (below 5 MHz). Both the upper and the lower sidebands are down-converted, since there is no preselection at RF. The IF chain greatly amplifies the noise signal, and a bolometer measures the received noise power. The system design focused on granting an extreme stability, as any gain fluctuation during the measurement would have an effect on the accuracy.

The DUT generated noise is compared with the noise produced by two primary standards, one in liquid nitrogen ($T \approx 80$ K, computed from the liquid nitrogen boiling point), the other kept close to the ambient temperature (nominally $T \approx 296$ K, monitored by a calibrated thermocouple). The schematic principle is shown in Fig. 4.5, and the DUT noise temperature is computed as [73,74]

$$T_{DUT} = T_{amb} + (T_{std} - T_{amb}) \frac{M_{std}\eta_{std}}{M_{DUT}\eta_{DUT}} \cdot \frac{Y_{DUT} - 1}{Y_{std} - 1}$$
(4.5)

where T_{amb} is the ambient standard noise temperature, T_{std} is the cryogenic standard noise temperature, η_{std} and η_{DUT} are the available gains from the cryogenic standard (plane 2) and from the DUT (plane 3) to the radiometer input (plane 0), respectively,

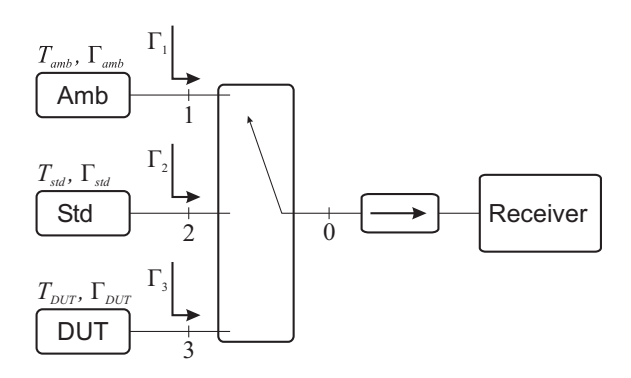


Figure 4.5. Total-power isolated radiometer block schematic.

and the mismatch factors are

$$M_{std} = \frac{(1 - |\Gamma_{std}|^2)(1 - |\Gamma_2|^2)}{|1 - \Gamma_{std}\Gamma_2|^2}$$
(4.6)

$$M_{DUT} = \frac{(1 - |\Gamma_{DUT}|^2)(1 - |\Gamma_3|^2)}{|1 - \Gamma_{DUT}\Gamma_3|^2}$$
(4.7)

being Γ_{std} and Γ_{DUT} the cryogenic standard and DUT reflection coefficients, respectively, and Γ_2 and Γ_3 the measuring system's reflection coefficients looking into planes 2 and 3, respectively.

All the measurements, excluding Γ_{DUT} , have been performed off-line and are stored as calibration factors of the radiometer. Γ_{DUT} is measured by an independent VNA just before the noise measurement.

Typical expanded (k = 2) combined uncertainty of such system is 1% for T_{DUT} , when measuring diode noise sources having $T_{DUT} > 1000$ K; a complete system description and uncertainty analysis is found in [73].

4.1.1 Noise in two-port circuits

A common figure of merit for an active linear circuit, acting as a transducer, e.g. an amplifier, is the *noise factor*, defined as

$$F \equiv \frac{SNR_{in}}{SNR_{out}} \ge 1 \tag{4.8}$$

which expresses the degradation of the output signal-to-noise ratio (SNR_{out}) due to the internally generated noise, with respect to the input one (SNR_{in}) . The noise figure is generally used to indicate the noise factor in a logarithmic scale

$$NF \equiv 10\log_{10}(F),\tag{4.9}$$

although sometimes the "noise figure" term is used for both.

The noise factor F depends on the amplifier's source termination, and it has a simple dependence with the source imittance $Y_S = G_S + jB_S$, like

$$F = F_{min} + \frac{R_n}{G_S} |Y_S - Y_{opt}|^2 \tag{4.10}$$

where F_{min} is the minimum noise factor, that depend uniquely on the device's noise properties, Y_{opt} is the optimal source immittance, that achieves the minimum noise figure, and R_n is called noise resistance and models the steepness of the curve. The same dependence can be cast in the scattering parameters representation

$$F = F_{min} + 4\frac{R_n}{Z_0} \cdot \frac{|\Gamma_{opt} - \Gamma_S|^2}{|1 + \Gamma_{opt}|^2 (1 - |\Gamma_S|^2)}$$
(4.11)

where Γ_S is the source reflection coefficient and Z_0 is the reference impedance ($Z_0 = 50 \Omega$).

In both representations, the constant noise figure curves are circles in the source termination's Smith chart plane. An example is in Fig. 4.6.

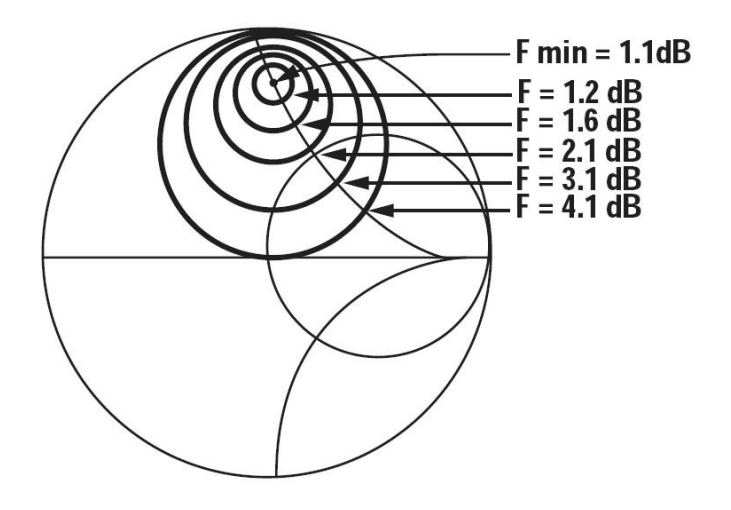


Figure 4.6. Noise circles. Courtesy of Agilent [8].

Low noise amplifiers (LNA) have typical noise figures below 1 dB, although the measurement of very low noise figures (e.g. 0.1 dB) is extremely difficult as the measurement uncertainty rarely falls below 0.1 dB.

Effective noise temperature

The widespread noise figure concept is practical when dealing with system-level design considerations, but it has a misleading nature. The noise factor definition

(4.8) is based on a ratio of two signal-to-noise ratios, but it must be pointed out that the noise figure measurement is an absolute measurement, since it characterizes the added noise power at the DUT output.

Alternatively, the DUT added noise may be expressed as an effective noise temperature, that is, the noise temperature assigned to the impedance at the input port of a DUT which would, when connected to a noise-free equivalent of the DUT, yield the same output power as the actual DUT when it is connected to a noise-free input port impedance (Fig. 4.7).

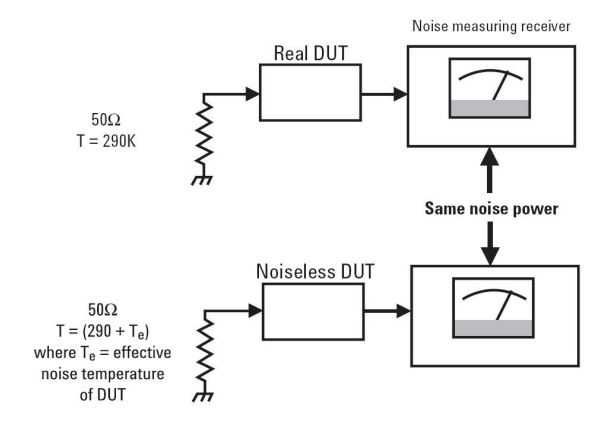


Figure 4.7. Graphical representation of the equivalent noise temperature definition. Courtesy of Agilent [11].

The effective noise temperature relates to the noise factor by

$$T_e = T_0(F - 1). (4.12)$$

Therefore, it depends on the source reflection coefficient in a similar way to F:

$$T_e(\Gamma) = T_{min} + t \frac{|\Gamma_{opt} - \Gamma_S|^2}{|1 + \Gamma_{opt}|^2 (1 - |\Gamma_S|^2)}$$
 (4.13)

$$t = 4T_0 \frac{R_n}{Z_0} (4.14)$$

where T_{min} is the minimum noise temperature, Z_0 is the reference impedance (usually 50 Ω) and the reference temperature is $T_0 = 290$ K.

Noise representation

As introduced in Section 1.2, a two-port device is described in terms of noise performances by two noise sources. Common practice is to refer the noise sources to the input port; however, this is not strictly necessary, but might be useful in the computations. Literature articles and books use a voltage and current representations, thus impedance (\mathbf{Z}) , admittance (\mathbf{Y}) , or hybrid matrices are used to model the linear device, while voltage or current noise source model the added noise, as in Fig. 4.8. [75].

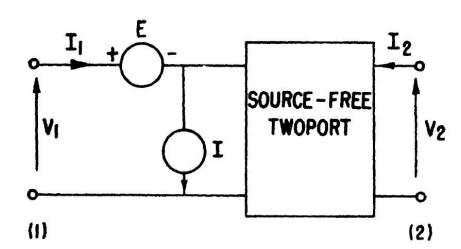


Figure 4.8. Graphical representation of a two-port noisy device.

4.1.2 Wave approach to the noise parameters determination

The IEEE noise parameters F_{min} or T_{min} , Γ_{opt} and R_n have two major disadvantages:

- 1. they are strictly defined for two-port devices, although the extension of the noise figure definition to multiport devices has been addressed by Randa in [76],
- 2. they effectively model the effect of the DUT noise, but they are not directly measurable.

To overcome these drawbacks, an intermediate noise representation could be used. Since at RF/microwave frequencies the DUT small-signal characterization is based on scattering parameters, the noise-wave approach is the most appealing.

Any linear N port device's noise can be modeled by N equivalent noise sources, as in (1.11)

$$b = Sa + c$$

where c is the noise wave vector, while S models the scattering of an equivalent noise-free device that would behave exactly as the actual device if no noise were present [18]. Generally speaking, the correlation matrix $C = \overline{cc}^{\dagger}$ fully describes the DUT noise properties, with no restriction on the number of ports.

In the two-port case, the both noise sources may be referred at the amplifier input by using the transmission matrix representation (Fig. 4.9).

The amount of amplifier-added noise is function of frequency and depends on the source impedance connected to the amplifier input. The source termination can be represented by (Fig. 4.10)

$$a_1 = \Gamma_S b_1 + c_S \tag{4.27}$$

$$a_1 \rightarrow P1 \qquad C_1 \qquad C_2 \qquad P2 \leftarrow a_2 \qquad a_1 \rightarrow P1 \qquad P2 \leftarrow a_2 \qquad a_2 \rightarrow b_2 \qquad a_1 \rightarrow b_2 \qquad a_2 \rightarrow b_2 \qquad a_2 \rightarrow b_2 \qquad a_3 \rightarrow b_2 \qquad a_4 \rightarrow b_2 \qquad a_4 \rightarrow b_2 \qquad a_5 \rightarrow b_2 \rightarrow b_2 \qquad a_5 \rightarrow b_2 \rightarrow b_$$

$$\begin{bmatrix} b_1 \\ b_2 \end{bmatrix} = \begin{bmatrix} S_{11} & S_{12} \\ S_{21} & S_{22} \end{bmatrix} \begin{bmatrix} a_1 \\ a_2 \end{bmatrix} + \begin{bmatrix} c_1 \\ c_2 \end{bmatrix} \qquad \begin{bmatrix} b_1 \\ a_1 \end{bmatrix} = \begin{bmatrix} T_{11} & T_{12} \\ T_{21} & T_{22} \end{bmatrix} \begin{bmatrix} a_2 \\ b_2 \end{bmatrix} + \begin{bmatrix} n_1 \\ n_2 \end{bmatrix}$$

$$S_{11} = T_{12}T_{22}^{-1} (4.15) T_{11} = S_{12} - S_{11}S_{21}^{-1}S_{22} (4.21)$$

$$S_{12} = T_{11} - T_{12}T_{22}^{-1}T_{21}$$
 (4.16) $T_{12} = S_{11}S_{21}^{-1}$ (4.22)

$$S_{21} = T_{22}^{-1}$$
 (4.17) $T_{21} = -S_{21}^{-1}S_{22}$ (4.23)

$$S_{22} = -T_{22}^{-1}T_{21} (4.18) T_{22} = S_{21}^{-1} (4.24)$$

$$c_1 = n_1 - S_{11}n_2$$
 (4.19) $n_1 = c_1 - T_{12}c_2$ (4.25)

$$c_2 = -S_{21}n_2 (4.20) n_2 = -T_{22}c_2 (4.26)$$

Figure 4.9. Graphical representation of a two-port noisy amplifier with (right) and without (left) the noise sources referenced to the input port.

where c_S is the generated wave, used to model the source generated noise, and,

Figure 4.10. Model for a two-port noisy amplifier connected to a noisy source.

using the conversion formulas in Fig. 4.9, the incident signal to the amplifier input at plane P1' becomes

$$a_1' = c_S + \Gamma_S n_1 - n_2 = c_S + \Gamma_S c_1 + \frac{1 - \Gamma_S S_{11}}{S_{21}} c_2$$
(4.28)

where c_S is independent from c_1 , c_2 , but there is some degree of correlation between c_1 and c_2 , so that the a'_1 intensity is (the overbar means statistical expectation)

$$\overline{|a_1'|^2} = \overline{|c_S|^2} + |\Gamma_S|^2 \overline{|c_1|^2} + |1 - \Gamma_S S_{11}|^2 \overline{|c_2/S_{21}|^2} + 2\Re[\Gamma_S (1 - \Gamma_S^* S_{11}^*) \overline{c_1(c_2/S_{21})^*}], \quad (4.29)$$

that is

$$\overline{|a_1'|^2} = N_S + N_{DUT}(\Gamma_S), \tag{4.30}$$

having defined

$$N_{S} = \overline{|c_{S}|^{2}}$$

$$N_{DUT}(\Gamma_{S}) = |\Gamma_{S}|^{2} \overline{|c_{1}|^{2}} + |1 - \Gamma_{S}S_{11}|^{2} \overline{|c_{2}/S_{21}|^{2}} + 2\Re[\Gamma_{S}(1 - \Gamma_{S}^{*}S_{11}^{*}) \overline{c_{1}(c_{2}/S_{21})^{*}}]$$

$$(4.31)$$

$$(4.32)$$

 N_{DUT} is a quadratic function of Γ_S , and, more interestingly, is a linear function of the parameters [77]

$$k_B X_1 = \overline{|c_1|^2} \tag{4.33}$$

$$k_B X_2 = |c_2/S_{21}|^2 (4.34)$$

$$k_B X_2 = \frac{|c_1|}{|c_2/S_{21}|^2}$$
 $k_B X_{12} = \frac{|c_1/S_{21}|^2}{c_1(c_2/S_{21})^*}.$
(4.34)

 X_1, X_2 and X_{12} have been called noise X-parameters [77], and have dimension of temperatures (k_B is the Boltzmann's constant). While X_1 and X_2 are real numbers, X_{12} is a complex quantity, and thus the DUT noise performances are described by four real parameters. More generally, a N-port noisy device is described by N^2 real noise parameters, as can be easily deducted being the correlation matrix Chermitian.

If a direct measurement of $\overline{|a'_1|^2}$ in (4.31) were possible, the X-parameters determination would consist on (at least) four independent measurements obtained by varying Γ_S and c_S . This measurement is not feasible, but the DUT output noise power is directly measurable, and the X-parameters can be computed as well.

Since N_{DUT} expresses the DUT added noise, the DUT equivalent noise temperature can be written as

$$T_e(\Gamma_S) = \frac{1}{k_B} \frac{N_{DUT}(\Gamma_S)}{1 - |\Gamma_S|^2} = \frac{|\Gamma_S|^2 X_1 + |1 - \Gamma_S S_{11}|^2 X_2 + 2\Re[\Gamma_S (1 - \Gamma_S^* S_{11}^*) X_{12}]}{1 - |\Gamma_S|^2}$$
(4.36)

and the conventional IEEE noise parameters can be derived from the X-parameters by the formulas published in [78]:

$$t = X_1 + |1 + S_{11}|^2 X_2 - 2\Re(X_{12}(1 + S_{11})^*)$$

$$T_{min} = \frac{X_2 - |\Gamma_{opt}|^2 [X_1 + |S_{11}|^2 X_2 - 2\Re(S_{11}^* X_{12})]}{1 + |\Gamma_{opt}|^2}$$

$$(4.37)$$

(4.38)

$$\Gamma_{opt} = \frac{\eta}{2} \left(1 - \sqrt{1 - \frac{4}{|\eta|^2}} \right) \tag{4.39}$$

$$\eta = \frac{X_2(1+|S_{11}|^2) + X_1 - 2\Re(S_{11}^*X_{12})}{X_2S_{11} - X_{12}}. (4.40)$$

4.1.3 Present measurement techniques

The present measurement scenario is characterized by a multitude of test-sets, which widely differ in complexity, but are based on few measurement techniques. The main purpose fo this Section is to draw a qualitative treatment where the strengths and weaknesses of each techniques are analyzed.

The methods share a common basis, as follows.

1. The DUT noise depends on four real parameters, which can be conveniently expressed as IEEE noise parameters T_{min} , Γ_{opt} , R_n , or as noise X-parameters X_1 , X_2 , X_{12}), or in any other meaningful representation.

The noise parameters are computed by solving a system, usually linear, formed by at least four equations. Almost all the known measurement techniques are based on sensing the DUT output noise power while varying the DUT input source termination. For each source termination position, an equation is added in the measurement system.

Great care is needed in choosing the best set of source reflection coefficient values, that improves the measurement accuracy and reduces the number of measurements [79,80].

2. The received noise power depends on the receiver's available gain-bandwidth product (BG) as

$$P_n = k_B B G (T + T_{RX}) (4.41)$$

where T is the input noise temperature to the receiver and T_{RX} is the effective receiver noise temperature. The measurement bandwidth B is chosen so that the noise spectrum is flat in that band.

The receiver noise adds to the DUT noise in the measurement. In terms of noise factors, this is expressed by the Friis formula (Fig. 4.11) [81]

$$F_{meas} = (F_{DUT} - 1) + (F_{RX} - 1)/G_{DUT}$$
(4.42)

where G_{DUT} is the DUT available gain. Therefore, the receiver's noise factor F_{RX} , which depends on the receiver's source termination by (4.11), needs to be characterized. This is usually accomplished by inserting a *thru* or low-loss device in place of the DUT, and measuring the receiver's noise parameters in the same way as the DUT measurement.

The DUT noise factor can be computed by (4.42), knowing the DUT gain and receiver's noise. This is called the *second stage correction*.

3. Due to the random nature of noise and the need for power measurements, redundant measurements and heavy averaging are often required to get satisfactory results.

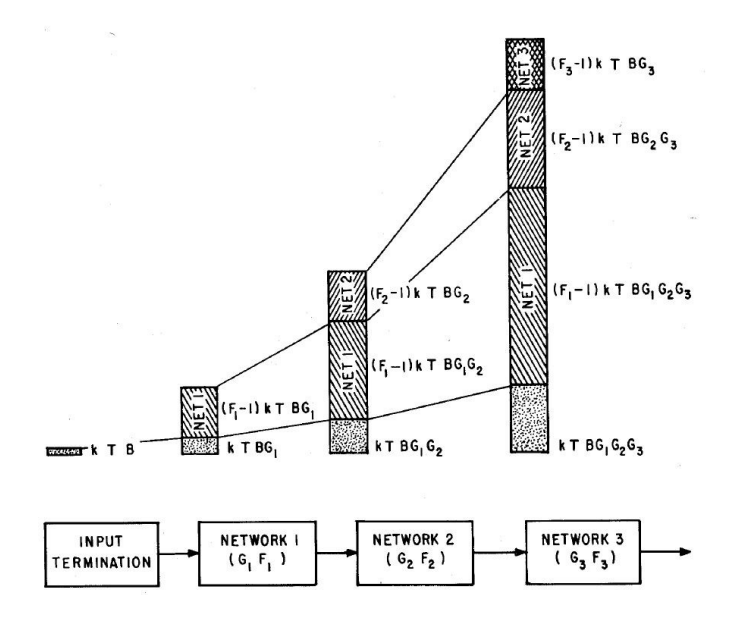


Figure 4.11. The propagation of the noise contributions in a cascade. Courtesy of Hewlett Packard [12].

Y-factor method

The Y-factor method is one of the pioneer noise measurement techniques, which was developed with focus on automatic noise figure meters [12]. Nowadays, it remains the most widely used technique.

A diode noise source is toggled on/off (hot/cold), and the noise receiver measures the noise powers in both states (Fig. 4.12). Chopping on/off the noise diode

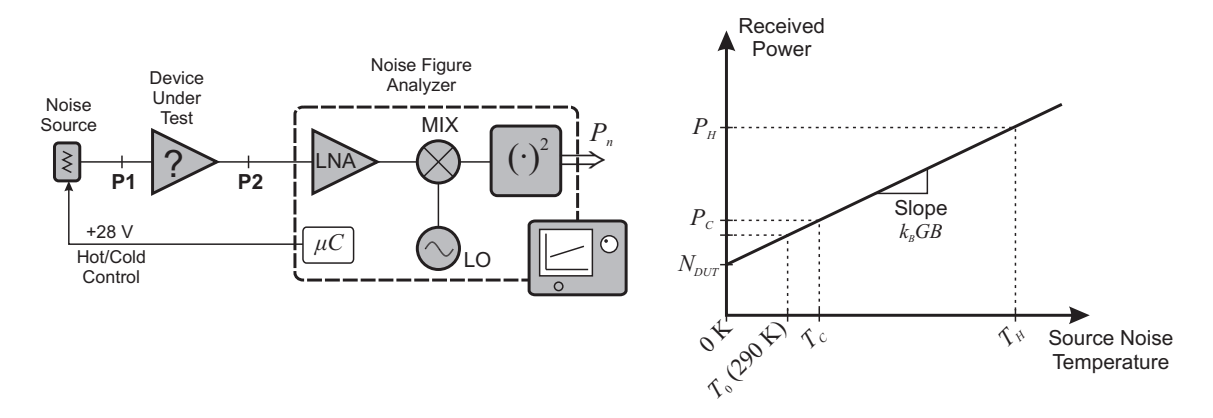


Figure 4.12. Y-factor measurement principle.

with known frequency allows to synchronously detect the measured power changes,

leading to lower measurement jitter.

The Y-factor is a ratioed measurement

$$Y \equiv \frac{P_H}{P_C} \tag{4.43}$$

which depends on the measured hot (P_H) and cold (P_C) noise powers. Being both powers proportional to the receiver's gain–bandwidth product BG, the Y-factor measurement is virtually insensitive to the receiver gain and bandwidth fluctuations.

The measured noise factor of the cascade DUT-receiver is computed as

$$F_{meas} = \frac{(T_H/T_0 - 1) - Y(T_C/T_0 - 1)}{Y - 1} \tag{4.44}$$

where $T_0 = 290$ K is the reference temperature, the hot noise temperature T_H is computed from the noise source ENR calibration table with (4.4) and the cold noise temperature $T_C \approx T_{phy}$ is close to the ambient temperature. The DUT noise factor is then computed by the second stage correction.

The DUT noise parameters are computed from a series of $F_{DUT}(\Gamma_S)$ readings, obtained by varying the noise source reflection coefficient Γ_S . This is accomplished by inserting a microwave tuner in between the noise source and the DUT input (Fig. 4.13). The drawback is that the tuner section losses need to be known in

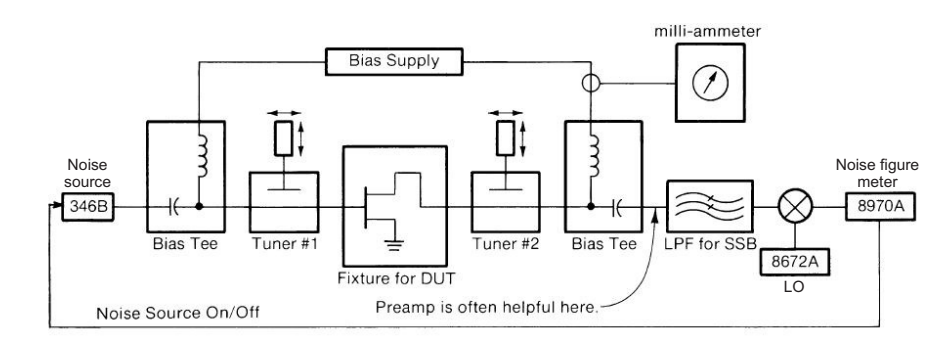


Figure 4.13. DUT noise parameter extraction by the Y-factor method. Courtesy of Hewlett–Packard [13].

order to compute the actual T_H and T_C at the DUT input port [82, 83]. Further considerations on the Y-factor method are listed in Tab. 4.1.

Hot/cold source method

In 1973, Adamian and Uhlir presented a measurement procedure that used four passive loads at ambient temperature and only one hot standard [85]. The need for a chopped diode source was eliminated.

Advantages

- 1. Ratioed measurement, no need for receiver's gain-bandwidth product measurement.
- 2. Insensitive to receiver's gain fluctuations.
- 3. Low sensitivity to DUT gain; mild dependance in the second stage correction.
- 4. Four passive source terminations required, hot/cold states.

Disadvantages

- 1. Losses in the tuner section should be carefully measured; this is not as easy as it seems [83].
- 2. Relies entirely on the noise source ENR calibration.
- 3. The noise source reflection coefficient changes in the hot and cold states; this produces a systematic error if not accounted for, although the issue can be overcome [84].
- 4. Pre-characterization of the tuner in terms of reflection coefficient and losses leads to inaccurate results.

Table 4.1. Y-factor technique strengths and weaknesses.

The hot/cold source method relies on absolute noise power measurements. The noise receiver is operated much like an extremely sensible narrow-band power meter, sensing the DUT output noise power, as sketched in Fig. 4.14.

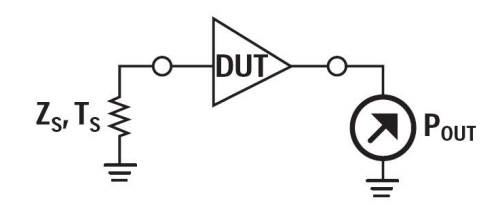


Figure 4.14. Hot/cold and cold source measurement principle. Courtesy of Agilent [8].

The receiver gain–bandwidth product BG plays a key role in determining the temperature/power scale factor, but its value cannot be computed accurately without a calibration step. It is therefore measured during the receiver calibration, using the temperature difference of the cold and hot standards [85]. The key point is that the receiver should be highly stable, as any changes in BG will result in errors in the measurement.

The advantage of the hot/cold method is its simplicity. The ambient noise sources can be connected at turn, while the hot source is inserted only once, without varying its reflection coefficient with a tuner as in the Y-factor method. This directly reflects in the measurement set-up (Fig. 4.15), which consists on a passive (electromechanical) multi-throw input switch that connects the various terminations to the DUT input [86]. A VNA is often used for measuring the DUT S-parameters,

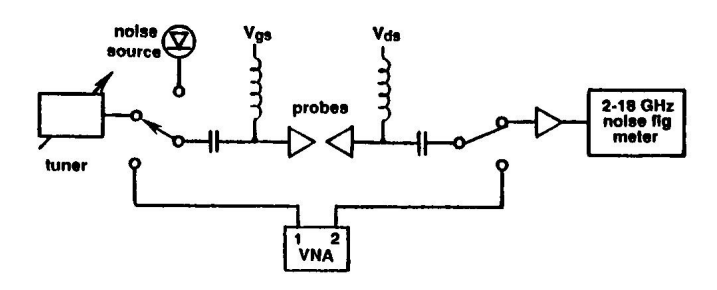


Figure 4.15. Typical hot/cold source measurement test-set.

as well as for pre-characterizing the source reflection coefficients. It is connected to the system by the input and output switches. The set-up low cost is particularly attractive, but the noise receiver requires additional efforts. A summary of the hot/cold source method is listed in Tab. 4.2.

Advantages

- 1. No need to measure the tuner section losses.
- 2. Simple set-up and calibration.
- 3. Generally stated as more accurate than the Y-factor method.
- 4. Lowest test-set cost, not accounting for the noise receiver.
- 5. Commercial and fast solutions available [87–89].

Disadvantages

- 1. The noise receiver should perform as a total-power receiver. Due to the extreme low-level noise powers, the receiver overall gain is usually in excess of 100 dB and it should be extremely stable. Gain fluctuations during the measurement directly affect the result accuracy.
- 2. Need calibration of the receiver gain—bandwidth product BG.
- 3. The DUT gain should be known.

Table 4.2. Hot/cold source technique strengths and weaknesses.

The hot/cold method is mainly used for calibrating the noise receiver, while for the DUT measurement sometimes the cold method is used.

Cold source method

The cold noise method is very similar to the hot/cold technique. The difference is the absence of a non-ambient (hot) source, since the receiver is already calibrated. This technique suits well with radiometers, although the noise receiver can be first calibrated with the hot/cold method, and then used with the cold method for the actual DUT measurement.

The DUT noise parameters are computed from the DUT output noise power readings associated with (at least) four different values of the source termination. The measurement set-up is the same as the hot/cold method, except for the hot noise source (Fig. 4.15).

The main advantage is that this method is the fastest one, as it requires the minimum number of noise source measurements. The main drawback is that both the DUT and the receiver gains play a key role during the measurement. The relevant characteristics are drawn in Tab. 4.3.

Advantages

- 1. No non-ambient source needed.
- 2. Intrinsically fast: the measurement number can be set at the very minimum (4).
- 3. Can be used in a hot/cold test-set once the receiver is calibrated. A recent example is in [89].
- 4. Simple test-set, relatively low cost.

Disadvantages

- 1. Gain fluctuations in the noise receiver.
- 2. Need for a calibrated noise receiver (gain-bandwidth product BG).
- 3. The DUT gain should be known.

Table 4.3. Cold source technique strengths and weaknesses.

4.2 The SPARRAD system at NIST

The SPARRAD system has been implemented at NIST using the NFRAD radiometer as calibrated noise receiver and a custom-made VNA test-set which provides the DUT scattering parameters measurement. The name origin is from S-PARameter and RADiometer.

Current two-port noise parameters measurements at NIST use the NFRAD radiometer as calibrated noise receiver, while the noise parameter extraction is based on a modification of the hot/cold source technique, where the hot standard is used for redundancy [50].

The NFRAD system does not include a scattering parameters measurement capability, which is handled with an independent VNA. This leads to additional measurement efforts:

- the DUT scattering parameters are measured off-line before starting the noise measurement; this requires to connect the DUT first to the VNA and then to the radiometer system, which is practical with repeatable coaxial connectors, but might become problematic for on-wafer measurements;
- any adapters used to mate the DUT connectors should be properly characterized; this applies to wafer probes as well;
- the noise parameter extraction requires multiple source terminations; these are pre-characterized by both the VNA (reflection coefficient) and by the radiometer (noise temperature); this procedure provides a consistency check since the noise temperature of passive terminations is known from their physical temperature;
- once the noise parameter measurement is started, there is no way to check for amplifier gain drifts or unrepeatable connections, which sometimes happen in on-wafer measurements.

The SPARRAD test-set in Fig. 4.16 has been devised to overcome such limitations. The system is somewhat similar to a two-port source-pull bench, with the

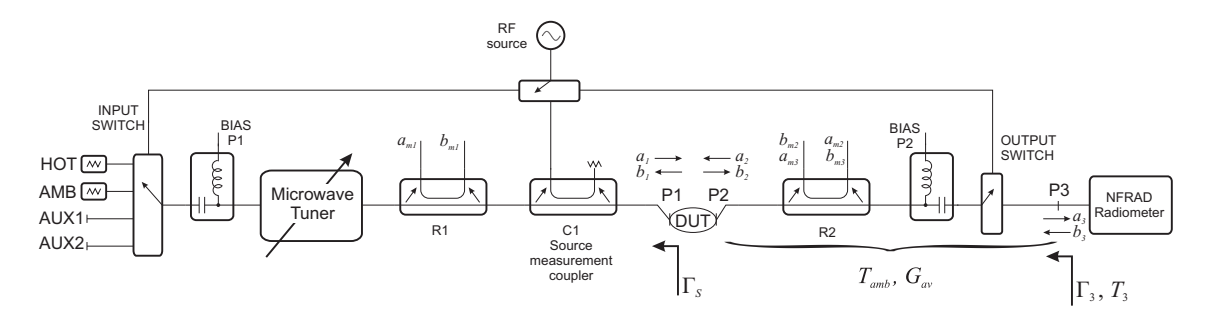


Figure 4.16. SPARRAD system block schematic.

noise receiver connected in place of the output load. The DUT is connected between planes P1 and P2, which can be either coaxial or on-wafer; two reflectometers, R1

and R2, sample the incident and reflected waves at ports 1 and 2, respectively. These waves are then routed to the VNA port 2 by a SP4T switch matrix (not shown). The RF signal drive passes through the input and output switches, which are set to connect the RF source switch.

A microwave passive tuner is inserted in the source section; in this way, the source reflection coefficient can be easily tuned. The source reflection coefficient measurement uses the source coupler C1 for the RF drive signal, while the measured waves are sampled by the R1 reflectometer.

The input switch (electromechanical) connects different noise sources during the noise measurement; typically, an ambient temperature load is used, but a built-in noise diode source is provided, and additional noise sources can be connected to AUX1 and AUX2. During the scattering parameters measurement, the input switch is set to pass the RF drive signal.

The output switch is devoted to protect the radiometer during the scattering parameters measurement, when the RF signal drive power is by far greater than the noise levels. During the noise measurement, it provides a path to the radiometer input at plane P3.

The supply bias for on-wafer transistors passes through two bias-tees.

The picture in Fig. 4.17 illustrates the hardware arrangement.

4.2.1 Scattering parameters calibration and measurement

The scattering parameters calibration is needed both for accurately measure the DUT parameters, and for characterizing the test-set losses during the noise measurement.

The system consists of three ports: two (P1 and P2) connect to the DUT, the third (P3) is an auxiliary port that connects to the NFRAD radiometer. Due to the use of a complete set of reflectometers, the complete hardware error model is used. Each port has associated four error coefficients, and (2.5), (2.6) hold:

$$a_i = -h_i a_{mi} + l_i b_{mi}$$

$$b_i = -m_i a_{mi} + k_i b_{mi}$$

where i is the port number and h_i , l_i , m_i , k_i are the error coefficients. No absolute calibration is needed, therefore the error coefficients are all normalized by k_1 .

First, an ordinary two-port calibration is performed between P1 and P2 (Fig. 4.18). The following error coefficients are thus computed:

$$\frac{h_1}{k_1}, \frac{l_1}{k_1}, \frac{m_1}{k_1}, \frac{h_2}{k_1}, \frac{l_2}{k_1}, \frac{m_2}{k_1}, \frac{k_2}{k_1}$$

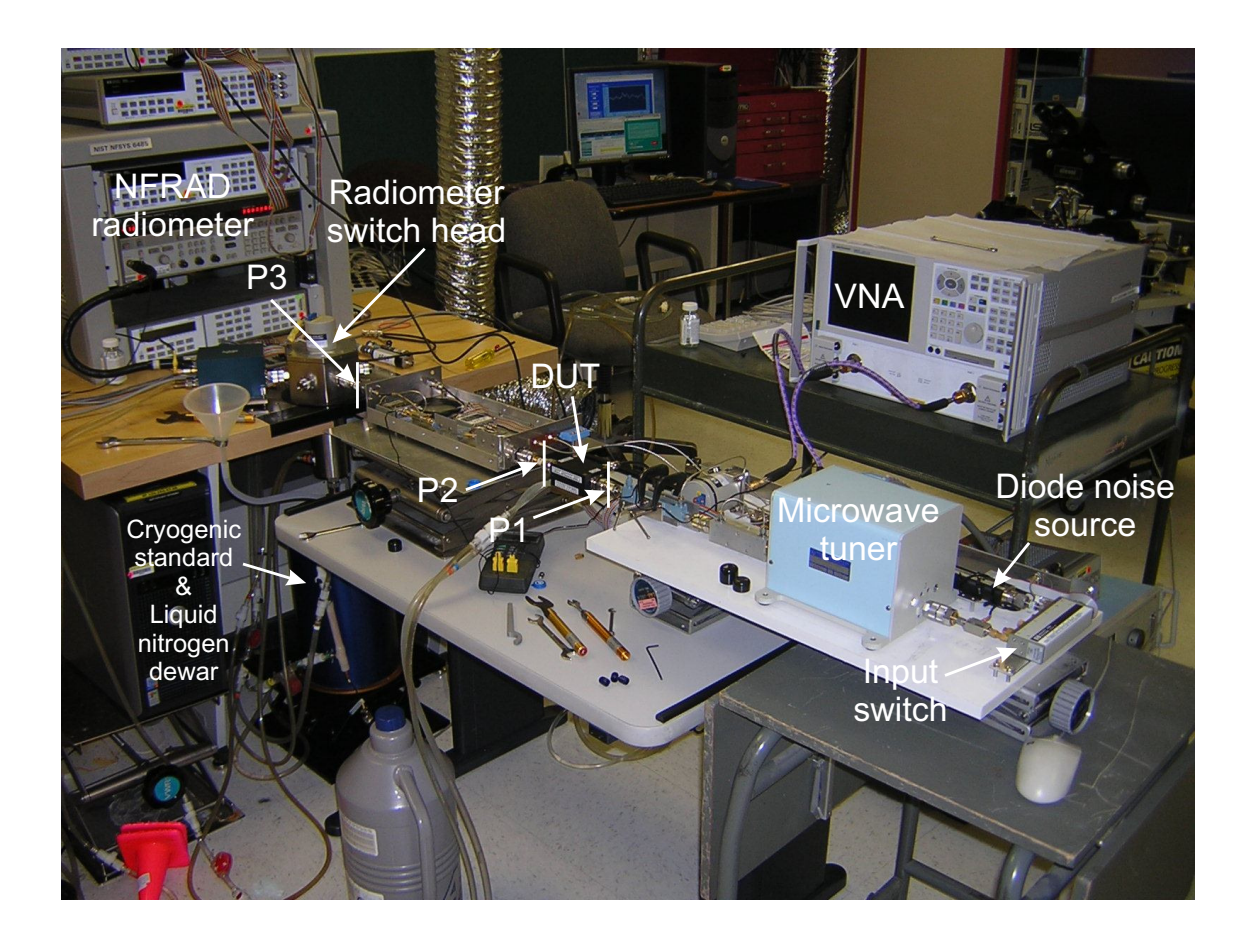


Figure 4.17. SPARRAD system picture.

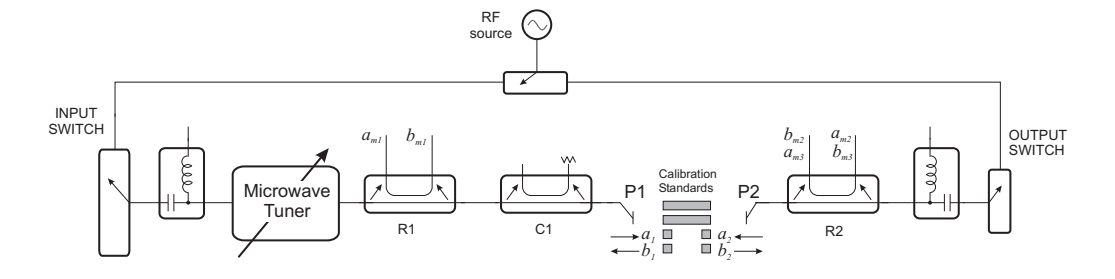


Figure 4.18. Scattering parameters calibration at P1 and P2. For clarity, unused connections are not drawn.

In this way, the DUT scattering matrix S can be computed as described in Section 2.1 using (2.1), from the incident and reflected waves measured in the two source drive conditions (P1 and P2 drive).

Then, a one-port calibration (short-open-load) is performed at the auxiliary port

P3 (Fig. 4.19). The output switch is set to P3 and the RF signal drive passes through

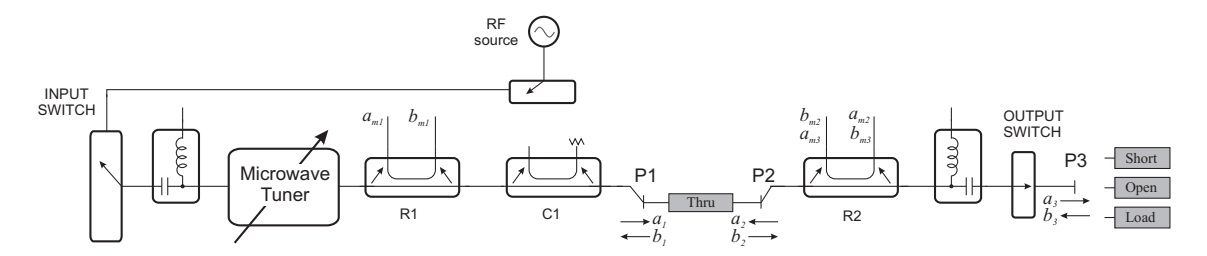


Figure 4.19. Scattering parameters calibration at P3. For clarity, unused connections are not drawn.

the input switch. The calibration computes $\frac{h_3}{k_3}$, $\frac{l_3}{k_3}$, $\frac{m_3}{k_3}$. Moreover, the scattering parameters of the P2–P3 section are computed as a by-product, employing the same technique used in load-pull systems [6].

The P2–P3 section scattering matrix S_{out} is of crucial importance during the noise measurement. Losses in this section attenuate the noise signal from the DUT output, thus the radiometer measurement does not reflect the DUT output noise temperature. The matrix S_{out} will be used to properly correct the noise levels.

4.2.2 Noise calibration and measurement

The noise parameters extraction is based on the cold source method, and requires at least four different source terminations at known temperatures.

For each tuner position k, the input switch connects the ambient load (Fig. 4.20), thus the source termination is made of passive devices kept at the same ambient temperature. Therefore, the source noise temperature is easily computed for each

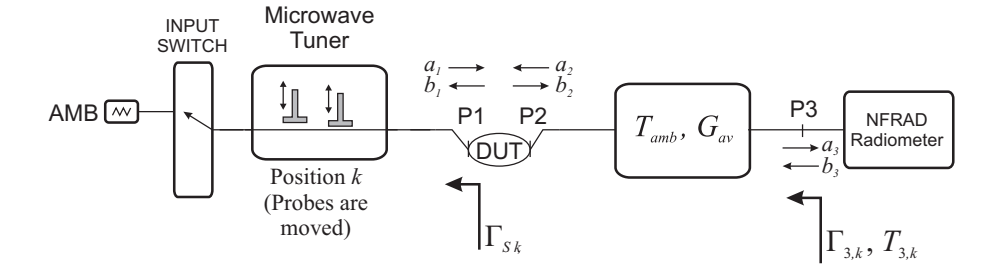


Figure 4.20. Noise parameter measurement, ambient terminations.

position.

The system is designed to allow for additional terminations, with noise temperature different from the ambient one. This redundancy improves the measurement accuracy. In this case, the tuner cannot be moved at will, since its loss would vary depending on the setting, without means of measuring it. When a non-ambient noise source is used, the tuner probes are set in a predefined position, corresponding to minimum attenuation (Fig. 4.21). The noise calibration determines the non-ambient

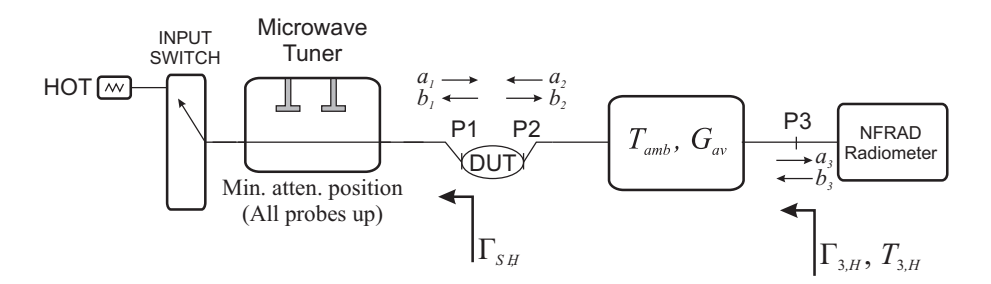


Figure 4.21. Noise parameter measurement, non-ambient terminations (internal noise diode or external sources).

sources actual noise temperatures at plane P1.

Noise calibration

The noise temperature calibration accomplishes two different tasks:

- 1. the non-ambient source noise temperatures need to be measured at plane P1;
- 2. the measured noise temperature by the radiometer (plane P3) should be referred to the DUT output (plane P2).

For the first point, both the input switch and the tuner should be highly repeatable, as any drift from the noise calibration time to the actual DUT measurement will affect the results. The tuner, of course, is not a repeatable device. Still, when the tuner slugs or probes are distant from the mainline, their effect strongly reduces. Therefore, the probes are set at one predefined position, that has the maximum distance from the mainline: the overall repeatability has been verified, and it resulted barely detectable.

The noise temperatures of the non-ambient sources are measured by inserting a thru or low-loss device between P1 and P2: the measured noise temperature T_2 at plane P2 relates to T_1 at P1 simply by

$$T_2 = G_{av}T_1 + (1 - G_{av})T_{amb} (4.45)$$

so that T_1 becomes

$$T_1 = T_2/G_{av} - (1/G_{av} - 1)T_{amb} (4.46)$$

where T_{amb} is the physical temperature of the thru device, and G_{av} its available gain

$$G_{av} = |S_{21}|^2 \frac{1 - |\Gamma_S|^2}{|1 - \Gamma_S S_{11}|^2 (1 - |\Gamma_{out}|^2)}$$
(4.47)

being S_{ij} the thru scattering parameters, Γ_S the noise source reflection coefficient at P1 and $\Gamma_{out} = S_{22} + \frac{S_{21}S_{12}\Gamma_S}{1-S_{11}\Gamma_S}$.

The problem of computing T_2 from the actual radiometer measurement T_3 at

plane P3 is handled in the same way:

$$T_2 = T_3/G_{av} - (1/G_{av} - 1)T_{amb} (4.48)$$

where now G_{av} is the P2-P3 section's available gain and T_{amb} its physical temperature. G_{av} in this case is computed from the P2-P3 section's scattering matrix S_{out} which is known from the scattering parameters calibration.

Noise measurement

The noise parameters measurement requires both scattering parameters measurements and noise temperature measurements. The measurement scheme is as follows.

- 1. The DUT S-parameters are measured.
- 2. The diode noise source is connected by the input switch and the tuner is reset in the minimum loss position
 - (a) The source reflection coefficient $\Gamma_{S,H}$ is measured
 - (b) The DUT output reflection coefficient $\Gamma_{out,H}$ is measured
 - (c) The DUT output noise temperature $T_{2,H}$ is measured
- 3. Point 2. is repeated in case additional non-ambient sources are used.
- 4. The ambient load is connected by the input switch and the tuner is moved in the k-th position
 - (a) The source reflection coefficient $\Gamma_{S,k}$ is measured
 - (b) The DUT output reflection coefficient $\Gamma_{out,k}$ is measured
 - (c) The DUT output noise temperature $T_{2,k}$ is measured
- 5. Point 4. is repeated for each user-defined tuner position
- 6. The measurements and calibration data are inserted in the linear system (4.58), which gives the DUT X_1 , X_2 , X_{12} as solution.

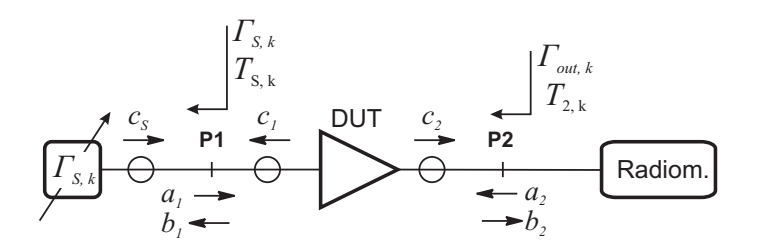


Figure 4.22. Model for the noise parameter measurement.

The measurement system is derived from the constitutive relationships of the DUT (Fig. 4.22)

$$b_1 = S_{11}a_1 + S_{12}a_2 + c_1 (4.49)$$

$$b_2 = S_{21}a_1 + S_{22}a_2 + c_2 (4.50)$$

and from the source termination's one, for the tuner position k

$$a_1 = \Gamma_{S,k} b_1 + c_{S,k}. (4.51)$$

being

$$\overline{|c_{S,k}|^2} = k_B T_k (1 - |\Gamma_{S,k}|^2). \tag{4.52}$$

When the tuner is moved (k = 1, ..., K), the source termination is passive and $c_{S,k}$ depends on the source section physical temperature $(T_k = T_{phy})$, while when the tuner is reset and the non-ambient source is connected (k = H), it becomes $T_k = T_H$, being T_H the non-ambient source noise temperature at plane P1, as measured during the noise calibration.

Equation (4.51) is substituted in (4.49) and leads to

$$b_1(1 - \Gamma_{S,k}S_{11}) = S_{12}a_2 + c_1 + S_{11}c_{S,k}$$
(4.53)

and a further substitution in (4.50) gives

$$b_2 = \Gamma_{out} a_2 + c_{out} \tag{4.54}$$

where

$$\Gamma_{out,k} = S_{22} + \frac{S_{21}S_{12}\Gamma_{S,k}}{1 - S_{11}\Gamma_{S,k}} \tag{4.55}$$

$$c_{out,k} = \frac{S_{21}}{1 - \Gamma_{S,k} S_{11}} \left[c_{S,k} + \Gamma_{S,k} c_1 + (1 - \Gamma_{S,k} S_{11}) c_2 / S_{21} \right]$$
(4.56)

and $C_{out,k}$ depends on the DUT output noise temperature $T_{2,k}$ as

$$\overline{|c_{out,k}|^2} = k_B T_{2,k} (1 - |\Gamma_{out,k}|^2). \tag{4.57}$$

The DUT output noise temperature $T_{2,k}$ at plane P2 is known from the radiometer measurement at plane P3 using (4.48). Finally, from (4.56) and from the DUT noise X-parameters definitions (4.33), (4.34) and (4.35) it follows that

$$\left| \frac{\Gamma_{S,k}}{1 - \Gamma_{S,k} S_{11}} \right|^{2} X_{1} + X_{2} + 2\Re \left(\frac{\Gamma_{S,k}}{1 - \Gamma_{S,k} S_{11}} \right) \Re(X_{12}) - 2\Im \left(\frac{\Gamma_{S,k}}{1 - \Gamma_{S,k} S_{11}} \right) \Im(X_{12}) = \frac{1 - |\Gamma_{out,k}|^{2}}{|S_{21}|^{2}} T_{2,k} - \frac{(1 - |\Gamma_{S,k}|^{2})}{|1 - \Gamma_{S,k} S_{11}|^{2}} T_{S,k}, \quad (4.58)$$

which is one row of the measurement system that has X_1 , X_2 , $\Re(X_{12})$ and $\Im(X_{12})$ as unknowns. The system is typically solved in the least-squares sense using redundant tuner positions and non-ambient standards.

4.2.3 Measurement results

The system has been carefully verified with tests and simulations during its development, but, due to shortage of time, the on-wafer capability was not tested.

A final assessment on coaxial environment was performed, comparing the SPAR-RAD results to the NIST procedure ones, described in [90]. The tested device was a 8–12 GHz low-noise amplifier. The main results are in Fig. 4.23 and 4.24. A fair agreement below 10 GHz is shown. Above that frequency, hardware limitations due to lack of directivity and small resonances in the SPARRAD system strongly affect the results. The error bars associated with the NIST measurements refer to the April 17 measurement, and are expanded combined uncertainties (k=3); the remaining NIST measurements have similar uncertainties, but these are not shown for clarity.

Although the comparison clearly shows differences due to hardware limitations, two further points should be taken into account.

- 1. The amplifier parameters have some long-term drift; for that particular device, the nominal 30 dB gain lowered of about 1 dB in one year period.
- 2. The partial inconsistence in the NIST data is mostly due to difficulties in setting uniform ambient conditions; in particular, the device physical temperature and supply voltage play a role.

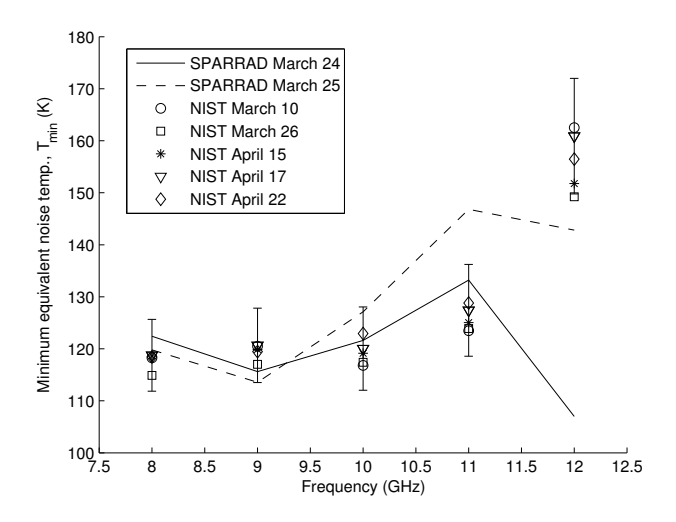


Figure 4.23. Minimum noise temperature T_{min} vs. frequency. NIST data courtesy of Dazhen Gu.

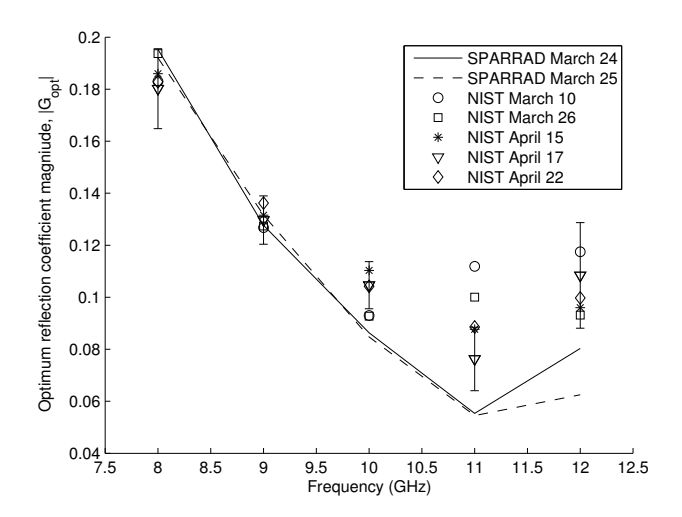


Figure 4.24. Optimum reflection coefficient G_{opt} vs. frequency. NIST data courtesy of Dazhen Gu.

4.2.4 Conclusions

The SPARRAD system has been developed and tested during February and March 2008. Due to the short time, the goal was to demonstrate the system correctness, while a thorough comparison and accuracy analysis were deferred.

During the development, two bottlenecks were found:

- the scattering parameters speed and accuracy could be improved using pindiode switches instead of electromechanical ones to route the measured waves to the VNA;
- the noise measurement speed could be greatly improved by a better refinement of the software communication between the NFRAD system (Labview-based) and the SPARRAD system (Matlab-based).

Moreover, the hardware testing evidenced small resonances due to mismatches in the components (tuner and bias-tees) which had some effect on both the scattering parameters and noise measurements. This could be improved by better components.

A final consideration regards the scattering parameters calibration accuracy. The port P3 calibration makes use of three known devices (open-short-load), which are defined by an electrical model. Especially for the open standard, the modeling is not perfect. This problem was rigorously addressed during the SPARYF system development at the Politecnico di Torino.

4.3 The SPARYF system at Politecnico di Torino

The noise bench at the Politecnico di Torino is based on the Y-factor method, and it was named SPARYF: S-PARameter and Y-Factor.

The Y-factor technique was chosen since no high-performance noise receivers were readily available, so a commercial spectrum analyzer (HP 8563E) was used. The receiver stability was simply not enough for a hot/cold or cold noise source method.

The SPARYF design addressed two issues common to present Y-factor noise measurement systems:

- 1. accurate measurement of the tuner section losses,
- 2. improving the measurement repeatability by eliminating electromechanical switches.

The work was presented in [91].

The uncertainty due to non-repeatable electromechanical switches has been completely removed by eliminating any switch along the noise signal paths, as the test-set schematic in Fig. 4.25 shows. Four directional couplers (C1, C2, C3 and C4) feed the system with the RF excitation signal through the SP4T switch SW2. The three reflectometers R1, R2 and R3 sample the incident and reflected waves at the DUT ports (planes P1, P2) and at the external ports (P3, P4). The VNA then measures the six outputs of the reflectometers by means of the SP6T pin-diode switch SW1, while the VNA reference is directly taken from the RF source signal.

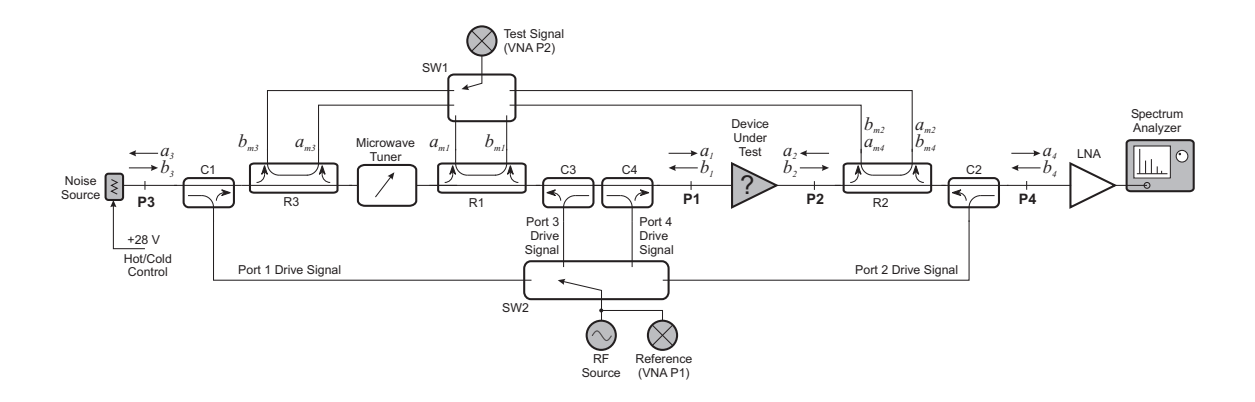


Figure 4.25. Block schematic of the SPARYF system.

The first problem, the measurement of the tuner section losses, was approached in an original way. The basic idea is to embed the tuner between two reflectometers, that sample the waves at both tuner's ports, as Fig. 4.26 shows. The noise source is

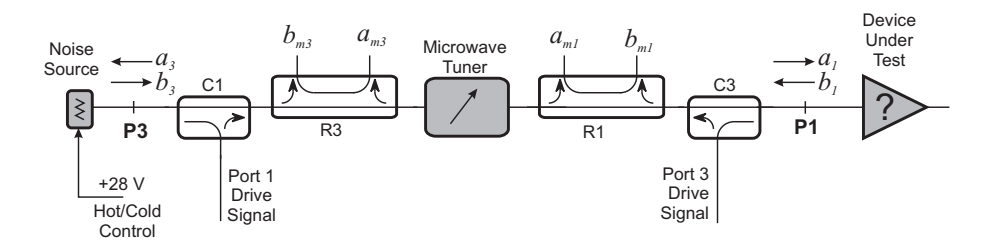


Figure 4.26. Basic block schematic for the tuner section measurement.

connected to P3, and the DUT input to P1. The microwave passive tuner is used to synthesize different source reflection coefficients at the DUT input port (plane P1).

The originality resides in the scattering parameter calibration procedure needed to accurately compute the tuner section (between P3 and P1) from the measured waves $a_{\rm m1}$, $b_{\rm m1}$, $a_{\rm m3}$ and $b_{\rm m3}$ belonging to reflectometers R1 and R3, respectively. Two directional couplers (C1 and C3) provide a path for the RF signal stimulus during the tuner measurement (Fig. 4.27).

During the DUT scattering parameters measurement only reflectometers R1 and R2 are used, being the RF drive signal sent through C1 or C2, as seen in Fig. 4.28.

During the noise measurement, the calibrated noise source is regularly switched on (hot state) and off (cold state). It generates known noise powers into the tuner section, which reach the DUT input port at P1, but are affected by attenuation and thermal noise along the path (Fig. 4.29). For each tuner position, the tuner section

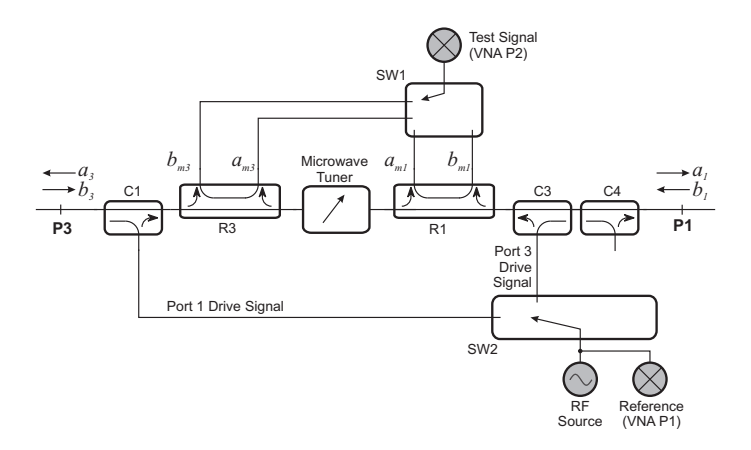


Figure 4.27. Main signal paths for the tuner section measurement. The schematic is a reduction of Fig. 4.25; for clarity, unused connections are not drawn.

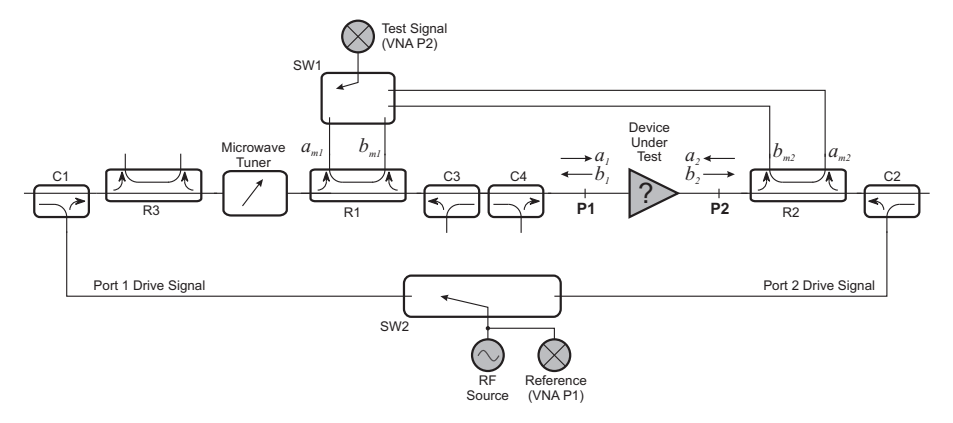


Figure 4.28. Main signal paths for the DUT S-parameters measurement. The schematic is a reduction of Fig. 4.25; for clarity, unused connections are not drawn.

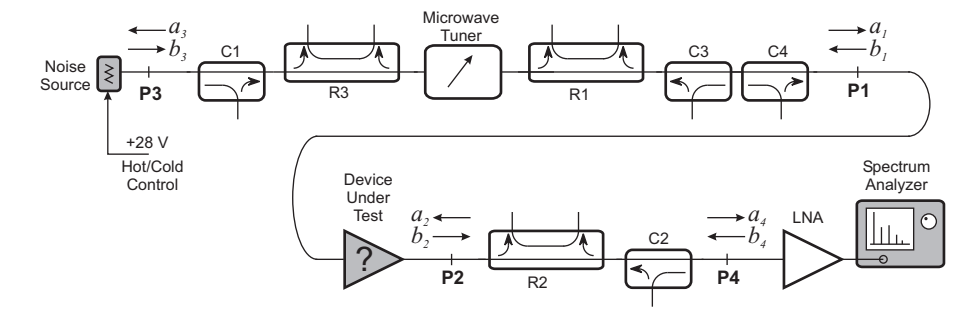


Figure 4.29. Main signal paths for the DUT noise parameters measurement. The schematic is a reduction of Fig. 4.25; for clarity, unused connections are not drawn.

losses are measured before starting the noise characterization. Thus, the hot and cold noise temperatures at plane P1 can be computed from the available losses by (4.45) and from the noise source ENR table by (4.4).

4.3.1 Scattering parameters calibration and measurement

The test-set is a multiport environment with three main ports: P1, P2 and P3. The fourth port (P4) is used during the scattering parameter calibration, but not used in the scattering and noise measurements. The key point is that the calibration takes advantage of this auxiliary port to improve the measurement accuracy of the tuner section losses.

The system uses the complete hardware error model, with four error coefficients to each port i (i = 1,2,3,4), as in (2.5) and (2.6):

$$a_i = l_i b_{mi} - h_i a_{mi}$$

$$b_i = k_i b_{mi} - m_i a_{mi}.$$

The port i error coefficients are organized in the error matrix

$$\boldsymbol{E}_{i} = \begin{bmatrix} -h_{i} & l_{i} \\ -m_{i} & k_{i} \end{bmatrix} = k_{i} \begin{bmatrix} \frac{-h_{i}}{k_{i}} & \frac{l_{i}}{k_{i}} \\ \frac{-m_{i}}{k_{i}} & 1 \end{bmatrix}, \tag{4.59}$$

and the error terms are normalized by k_1 , since no absolute power calibration is needed. Thus, the scattering parameter calibration involves 15 terms, and it is performed in three steps: the first two solve for 7 unknowns each, and the last one computes the remaining term.

Calibration at P1 and P2

The aim of this scattering calibration (Fig. 4.30) is to compute the \mathbf{E}_1/k_1 and \mathbf{E}_2/k_1 error matrices as

$$\mathbf{E}_{1}/k_{1} = \begin{bmatrix} \frac{-h_{1}}{k_{1}} & \frac{l_{1}}{k_{1}} \\ \frac{-m_{1}}{k_{1}} & 1 \end{bmatrix}, \mathbf{E}_{2}/k_{1} = \begin{bmatrix} \frac{-h_{2}}{k_{1}} & \frac{l_{2}}{k_{1}} \\ \frac{-m_{2}}{k_{1}} & \frac{k_{2}}{k_{1}} \end{bmatrix}, \tag{4.60}$$

so seven error coefficients l_1/k_1 , m_1/k_1 , h_1/k_1 and l_2/k_1 , m_2/k_1 , h_2/k_1 , k_2/k_1 are determined. This is performed by any suitable two-port calibration type.

Calibration at P3 and P4

The system needs the P3 error coefficients in order to compute the tuner section S-matrix. The P4 error coefficients are not used in any measurement. Therefore, the

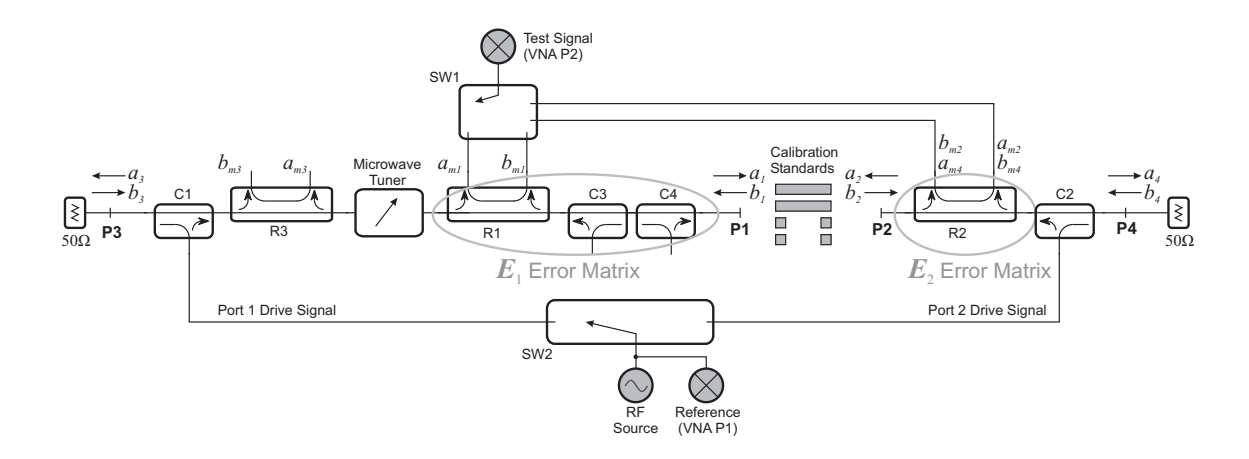


Figure 4.30. Calibration at Ports 1, 2. The schematic is a reduction of Fig. 4.25; for clarity, unused connections are not drawn.

P3 error matrix E_3/k_3 could be obtained by a simple one-port calibration (short-open-load), avoiding a two-port calibration.

In one-port calibrations, the use of fully known standards is mandatory. Unfortunately, the open standard does not suit well to be accurately modeled due to the fringing capacitance frequency dependence. The systematic error introduced by a poor modeling will bias the computed tuner losses.

A well-known solution for accurate one-port calibrations is to perform a two-port calibration and then use only the error coefficients of interest. In particular, self-calibration techniques that use unknown standards, like Multiline *thru*-reflect-line (TRL) [43], TRL [42] or line-reflect-match (LRM) [38], lead generally to the most accurate results.

This principle is used in the SPARYF system, and the P4 error coefficients are discarded. The two-port calibration (Fig. 4.31) is performed with with a *thru* device between P1 and P2. The calibration computes the E_3/k_3 and E_4/k_3 error matrices with normalization constant k_3 :

$$\mathbf{E}_{3}/k_{3} = \begin{bmatrix} \frac{-h_{3}}{k_{3}} & \frac{l_{3}}{k_{3}} \\ \frac{-m_{3}}{k_{3}} & 1 \end{bmatrix}, \mathbf{E}_{4}/k_{3} = \begin{bmatrix} \frac{-h_{4}}{k_{3}} & \frac{l_{4}}{k_{3}} \\ \frac{-m_{4}}{k_{3}} & \frac{k_{4}}{k_{3}} \end{bmatrix}.$$
(4.61)

In this case, E_3/k_3 and E_4/k_3 are not consistent with E_1/k_1 and E_2/k_1 due to the different normalization term

$$\mathbf{E}_3/k_3 = \frac{k_1}{k_3} \mathbf{E}_3/k_1, \tag{4.62}$$

and the linking coefficient k_1/k_3 is still unknown.

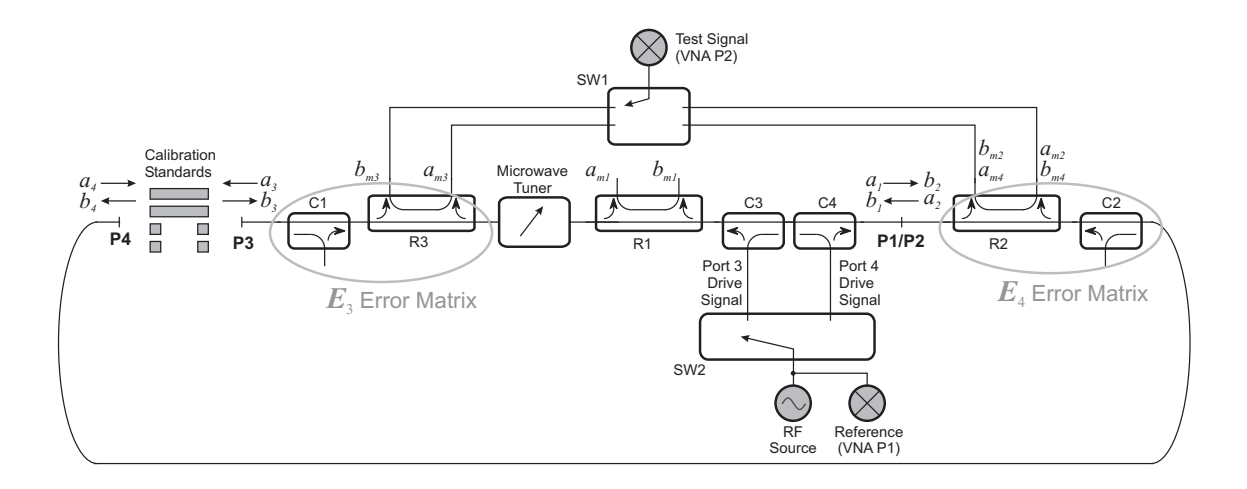


Figure 4.31. Calibration at Ports 3, 4. The schematic is a reduction of Fig. 4.25; for clarity, unused connections are not drawn.

Calibration at P1 and P3

An unknown thru [40] calibration is performed at planes P1–P3 in order to correlate the P3 error coefficients to the P1–P2 ones. The hardware model is sketched in Fig. 4.32, where two fictitious calibration planes (P5 and P6) represent the microwave tuner input and output ports.

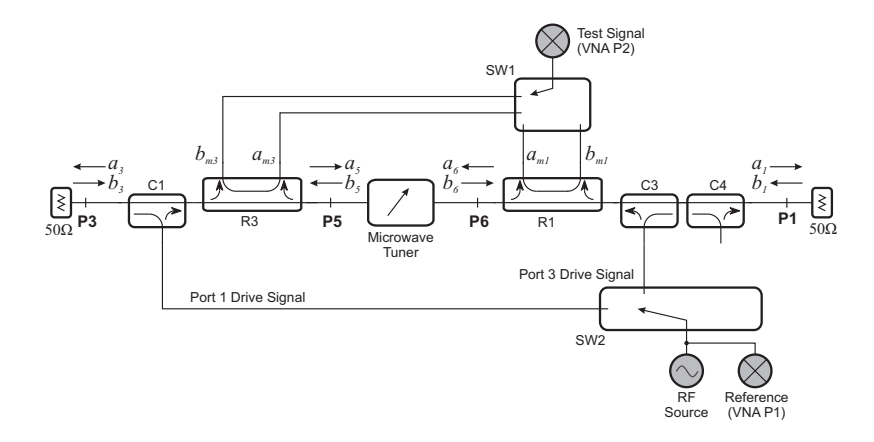


Figure 4.32. Calibration at Ports 1, 3. The schematic is a reduction of Fig. 4.25; for clarity, unused connections are not drawn.

The tuner alone is defined by the transmission matrix T'

$$\begin{bmatrix} b_5 \\ a_5 \end{bmatrix} = \mathbf{T}' \begin{bmatrix} a_6 \\ b_6 \end{bmatrix}, \tag{4.63}$$

whereas two fictitious error matrices link the waves at the tuner ports with the measured quantities

$$\begin{bmatrix} a_5 \\ b_5 \end{bmatrix} = \mathbf{E}_5 \begin{bmatrix} a_{\text{m5}} \\ b_{\text{m5}} \end{bmatrix}, \quad \begin{bmatrix} a_6 \\ b_6 \end{bmatrix} = \mathbf{E}_6 \begin{bmatrix} a_{\text{m6}} \\ b_{\text{m6}} \end{bmatrix}, \quad (4.64)$$

being the measured waves

$$a_{\rm m5} = b_{\rm m3}, \quad b_{\rm m5} = a_{\rm m3}$$
 (4.65)

$$a_{\rm m6} = b_{\rm m1}, \quad b_{\rm m6} = a_{\rm m1}.$$
 (4.66)

From (4.63) and (4.64), the measured transmission matrix $T_{\rm m}$

$$\begin{bmatrix} b_{\text{m5}} \\ a_{\text{m5}} \end{bmatrix} = \mathbf{T}_{\text{m}} \begin{bmatrix} a_{\text{m6}} \\ b_{\text{m6}} \end{bmatrix}$$

$$\tag{4.67}$$

is expressed as

$$T_{\mathrm{m}} = X[E_5]^{-1}XT'E_6, \tag{4.68}$$

where $\boldsymbol{X} = \begin{bmatrix} 0 & 1 \\ 1 & 0 \end{bmatrix}$ is a 2 × 2 permutation matrix. This is analogue to equation (4) of [40], but in our case \boldsymbol{E}_5 and \boldsymbol{E}_6 contain more than one unknown term, and so no solution can be found.

The calibration problem is solved by referencing the unknown error coefficients to the ones previously determined at P1 and P3, thus leading to an equation where only a single term (k_1/k_3) has to be determined. We define two transmission matrices, T_1 from plane P6 to P1, and T_3 from P3 to P5

$$\begin{bmatrix} a_6 \\ b_6 \end{bmatrix} = \mathbf{T}_1 \begin{bmatrix} b_1 \\ a_1 \end{bmatrix}, \quad \begin{bmatrix} a_3 \\ b_3 \end{bmatrix} = \mathbf{T}_3 \begin{bmatrix} b_5 \\ a_5 \end{bmatrix}. \tag{4.69}$$

In this way, from the error matrix definition (4.59) and (4.64)-(4.66), (4.69) \mathbf{E}_5 and \mathbf{E}_6 can be computed as

$$\boldsymbol{E}_5 = \boldsymbol{X}[\boldsymbol{T}_3]^{-1}\boldsymbol{E}_3\boldsymbol{X} \tag{4.70}$$

$$\boldsymbol{E}_6 = \boldsymbol{T}_1 \boldsymbol{X} \boldsymbol{E}_1 \boldsymbol{X}, \tag{4.71}$$

and (4.68) is rewritten as

$$\boldsymbol{T}_{\mathrm{m}} = \frac{k_{1}}{k_{3}} \left[\frac{\boldsymbol{E}_{3}}{k_{3}} \right]^{-1} \boldsymbol{T}_{3} \boldsymbol{T}' \boldsymbol{T}_{1} \boldsymbol{X} \left[\frac{\boldsymbol{E}_{1}}{k_{1}} \right] \boldsymbol{X}. \tag{4.72}$$

Finally, k_1/k_3 is computed from the determinant of T_m , being the determinants of T_1 , T' and T_3 unitary due to reciprocity

$$k_1/k_3 = \pm \sqrt{\frac{\det(\mathbf{T}_{\mathrm{m}})\det(\mathbf{E}_3/k_3)}{\det(\mathbf{E}_1/k_1)}},$$
(4.73)

and the sign ambiguity is solved by a prior knowledge of the electrical delay from plane P3 to P1.

Scattering parameter measurement

The parameters of interest are sketched in Fig. 4.33.

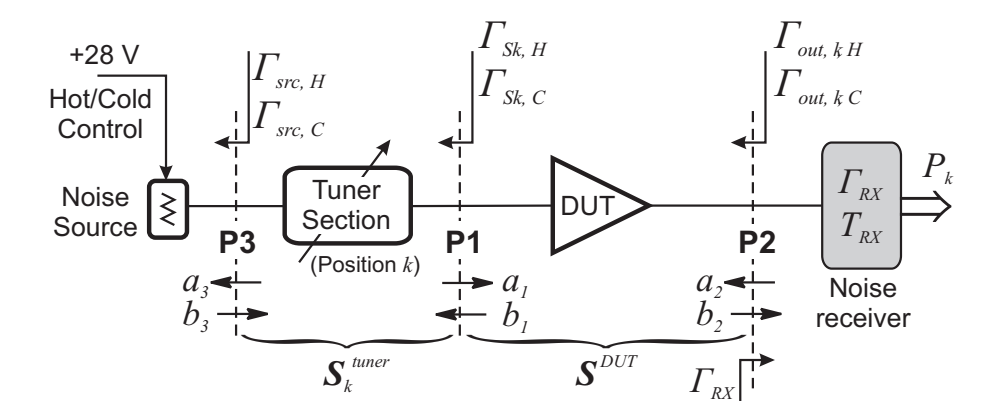


Figure 4.33. Parameters of interest during the scattering parameters measurement.

The DUT S-parameters are measured by sampling the four readings $a_{\rm m1}$, $b_{\rm m1}$, $a_{\rm m2}$ and $b_{\rm m2}$ for two different source drive signals (through couplers C1 and C2, respectively). The DUT S-matrix can be computed as

$$\mathbf{S}^{DUT} = \left[\frac{\mathbf{B}}{k_1}\right] \left[\frac{\mathbf{A}}{k_1}\right]^{-1},\tag{4.74}$$

with

$$\frac{\boldsymbol{B}}{k_1} = -\begin{bmatrix} \frac{m_1}{k_1} & 0\\ 0 & \frac{m_2}{k_1} \end{bmatrix} \boldsymbol{A}_{\mathbf{m}} + \begin{bmatrix} 1 & 0\\ 0 & \frac{k_2}{k_1} \end{bmatrix} \boldsymbol{B}_{\mathbf{m}}$$
(4.75)

$$\frac{\mathbf{A}}{k_1} = -\begin{bmatrix} \frac{h_1}{k_1} & 0\\ 0 & \frac{h_2}{k_1} \end{bmatrix} \mathbf{A}_{\mathbf{m}} + \begin{bmatrix} \frac{l_1}{k_1} & 0\\ 0 & \frac{l_2}{k_1} \end{bmatrix} \mathbf{B}_{\mathbf{m}}, \tag{4.76}$$

being the measured waves organized as

$$\mathbf{A_{m}} = \begin{bmatrix} a'_{m1} & a''_{m1} \\ a'_{m2} & a''_{m2} \end{bmatrix}$$

$$\mathbf{B_{m}} = \begin{bmatrix} b'_{m1} & b''_{m1} \\ b'_{m2} & b''_{m2} \end{bmatrix}$$
(4.77)

$$\boldsymbol{B}_{\mathbf{m}} = \begin{bmatrix} b'_{\mathbf{m}1} & b''_{\mathbf{m}1} \\ b'_{\mathbf{m}2} & b''_{\mathbf{m}2} \end{bmatrix}$$
 (4.78)

where the prime and double prime refer to the first and second RF source drive.

Similarly, the tuner section S-parameters are computed from $a_{\rm m1}$, $b_{\rm m1}$, $a_{\rm m3}$ and $b_{\rm m3}$ read in turn with the RF source driving in coupler C1 and C3. The same equations like (4.74) through (4.78) hold in this case: the subscript 2 should be substituted with 3.

When the RF drive is through C3, the noise source reflection coefficient at P3 (Γ_{src}) and the source reflection coefficient at plane P1 (Γ_S) are calculated as

$$\Gamma_{src} \equiv \frac{b_3}{a_3} \Big|_{C3} = \frac{\frac{k_3}{k_1} b_{m3} - \frac{m_3}{k_1} a_{m3}}{\frac{l_3}{k_1} b_{m3} - \frac{h_3}{k_1} a_{m3}}$$

$$(4.79)$$

$$\Gamma_S \equiv \frac{a_1}{b_1}\Big|_{C3} = \frac{\frac{l_1}{k_1}b_{m1} - \frac{h_1}{k_1}a_{m1}}{b_{m1} - \frac{m_1}{k_1}a_{m1}}.$$
(4.80)

The DUT output reflection coefficient can be measured driving from coupler C2 as

$$\Gamma_{out} \equiv \frac{b_2}{a_2} \bigg|_{C2} = \frac{\frac{k_2}{k_1} b_{m2} - \frac{m_2}{k_1} a_{m2}}{\frac{l_2}{k_1} b_{m2} - \frac{h_2}{k_1} a_{m2}}.$$
(4.81)

Finally, the noise receiver input reflection coefficient, referenced to plane P2, is calculated as

$$\Gamma_{RX} \equiv \frac{a_2}{b_2} \bigg|_{C4} = \frac{\frac{l_2}{k_1} b_{m2} - \frac{h_2}{k_1} a_{m2}}{\frac{k_2}{k_1} b_{m2} - \frac{m_2}{k_1} a_{m2}}$$

$$(4.82)$$

with RF drive through coupler C4; this is performed during the noise receiver calibration.

4.3.2 Noise calibration and measurement

The SPARRAD system is based on an extension of the Y-factor technique, that rigorously accounts for the different diode noise source reflection coefficients in the hot and cold states [84].

Noise receiver calibration model

The noise receiver calibration sets the receiver reference plane directly to the DUT output (plane P2). Its input reflection coefficient Γ_{RX} is measured by (4.82). A thru or low-loss passive device is connected in place of the DUT, as shown in Fig. 4.34.

The noise temperature $T_{out,k,L}$ at plane P2 depends on the k-th tuner position and on the noise source state (hot L = H, or cold L = C). $T_{out,k,L}$ is obtained from the P3-P2 section available gain $G_{av,k}^{32}$ as

$$T_{out,k,L} = T_{src,L}G_{av,k}^{32}(\Gamma_{src,L}) + T_{amb}\left(1 - G_{av,k}^{32}(\Gamma_{src,L})\right)$$
 (4.83)

$$G_{av,k}^{32}(\Gamma_{src,L}) = \frac{|S_{23,k}|^2}{|1 - S_{33,k}\Gamma_{src,L}|^2} \frac{1 - |\Gamma_{src,L}|^2}{1 - |\Gamma_{out,k,L}|^2}$$

$$(4.84)$$

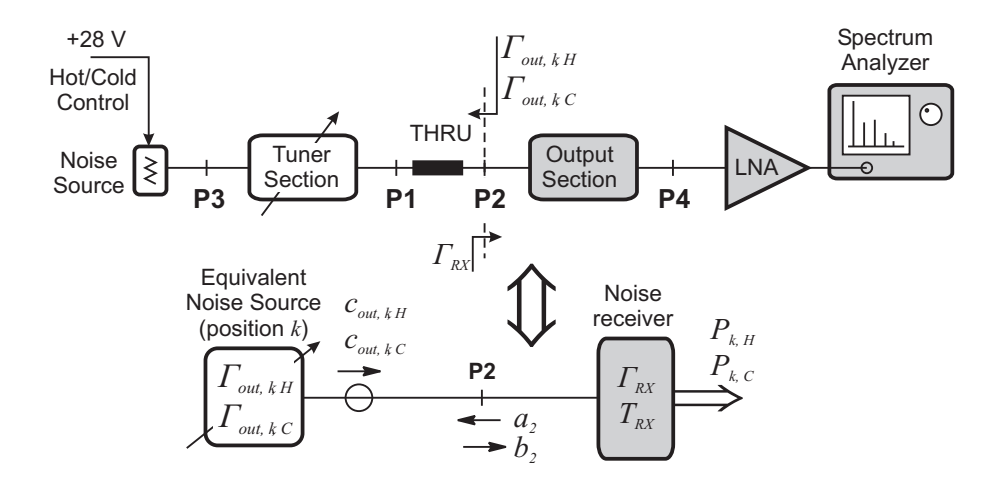


Figure 4.34. Noise receiver calibration model.

where T_{amb} is the P3-P2 section's temperature, supposed uniform, $\Gamma_{src,L}$ and $T_{src,L}$ are the noise head reflection coefficient and noise temperature, respectively. $T_{src,L}$ is known either from the ENR table (hot state) or from the physical temperature (cold state) [22]. $\Gamma_{src,L}$ is measured using (4.79). The P3-P2 scattering parameters S_{22} , $S_{23} = S_{32}$ and S_{33} are computed by cascading the P3-P1 section and P1-P2 section measured scattering matrices.

The measured noise power $P_{k,L}$ contains a contribution from the input termination, and one due to the receiver added noise

$$P_{k,L} = k_B BG(\Gamma_{out,k,L})[T_{out,k,L} + T_{RX}(\Gamma_{out,k,L})]$$
(4.85)

where the receiver's available gain G depends on its source termination. Making explicit this dependence, $P_{k,L}$ is written as

$$P_{k,L} = k_B \frac{BS_{21}^{RX} (1 - |\Gamma_{out,k,L}|^2)}{|1 - \Gamma_{out,k,L}\Gamma_{RX}|^2} [T_{out,k,L} + T_{RX}(\Gamma_{out,k,L})]$$
(4.86)

where S_{21}^{RX} is the receiver's forward gain.

The receiver's equivalent noise temperature T_{RX} is expressed in terms of X-parameters as

$$T_{RX} = \frac{|\Gamma_{out,k,L}|^2 X_1 + |1 - \Gamma_{out,k,L} \Gamma_{RX}|^2 X_2 + 2\Re(\Gamma_{out,k,L} (1 - \Gamma_{out,k,L}^* \Gamma_{RX}^*) X_{12})}{1 - |\Gamma_{out,k,L}|^2}.$$
(4.87)

The Y-factor measurement becomes

$$Y_{k} = \frac{P_{k,H}}{P_{k,C}} = \frac{(1 - |\Gamma_{out,k,H}|^{2}) \frac{T_{out,k,H} + T_{RX}(\Gamma_{out,k,H})}{|1 - \Gamma_{out,k,H}\Gamma_{RX}|^{2}}}{(1 - |\Gamma_{out,k,C}|^{2}) \frac{T_{out,k,C} + T_{RX}(\Gamma_{out,k,C})}{|1 - \Gamma_{out,k,C}\Gamma_{RX}|^{2}}}.$$
(4.88)

The calibration coefficients X_1 , X_2 , $\Re(X_{12})$ and $\Im(X_{12})$ are computed as detailed in the following "Noise parameter fitting" paragraph.

Note that if one could assume that the noise source reflection coefficient remains the same in the hot and cold states ($\Gamma_{out,k,H} = \Gamma_{out,k,C} = \Gamma_{out,k}$), equation (4.88) would result in the usual form [92]

$$Y_k = \frac{T_{out,k,H} + T_{RX}(\Gamma_{out,k})}{T_{out,k,C} + T_{RX}(\Gamma_{out,k})}.$$
(4.89)

DUT noise parameter measurement

The DUT output noise temperature is expressed as

$$T_{out,k,L} = G_{AV}(\Gamma_{Sk,L}) \left[T_{Sk,L} + T_{DUT}(\Gamma_{Sk,L}) \right] \tag{4.90}$$

where $T_{Sk,L}$ and $\Gamma_{Sk,L}$ are the source reflection coefficient and noise temperature at plane P1, respectively, and $\Gamma_{Sk,L}$ is directly measured using (4.80). $G_{AV}(\Gamma_{Sk,L})$ is the DUT available gain

$$G_{AV}(\Gamma_{Sk,L}) = \frac{|S_{21}|^2 (1 - |\Gamma_{Sk,L}|^2)}{(1 - |\Gamma_{out,k,L}|^2)|1 - S_{11}\Gamma_{Sk,L}|^2},$$
(4.91)

and $\Gamma_{out,k,L}$ is directly measured using (4.81), while the DUT equivalent noise temperature is computed as

$$T_{DUT} = \frac{|\Gamma_{Sk,L}|^2 X_1 + |1 - \Gamma_{Sk,L} S_{11}|^2 X_2 + 2\Re(\Gamma_{Sk,L} (1 - \Gamma_{Sk,L}^* S_{11}^*) X_{12})}{1 - |\Gamma_{Sk,L}|^2}.$$
 (4.92)

The source noise temperature $T_{Sk,L}$ in (4.90) is computed similarly to (4.83), using the tuner section measured losses from P3 to P1:

$$T_{Sk,L} = T_{src,L}G_{av,k}^{31}(\Gamma_{src,L}) + T_{amb}\left(1 - G_{av,k}^{31}(\Gamma_{src,L})\right)$$
(4.93)

where T_{amb} is the P3–P1 section's temperature and its available gain $G_{av,k}^{31}$ is

$$G_{av,k}^{31}(\Gamma_{src,L}) = \frac{|S_{13,k}|^2}{|1 - S_{33,k}\Gamma_{src,L}|^2} \frac{1 - |\Gamma_{src,L}|^2}{1 - |\Gamma_{Sk,L}|^2}.$$
(4.94)

The Y-factor measurement is finally given by (4.88), which is rewritten using (4.90) and (4.91) as

$$Y_{k} \frac{|1 - \Gamma_{out,k,H} \Gamma_{RX}|^{2}}{|1 - \Gamma_{out,k,C} \Gamma_{RX}|^{2}} = \frac{(1 - |\Gamma_{Sk,H}|^{2}) \frac{T'_{Sk,H} + T_{DUT}(\Gamma_{Sk,H})}{|1 - \Gamma_{Sk,H} S_{11}|^{2}}}{(1 - |\Gamma_{Sk,C}|^{2}) \frac{T'_{Sk,C} + T_{DUT}(\Gamma_{Sk,C})}{|1 - \Gamma_{Sk,C} S_{11}|^{2}}},$$
(4.95)

being

$$T'_{Sk,L} = T_{Sk,L} + \frac{T_{RX}(\Gamma_{out,k,L})}{G_{AV}(\Gamma_{Sk,L})}.$$

$$(4.96)$$

and T_{RX} is known from the noise receiver calibration. Equation (4.95) is used to compute the DUT X-parameters as shown in the following "Noise parameter fitting" paragraph.

The IEEE noise parameters can be derived from the X-parameters using (4.37), (4.38) and (4.39).

Noise parameter fitting

Since the noise parameter extraction procedure is basically the same for the noise receiver calibration and the DUT measurement, the treatment has been unified. Both equations (4.88) and (4.95) can be written in the form

$$Y_{k}' = \frac{(1 - |\Gamma_{k,H}'|^{2}) \frac{T_{k,H}' + T_{e}(\Gamma_{k,H}')}{|1 - \Gamma_{k,H}' \Gamma_{e}|^{2}}}{(1 - |\Gamma_{k,C}'|^{2}) \frac{T_{k,C}' + T_{e}(\Gamma_{k,C}')}{|1 - \Gamma_{k,C}' \Gamma_{e}|^{2}}}.$$
(4.97)

During the noise receiver calibration (equation (4.88)) the following is used: $Y'_k = Y_k$, $\Gamma'_{k,L} = \Gamma_{out,k,L}$, $T'_{k,L} = T_{out,k,L}$, $T_e = T_{RX}$ and $\Gamma_e = \Gamma_{RX}$.

For the DUT measurement (equation (4.95)) the following holds: $Y'_k = Y_k \frac{|1 - \Gamma_{out,k,H} \Gamma_{RX}|^2}{|1 - \Gamma_{out,k,C} \Gamma_{RX}|^2}$, $\Gamma'_{k,L} = \Gamma_{Sk,L}$, $T'_{k,L} = T'_{Sk,L}$, $T_e = T_{DUT}$ and $\Gamma_e = S_{11}$, where S_{11} is the DUT Sparameter.

 T_e is a function of the X-parameters as

$$T_e(\Gamma'_{k,L}) = \frac{|\Gamma'_{k,L}|^2 X_1 + |1 - \Gamma'_{k,L} \Gamma_e|^2 X_2 + 2\Re(\Gamma'_{k,L} (1 - \Gamma'^*_{k,L} \Gamma^*_e) X_{12})}{1 - |\Gamma'_{k,L}|^2}.$$
 (4.98)

Thus, a linear system with the X-parameters as unknowns is derived from (4.97); each system row looks like

$$\begin{bmatrix} A_k & B_k & C_k & D_k \end{bmatrix} \begin{bmatrix} X_1 \\ X_2 \\ \Re(X_{12}) \\ \Im(X_{12}) \end{bmatrix} = M_k$$

$$(4.99)$$

where

$$A_k = Y_k \frac{|\Gamma'_{k,C}|^2}{|1 - \Gamma'_{k,C}\Gamma_e|^2} - \frac{|\Gamma'_{k,H}|^2}{|1 - \Gamma'_{k,H}\Gamma_e|^2}$$
(4.100)

$$B_k = Y_k - 1 (4.101)$$

$$C_k = 2\Re\left(Y_k \frac{\Gamma'_{k,C}}{1 - \Gamma'_{k,C}\Gamma_e} - \frac{\Gamma'_{k,H}}{1 - \Gamma'_{k,H}\Gamma_e}\right) \tag{4.102}$$

$$D_k = -2\Im\left(Y_k \frac{\Gamma'_{k,C}}{1 - \Gamma'_{k,C}\Gamma_e} - \frac{\Gamma'_{k,H}}{1 - \Gamma'_{k,H}\Gamma_e}\right) \tag{4.103}$$

$$M_k = \frac{T'_{k,H}(1 - |\Gamma'_{k,H}|^2)}{|1 - \Gamma'_{k,H}\Gamma_e|^2} - Y_k \frac{T'_{k,C}(1 - |\Gamma'_{k,C}|^2)}{|1 - \Gamma'_{k,C}\Gamma_e|^2}.$$
 (4.104)

Typically, an accurate solution is found in the least-squares sense, being the number of tuner positions greater than four.

4.3.3 Measurement results

The tuner section measurement procedure was assessed by a comparison with an independent VNA (HP8510A). Multiline TRL calibrations were performed at ports P1–P2 and P3–P4, and at the independent VNA ports. All the connectors were 7 mm connectors, and we used the same standards (APC7 short, 10 cm and 20 cm airlines) for all calibrations.

The computed available gain is reported in Fig. 4.35 for five different tuner positions. The biggest differences near 1.5 GHz, 3 GHz, 4.5 GHz and 6 GHz are due to the poor phase margin of the standard sequence used in the multiline TRL calibrations, as at these frequencies the airlines' phase shifts approach 180°. At the other frequencies the agreement improves, and the discrepancies are deemed to belong to the connector repeatability error and calibration uncertainty.

The noise figure capability was checked by specific comparisons. Unfortunately, a reliable independent noise parameters test-set was not available, so different tests were devised to individually assess the correctness of each noise parameter.

For the minimum noise figure, a comparison was made on the 50 Ω noise figure measurements of a Mini-Circuits ZX60-6013E+ broadband amplifier, that has the optimum source reflection coefficient very close to 50 Ω . The DUT noise parameters were measured twice, in two consecutive days, by the SPARYF system and the respective 50 Ω noise figures were computed. An independent measurement performed with a 50 Ω noise system (Anritsu MS4623B) was used as reference. In all these measurements, the noise source was the same (Noise/COM NC346B). The results are plotted in Fig. 4.36, showing good agreement.

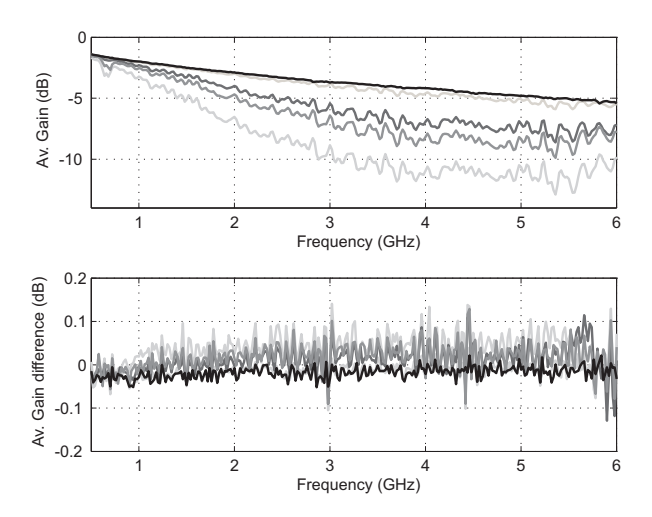


Figure 4.35. Available gain comparison for five different tuner positions.

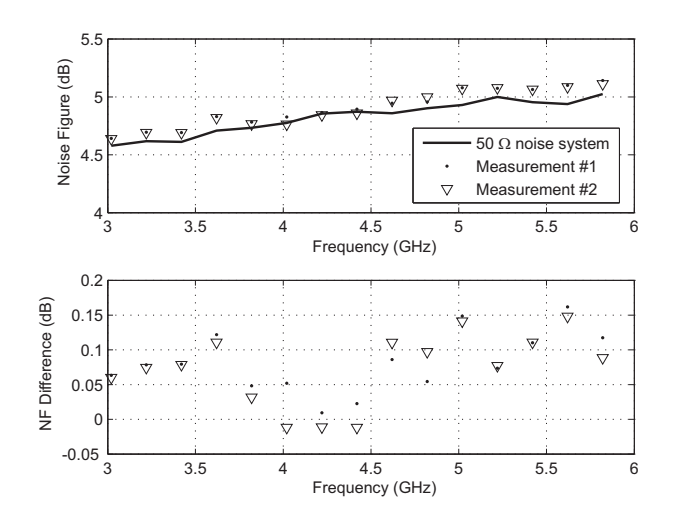


Figure 4.36. 50 Ω noise figure comparison.

Finally, the accuracy of the extracted optimum reflection coefficient Γ_{opt} and noise resistance R_n was checked. The noise behavior of a mismatched transistor was mimicked by a cascade made of a manual passive double-slug tuner, fixed to high reflection, and the amplifier used in the previous test, as sketched in Fig. 4.37.

The measured noise parameters of the amplifier alone, and the measured tuner S-parameters were used in a circuit simulator. Then the measured noise parameters

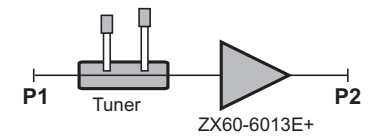
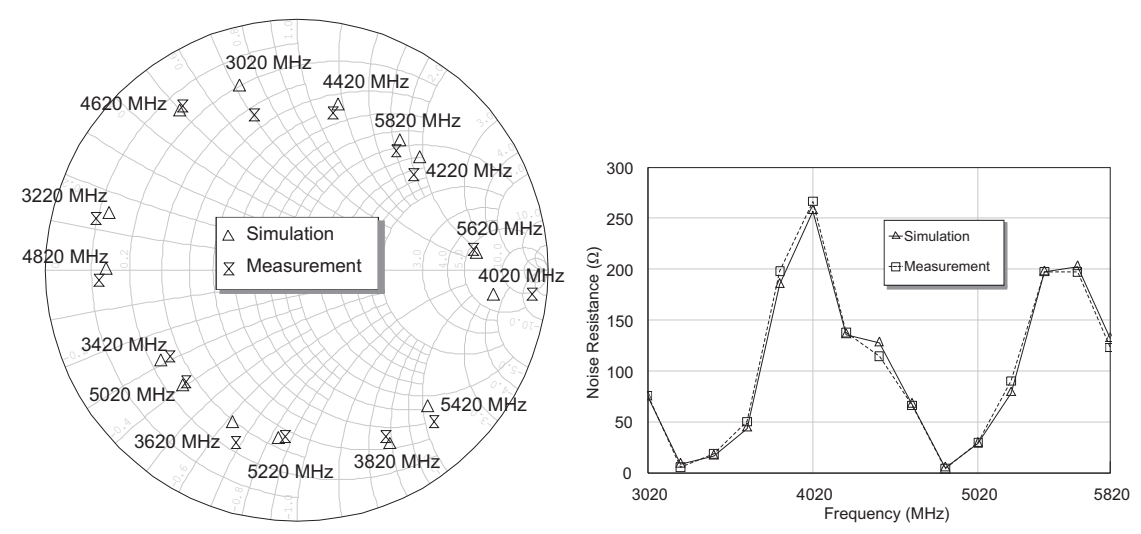


Figure 4.37. DUT used in the Γ_{opt} and R_n test.

of the cascade were compared with the simulated ones. The results are in Fig. 4.38(a) and Fig. 4.38(b), respectively.



(a) Optimum reflection coefficient Γ_{opt} vs. fre- (b) Noise resistance R_n vs. frequency of the casquency of the cascade in Fig. 4.37. cade in Fig. 4.37.

Figure 4.38. Comparison between measurement and simulation of Γ_{opt} and R_n .

4.3.4 Conclusions

The SPARYF system proposes a solution to the well-known tuner characterization and switch repeatability problems, common to many noise parameters test-set based on the Y-factor technique.

The innovative calibration solution is also a further step toward better accuracy in the SPARRAD system, where the losses between the radiometer and DUT output should be well characterized.

Currently, the main accuracy bottlenecks of the SPARYF system are

• the noise receiver, which measurement jitter should be improved; instead of the spectrum analyzer used, a commercial noise figure meter could be employed;

• the tuner section losses, that are in the order of 6–10 dB, and thus strongly attenuate the source hot noise temperature; these can be reduced with ultralow-loss directional couplers in the test-set [93].

Moreover, a noise figure meter will considerably improve the measurement speed, and lower losses might allow to use less averaging. A software routine that automatically generates a "good" set of source termination values would also be very effective.

Chapter 5

Dielectric Permittivity Measurements by Resonating Methods

The problem of electrical characterization of high-frequency dielectrics was addressed in this Thesis. A review of the present measurement techniques is carried out in this Chapter, and original contributions were found regarding resonating measurement methods.

The research work was carried on at the National Institute of Standards and Technology during Summer 2007.

5.1 Basics

The high-frequency designer is always faced with the problem of choosing appropriate materials for his project.

Of crucial importance are the dielectric properties of high-frequency printed circuit boards (PCB), that have an enormous impact on attenuation, propagation delay, characteristic impedances and crosstalk of the interconnection lines. Therefore, many measurement methods were devised to such characterization, and they differ depending on the frequency range, sample mechanical dimensions and test structure properties.

Generally speaking, most of PCB substrate have little or no magnetic properties, so that their permeability μ equals the vacuum magnetic constant μ_0 . On the contrary, their electrical properties greatly differ, as their permittivity

$$\epsilon = \epsilon'(f) + j\epsilon''(f) = \epsilon_0 \epsilon_r (1 - j \tan \delta)$$
 (5.1)

is a complex-valued function of frequency, where ϵ_0 is the vacuum electrical constant,

 ϵ_r is the relative permittivity and $\tan \delta$ is the loss tangent.

The permittivity's real part directly relates to the propagation delay of a transmission line, which for low loss transverse electromagnetic (TEM) lines takes the form

$$\tau = l \frac{\sqrt{\epsilon_r}}{c} \tag{5.2}$$

being l the line length and c the light speed in vacuum. The imaginary part ϵ'' governs the dielectric losses, which cause signal attenuation and unwanted heating in high-power circuits. The attenuation due to dielectric effects is roughly proportional to the frequency

$$A = \pi f \frac{\sqrt{\epsilon_r}}{c} (\tan \delta), \quad [A] = \text{Np/m}.$$
 (5.3)

For low-loss (tan $\delta < 10^{-3}$) RF/microwave materials the loss tangent usually has a linear (increasing) dependence with frequency, while the permittivity is either constant or mildly linearly decreasing.

Low dielectric constant materials ($\epsilon_r \approx 1-4$) are useful at higher frequency to reduce capacitive crosstalk and minimize the propagation delay; moreover, they are generally low loss. High permittivity materials ($\epsilon_r \approx 20-500$) are instead used to keep the physical dimensions small when dealing with low frequencies or to increase the capacitance of integrated capacitors.

5.1.1 High-frequency package and substrate materials

Common high-frequency materials include plastics, polymers, ceramics, glasses and crystalline materials.

Organics (plastics or polymers) are commonly used in packaging materials and are inexpensive, but have poor heat dissipation and large thermal expansion, thus they are not durable in demanding applications. PCB substrates often take advantage of composites of polymers (polytetrafluoroethylene (PTFE) and polystyrene) and other materials like glass or ceramics that improve the durability and mechanical rigidity.

Fiberglass-epoxy composites (e.g. the widely used FR-4 or the high-temperature FR-5) are low-cost laminates that are commonly used in the electronic industry for analog applications from low-frequency to RF and for the most digital applications. Laminations and woven-glass cloth cause dielectric anisotropy, i.e. the permittivity tensor normal and in-plane components differ.

Some relevant properties of common plastic composite substrates are reported in Tab. 5.1 [94], while a comparison between plastics, ceramic and glasses properties is given in Tab. 5.2 [95].

Material	ϵ_r	$\tan \delta$	Useful range of	Anisotropy
or composite	(typ.)	(typ.)	temperatures (°C)	
PTFE	2.06	0.0002	-20 to 150	no
PTFE/Fiberglass	2.25	0.0010	-20 to 150	yes
PTFE/Quartz	2.50	0.0005	-20 to 200	
PTFE/Ceramic	10.0	0.0010	-20 to 200	
Polystyrene	2.54	0.0004	-20 to 100	no
Polystyrene/Fiberglass	2.70	0.0010	-20 to 100	yes
Polystyrene/Quartz	2.70	0.0005	-20 to 100	yes
FR-4	4.3 (3.8 - 4.7)	0.02	-50 to 100	yes

Table 5.1. Typical properties of plastic substrates.

Material Class	ϵ_r	$\tan \delta$	Temp.	Metal
			expansion	adhesion
Low-K polymers	2 - 5	0.0001 - 0.01	high	poor-good
Plastic/Ceramic composites	3 - 50	0.0001 - 0.01	low	poor-good
Glasses	3 - 12	0.00005 - 0.01	low	good
Ceramics	10 - 500	0.00005 - 0.005	low	good
Ceramic/Glass composites	4 - 100	0.00005 - 0.005	low	good

Table 5.2. General properties of substrate materials.

Ceramics are particularly attractive for rugged packaging because of the low loss, good thermal conductivity and low thermal expansion. Beryllium oxide is widely used in power transistor packaging, although issues due to the material's toxicity in powder form are present.

Alumina (aluminum oxide) has been widely used as a high-frequency substrate for decades, and still remains a good choice for low-loss circuits and thin-film technology.

Low-temperature co-fired ceramics (LTCC) are gaining importance due to their ruggedness, low-loss, high permittivity, excellent thermal properties, but mainly their advantage relies in the possibility of embedding passives and conductors, as the low-temperature sintering allows to incorporate metals.

Ceramics' low loss and high permittivity are crucial for RF/microwave dielectric resonators, and for reducing the dimensions of coaxial resonators (from few hundreds MHz to 5 GHz).

5.1.2 Measurement techniques comparison

Typically, microwave substrate materials have shape of sheets, with thickness less than about 3 mm, although, for testing purposes, bulk materials may be required for machining. Metal foils are electrodeposited or are attached to PCB substrates by adhesives, and the interconnecting lines are created by an etching process.

Inexpensive test methods make use of structures machined on the metal plates. A set of microstrip or coplanar waveguides lines can be etched, and the substrate electrical properties are deducted from the measured propagation constant. This method provides a broadband characterization with realistic test structures, very similar to the actual interconnection lines [43,96].

Alternatively, more insight in the substrate loss can be gained by etching microstrip resonators. The single-frequency dielectric constant is computed from the resonance parameters, thus different resonators are needed to span the frequency band of interest.

The most accurate methods use resonant test structures in which the sample, properly machined, is inserted [97]. Most of these techniques use cavity resonators, and tend to be unpractical under 1 GHz due to mechanical dimensions. The exception is the reentrant cavity technique, that uses a TEM resonator and starts from 100 MHz [98,99].

Some widely used techniques are compared in Tab. 5.3 [95].

Technique	Field	Advantages	$U(\epsilon_r)$	$U(\tan \delta)$
Full-sheet resonance	TE_{10}	ϵ_r'	2%	n.a.
Coaxial line	TEM	broadband	1 - 10%	0.005
Waveguide	TE_{10}	broadband	1 - 10%	0.005
Capacitor	Normal E-field	low freq.	1%	10^{-4}
Cavity (TE)	TE_{01}	very accurate	0.2%	$5\cdot 10^{-5}$
		(in-plane)		
Cavity (TM)	$\mathrm{TM}_{\mathrm{0m}}$	accurate	0.5%	$5 \cdot 10^{-4}$
		(normal)		
Dielectric reson.	TE_{01}	very accurate	0.2%	$5\cdot 10^{-5}$
Coax probe	TEM, TM_{01}	nondestructive	2-10%	0.02
Fabry-Perot	TEM	high frequency	2%	0.0005

Table 5.3. Summary of dielectric substrates measurement categories, compared in terms of typical uncertainties.

Amongst the different methods, a common factor that affect the measurement accuracy is the sample's thickness uncertainty and roughness, critical for ϵ_r in thin samples. The permittivity normal component is further affected by systematic errors

arising from any air gap between the sample and the test fixture, since the test electric field is mainly normal to the sample. The air gaps can be mitigated by proper machining (like metal-plating the sample faces) or can be modeled and corrected from the measurement [100, 101].

5.1.3 Resonating techniques

Resonating methods have the greatest sensitivity to the sample's permittivity and loss tangent, and therefore these methods have the greatest resolution. Accuracy in the results is mainly due to a measurement model, which properly accounts for the systematic effects of the cavity fixture.

Most of the resonating methods compute the sample dielectric properties from the measured resonance parameters, mainly the resonant frequency f_0 and quality factor Q. The characterization is usually performed at a single frequency point, although some techniques take advantage of multiple resonating modes.

Reflection-mode cavities are one-port resonators, and the sample's properties are computed from the cavity reflection coefficient measurement. These cavities require a strong coupling with the test instrumentation, and therefore their loaded quality factor is consistently decreased, as well as their sensitivity to the sample losses.

Transmission-mode cavities have two ports, and the transmission curve is measured (Fig. 5.1). The test circuit loading effect is minimized by reducing the in-

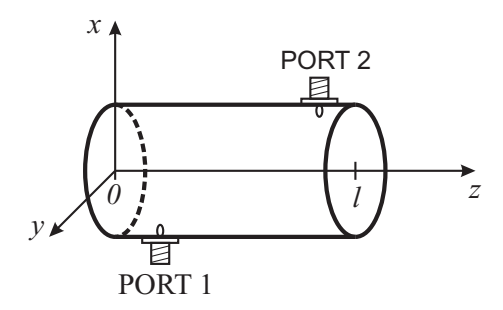
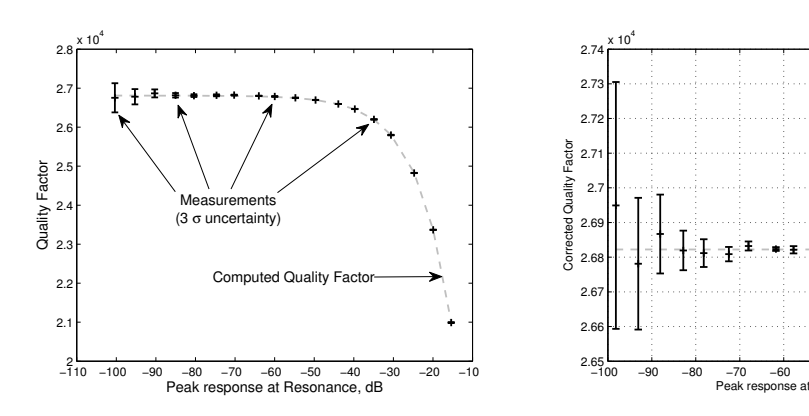


Figure 5.1. An example of transmission-mode cavity resonator.

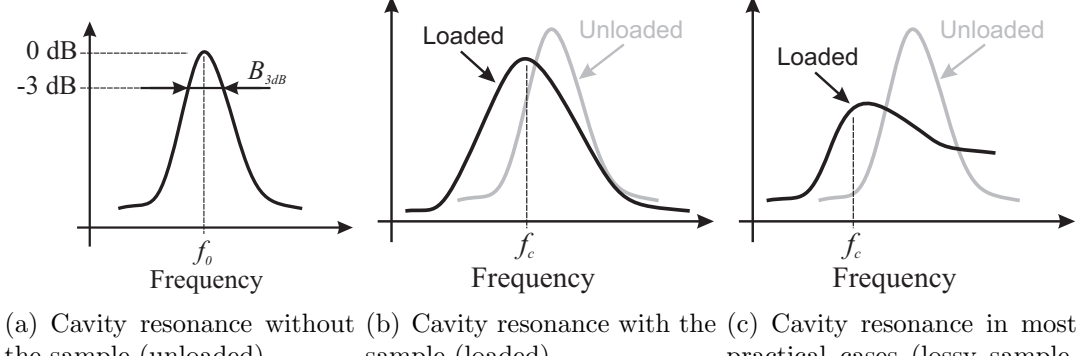
put/output couplings, thus the measured (loaded) quality factor is very close to the unloaded one, and it is possible to neglect the correction term due to the loading, as demonstrated experimentally in Fig. 5.2.

The cavity is designed for a clean resonance curve with nominal resonance frequency f_0 , as in Fig. 5.3(a). With the sample in place, the resonance peak shifts down in frequency depending on the sample's dimensions and permittivity. The loaded curve quality factor is decreased due to the additional sample's losses (Fig. 5.3(b)).



(a) Quality factor decrease due to coupling (b) Effect of the coupling losses correction. losses.

Figure 5.2. Measured quality factor ($f_0 = 10 \text{ GHz}$) vs. coupling losses.



(a) Cavity resonance without (b) Cavity resonance with the (c) Cavity resonance in most the sample (unloaded) sample (loaded) practical cases (lossy sample, distorted resonance)

Figure 5.3. Examples of measured resonance curves.

The cavity response is usually approximated by a Lorentzian curve, and the resonator is commonly modeled as a series RLC circuit with input/output transformers [102–104], as Fig. 5.4 shows. This approach is effective only for clean

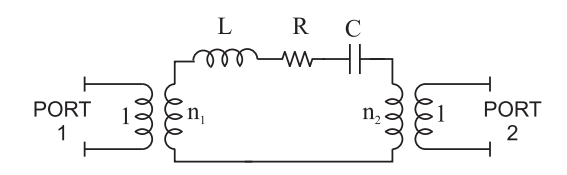


Figure 5.4. Lumped-element electrical model of a cavity resonator.

resonances, but it is a coarse approximation when asymmetric resonances are measured (as example, the one in Fig. 5.3(c)), since it assumes a single resonant mode and ignores all spurious resonances that may interfere with the primary resonance curve.

5.1.4 Resonance parameters measurements

As the permittivity and loss tangent are computed from the measured resonance parameters, accuracy in the estimation of the resonant frequency and quality factor plays a key role. The resonance parameters are generally found by fitting the measured response to the resonator model's one. Most methods are based on a clean-resonance assumption and employ a lumped-element model, like the one in Fig. 5.4.

It is not difficult to understand that, when the model assumptions break down, the resonance parameters become heavily biased. Common practice is to account for asymmetry in the resonance by increasing the electrical model complexity [105] or, sometimes more empirically, using a fitting curve with more degrees of freedom [106].

The simplest method (the "3 dB method") identifies the resonant frequency in the peak response frequency f_c and the quality factor is computed from the 3 dB bandwidth as

$$Q = \frac{f_c}{B_{3 dB}}. (5.4)$$

Such method, although very practical, gives a best uncertainty of few percent for the Q evaluation.

Moreover, being the quality factor definition

$$Q(\omega_0) \equiv \omega_0 \frac{W}{P_d} \tag{5.5}$$

where $\omega_0 = 2\pi f_0$ is the angular frequency, W is the time averaged energy stored within the cavity, and P_d is the dissipated power in the cavity, it can be demonstrated that (5.4) is approximated with distributed-elements components, and the approximation is worse as the quality factor lowers [107].

More accurate approaches parametrize the resonance curve by a fixed number of terms, and take into account the effects of asymmetry [108–111]. These parameters are then computed by linear or iterative routines, depending on the method, and finally the set is used to compute the resonance data.

Hybrid approaches make use of intermediate corrections to the measured data based on the electrical model [105, 106].

5.1.5 Split-Cylinder technique

The Split-Cylinder technique is a resonating method suited for planar samples, like uncladded microwave substrate sheets [112,113]. It consists of a cylinder resonator cut into two halves along the transversal plane (Fig. 5.5); the sample is placed in the gap between the two shorted cylindrical waveguide sections, thus the technique is non-destructive for the sample and requires no machining.

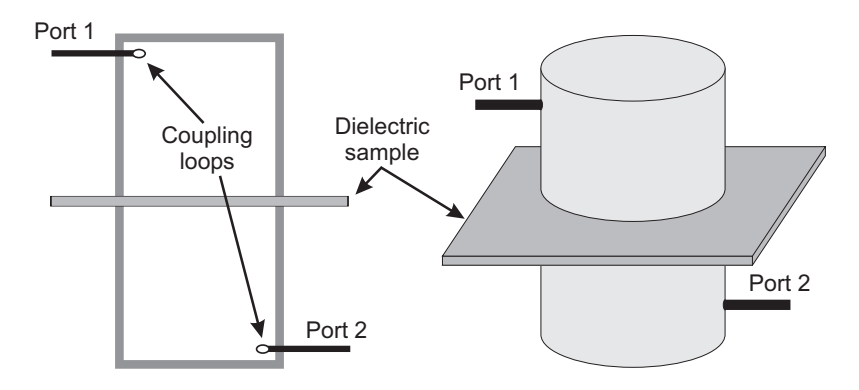


Figure 5.5. The Split-Cylinder cavity resonator.

Using multiple resonating modes TE_{0np} of the same cavity, the method offers a broad-band characterization [114,115]. An octave bandwidth is typically achieved.

Unfortunately, the mechanical advantages are paid in terms of a complex electromagnetic modeling, as the sample region is not bounded by metallic walls. The initial gap correction of Kent [114] was superseded by Janezic [116] who proposed a numerical method based on the mode-matching technique. This greatly improved the accuracy for higher resonating modes.

The method has many advantages for large-scale quality-control purposes, and has been standardized (IPC-650.2.5.5.13, [117]). Commercial solutions are also available [118].

5.2 Improvements in the resonance parameters measurement

To overcome the present limitations in the resonance parameters estimation, a general measurement model and more sophisticated numerical techniques have been devised. The achievement of this Section consists on having demonstrated that current measurement techniques are biased, and that the bias is due to the underlying model approximations that are not satisfied in many cases.

The key ideas of the new approach are simple:

- The measurement model should be as general as possible, and, since both the resonator and the measuring system are made of distributed-element components, a scattering matrix approach should be used (Fig. 5.6).
- The cavity is described by a transfer function, which can be parametrized by a certain number of poles and zeros. Although the transfer function degree is not known, the resonance poles are the ones that give information on the resonant frequency and quality factor of the considered mode.

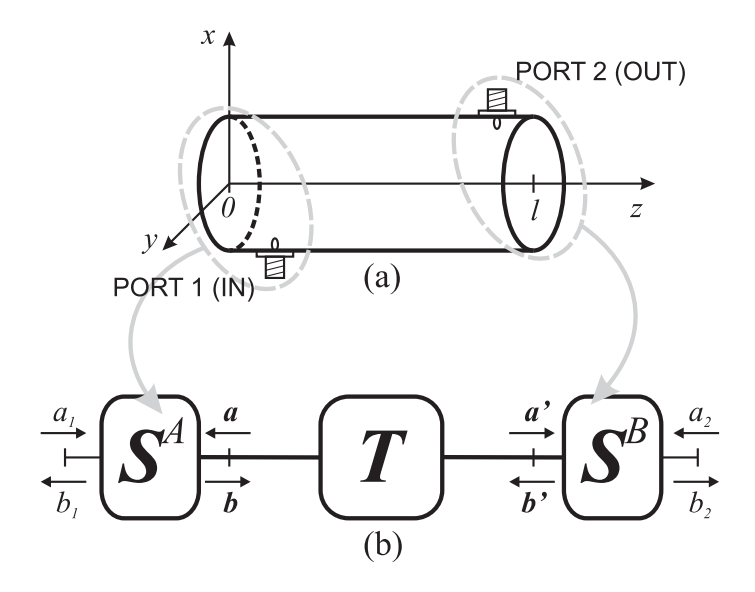


Figure 5.6. Transmission-mode cavity resonator model.

The coupling between the input/output ports and the $m \geq 1$ transversal modes in the inner cavity can be modeled by the two $(m+1) \times (m+1)$ scattering matrices \mathbf{S}^A and \mathbf{S}^B

$$\begin{pmatrix} b_1 \\ \mathbf{b} \end{pmatrix} = \begin{pmatrix} S_{11}^A & \mathbf{S}_{12}^A \\ \mathbf{S}_{21}^A & \mathbf{S}_{22}^A \end{pmatrix} \begin{pmatrix} a_1 \\ \mathbf{a} \end{pmatrix}$$
 (5.6)

$$\begin{pmatrix} \mathbf{b}' \\ b_2 \end{pmatrix} = \begin{pmatrix} \mathbf{S}_{11}^B & \mathbf{S}_{12}^B \\ \mathbf{S}_{21}^B & S_{22}^B \end{pmatrix} \begin{pmatrix} \mathbf{a}' \\ a_2 \end{pmatrix}. \tag{5.7}$$

The incident and reflected waves at port 1 and 2 are a_1 , b_1 and a_2 , b_2 , respectively, while the vectors \mathbf{a} , \mathbf{b} , \mathbf{a}' , \mathbf{b}' express the reflected and incident waves of the internal m transversal modes at the two cavity ends.

The $2m \times 2m$ transmission matrix T models the propagation effects between the left and right sides of the cavity

$$\begin{pmatrix} \mathbf{a} \\ \mathbf{b} \end{pmatrix} = \underbrace{\begin{pmatrix} \mathbf{T}_{11} & \mathbf{T}_{12} \\ \mathbf{T}_{21} & \mathbf{T}_{22} \end{pmatrix}}_{\mathbf{T}} \begin{pmatrix} \mathbf{b}' \\ \mathbf{a}' \end{pmatrix}. \tag{5.8}$$

When a dielectric sample is inserted in the cavity, T is a full matrix and depends on the sample dimensions and electrical properties as well as on the cavity dimensions, while for an empty cavity it reduces to

$$\begin{pmatrix} \mathbf{a} \\ \mathbf{b} \end{pmatrix} = \begin{pmatrix} \mathbf{E}^{-1} & \mathbf{0} \\ \mathbf{0} & \mathbf{E} \end{pmatrix} \begin{pmatrix} \mathbf{b}' \\ \mathbf{a}' \end{pmatrix}$$
 (5.9)

where

$$\mathbf{E} = \begin{pmatrix} e^{jk_{z1}l} & 0 & \dots & 0 \\ 0 & \ddots & & \vdots \\ \vdots & & e^{jk_{zi}l} & 0 \\ 0 & \dots & 0 & e^{jk_{zm}l} \end{pmatrix}$$
 (5.10)

and $k_{zi} = \beta_i - j\alpha_i$ is the longitudinal propagation constant of the *i*-th transversal mode

In the empty cavity the resonance effects can be conveniently expressed in terms of multiple reflections between S^A and S^B . As such, the resonances depend on a $m \times m$ matrix inverse

$$\mathbf{D}^{-1} = \left(\mathbf{I} - \mathbf{E}^{-1} \mathbf{S}_{22}^{A} \mathbf{E}^{-1} \mathbf{S}_{11}^{B} \right)^{-1}, \tag{5.11}$$

that, if a single mode is considered in the waveguide, becomes the well-known resonating denominator

$$D^{-1} = \left(1 - S_{22}^A S_{11}^B e^{-j2k_z l}\right)^{-1}. (5.12)$$

When a sample is inserted in the cavity, D depends also on the off-diagonal elements of T. From (5.6), (5.7) and (5.8) it is found that

$$T_{22}Da' = S_{21}^A a_1 + (S_{22}^A T_{11} - T_{21}) S_{12}^B a_2,$$
 (5.13)

where

$$D = 1 - T_{22}^{-1} \left(S_{22}^A T_{12} - T_{21} S_{11}^B + S_{22}^A T_{11} S_{11}^B \right)$$
 (5.14)

and 1 is the matrix identity.

The structure resonates when the determinant of D vanishes; the discrete and complex-valued frequencies that satisfy this condition are the cavity resonances [104, 119]

$$\widetilde{\omega}_{0n} = \omega_{0n} \left(1 + j \frac{\delta_n}{2\pi} \right) \tag{5.15}$$

where n is the resonance index (n = 1, 2, ...), ω_{0n} is the resonant frequency and δ_n expresses the damping factor of the resonating mode. The quality factor can be expressed in terms of the damping as [120]

$$Q(\omega_{0n}) = \frac{\pi}{\delta_n}. (5.16)$$

The resonance parameters can be estimated from the measured resonator's S_{21} response. Inserting (5.13) in (5.7), the S_{21} parameter is computed as

$$S_{21} = \mathbf{S}_{21}^B \mathbf{D}^{-1} \mathbf{T}_{22}^{-1} \mathbf{S}_{21}^A \tag{5.17}$$

which may approximate a Lorentzian curve in the case of a clean, high Q, resonance. However, the approximation becomes less effective as the frequency moves apart from the resonance peak due to the periodic resonances of S_{21} .

Due to the very weak coupling, only transmission measurements $(S_{21} = S_{12})$ give useful information, while the reflection parameters (S_{11}, S_{22}) don't have a measurable dependence on the system poles in \mathbf{D}^{-1} .

5.2.1 Resonance parameters estimation

Considering a single transversal mode in the empty cavity, the S_{21} resonator transfer function can be expressed as

$$S_{21} = \frac{S_{21}^A S_{21}^B e^{-jk_z l}}{1 - S_{22}^A S_{11}^B e^{-j2k_z l}}$$

$$(5.18)$$

which suggests to use a Padé approximant with polynomial basis function $x(\omega) = e^{-j\omega T}$, due to the similarity to the model¹:

$$S_{21}(\omega) = \frac{\sum_{i=0}^{M_1} b_i e^{-j\omega T i}}{\sum_{i=0}^{M_2} a_i e^{-j\omega T i}} + n(\omega)$$
 (5.19)

where $a_0 = 1$ due to normalization, the polynomial numerator and denominator degrees are M_1 and M_2 , respectively, and $n(\omega)$ models the fitting residuals.

If the estimated transfer function would track perfectly the actual one, the residuals would correspond to the measurement noise. A fair assumption is to deal with a white Gaussian noise with zero mean and power spectral density P_n flat in frequency. Actually, the noise figure of the measuring system depends on the source impedance [121], but, since a network analyzer is used and its directional bridges at each port are usually quite lossy, the measurement noise is rather independent on the measurand frequency variations.

 $^{^{1}}e^{-j2k_{z}l} = e^{-2\alpha l}e^{-j\omega\frac{2l}{v_{p}}}$, being v_{p} the phase velocity.

The transfer function approach is widely used to generate electrical models from measured data. For example, the multiport electrical model of packages can be extracted from wideband S-parameters measurements, and a good variety of fitting algorithms is published [122–128]. Little use is found in the field of resonating measurements of materials [129]. Our application differs from the literature cases, as the measurement frequency band is usually very narrow, and unfortunately the measurement signal-to-noise ratio is limited by the very low transmission coupling.

For sake of simplicity, a simple linear least-squares solution was adopted, and the poles and zeros can be numerically computed as polynomial roots from the numerator and denominator polynomials. The solution was found to be very effective and reliable in this kind of application, although it should not be considered as the best one.

Using the measured frequency points ω_k (k = 1 ... K), the system consists of K rows like

$$\sum_{i=0}^{M_1} b_i e^{-j\omega_k T i} - S_{21}(\omega_k) \left[\sum_{i=1}^{M_2} a_i e^{-j\omega_k T i} \right] = S_{21}(\omega_k)$$
 (5.20)

where the T parameter is used for frequency normalization: $\omega_k T = \frac{\pi}{2} \frac{f_k}{f_c}$, being f_c the center measurement frequency. The system is over-determined, being the $M_1 + M_2 - 1$ unknown much less than the frequency points (K = 201 typically).

Different fittings with increasing $M_2 = 2 \dots M_{max}$ are performed on the same measurement data, and it has been verified that for the most of practical cases $M_1 = M_2$ or $M_1 = M_2 - 1$ achieves the best fitting. A simple solution consists on choosing the transfer function degree that minimizes the residuals variance.

As there could be more than one resonance in the measurement bandwidth, a choice is made based on an initial guess, given by the 3 dB method. The estimated resonant frequency $\hat{\omega}_{0n}$ and quality factor $\hat{Q}(\omega_{0n})$ are then computed from the resonance pole $\hat{p} = e^{j\tilde{\omega}_{0n}T}$ as

$$\hat{\omega}_{0n}T = \angle \hat{p} \tag{5.21}$$

$$\hat{Q}(\omega_{0n}) = -\frac{1}{2} \frac{\angle \hat{p}}{\log |\hat{p}|}$$

$$(5.22)$$

Similar relationships to (5.21) and (5.22) were derived by Young based on an electrical model of the cavity [130].

5.2.2 Optimal parameters and accuracy

The least-squares approach was found to outperform most estimation techniques in almost any practical case. However, simulations were carried out in order to find the critical aspects and set the optimal measurement settings. As a general rule, whichever effect that causes a lower numerical conditioning in (5.19) is likely to worsen the result's accuracy.

Frequency span

With wider measurement spans the conditioning is lower. This is a well known issue due to the Vandermonde system matrix in (5.19). The use of orthogonal polynomials may overcome the problem [122]. However, a normalized frequency span $\xi = \frac{\omega_{max} - \omega_{min}}{\omega_0} Q$ of about 3 was found to give optimal results for a wide range of resonator Q factors (Fig. 5.7).

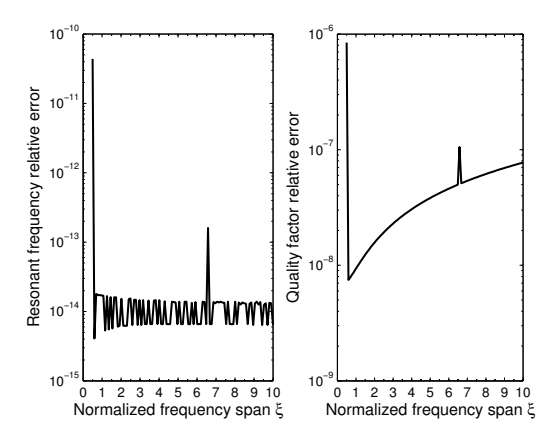


Figure 5.7. Simulation of the effect of the normalized frequency span ξ on the resonant frequency and Q factor accuracy. The resonance parameters were Q = 10000, $f_0 = 10$ GHz and peak magnitude $S_{21pk} = -50$ dB; 201 frequency points were used; no crosstalk and no cable delay are simulated. The fitting maximum degree is 3.

Uncompensated cables

Time delay due to long cables degrades the fitting accuracy, as this effect is inefficiently accounted for in terms of poles and zeros (Fig. 5.8). Therefore, the test cables should be included in the VNA calibration. However, a small uncompensated cable delay is effectively handled by the fitting routines. It was found that the uncompensated delay should not exceed $\pi/4$ phase shift in the measurement bandwidth, that means a few centimeters in terms of cable length.

External resonances

Long cables associated with a poor calibration may introduce artifacts like additional resonances in the data, since the input and output cavity matches are generally very

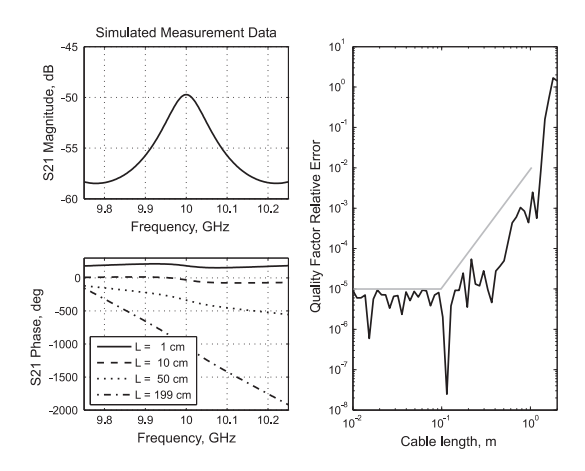


Figure 5.8. Simulation of the effect of uncompensated cables on the quality factor estimation. The simulated TE_{01p} resonance mode has p=23, Q=100, $f_0=10$ GHz and peak magnitude $S_{21pk}=-50$ dB; crosstalk has -80 dB magnitude. The cable dielectric has $\epsilon_r=2.1$. 201 frequency points were used and the fitting maximum degree is 41.

poor. However, the simulation showed that the effect is negligible (Fig. 5.9).

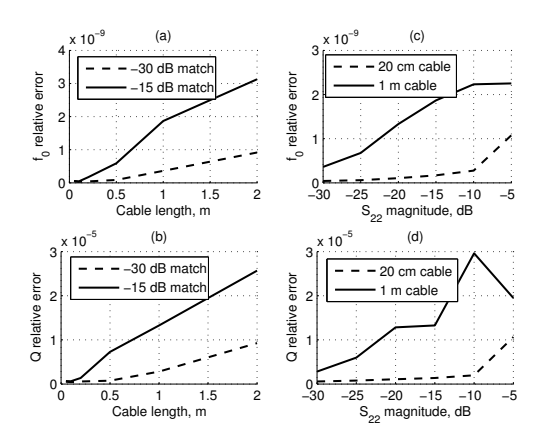


Figure 5.9. Simulation of the combined worst-case effect of mismatches and long cables. The simulated TE_{01p} resonance mode has p=23, Q=100, $f_0=10$ GHz and peak magnitude $S_{21pk}=-50$ dB; crosstalk has -80 dB magnitude. 201 frequency points were used.

Crosstalk and spurious resonances

Direct coupling between the cavity input and output ports (crosstalk), as well as spurious resonating modes require a transfer function with more poles and zeros. As the polynomial degree increases, its roots become less accurate due to the numerical computation.

A thorough simulation cannot be performed, as the number of simulation parameters is large. It has been found that the optimal fitting maximum degree for clean resonances is 3 to 5; with distorting effects (crosstalk and close-in spurious resonances) the degree raises to 15 or more. The lower degree compatible with a flat residuals plot should be chosen, as it generally corresponds to the most accurate result.

Noise

The low-coupling approximation requires maximum transmission coefficients less than -50 dB magnitude, thus the greatest source of error is due to the measurement noise. Simulations were performed in order to understand the effects on the resonance parameters, and are shown in Fig. 5.10. For low SNR, the results are bi-

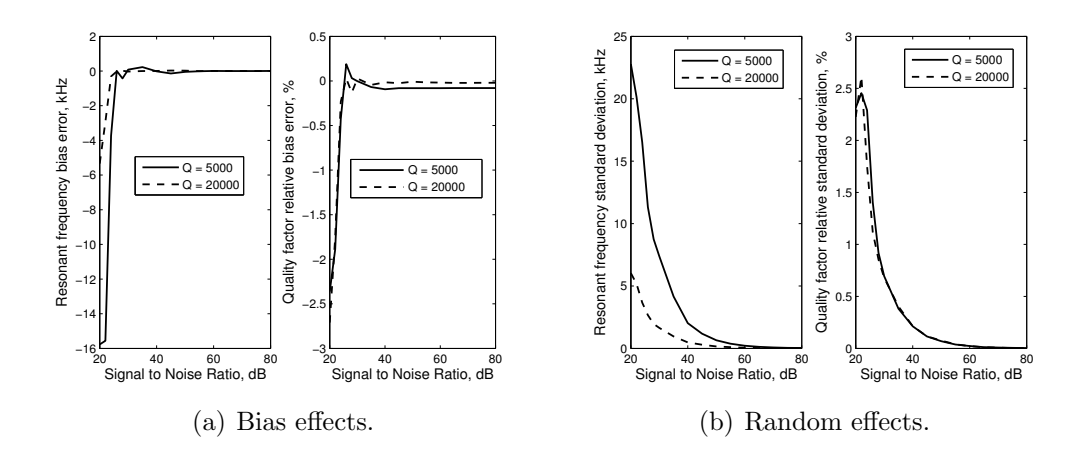


Figure 5.10. Simulation of the effect of noise. Realistic conditions were simulated. The resonance has $f_0 = 10$ GHz and peak magnitude -50 dB; crosstalk has -80 dB magnitude. 201 frequency points were used in a normalized frequency span of $\xi = 3$. 500 different noise realizations were simulated with a fitting maximum degree of 3.

ased, however, the bias rapidly vanishes above 30 dB SNR, where the random effects dominate (Fig. 5.10). The quality factor uncertainty of the method (three standard deviations) is below 1% for SNR of 40 dB and better. The resonant frequency accuracy improves nearly proportional to $\frac{1}{O}$, due to the reduction of the measurement

frequency span (the normalized frequency span ξ is fixed).

The systematic noise effects tend to lower the measured Q, and the bias worsens as the Q lowers. In most practical cases, the SNR is in the range 40–50 dB, thus the random effects dominate.

Uncertainty estimation of the resonance parameters

The fitting approach consists on two main parts:

- the transfer function polynomials are determined from the measurement data,
- the poles are computed as roots of the denominator polynomial.

Then, the resonance parameters are computed from the chosen resonance poles.

The main source of uncertainty is the noise level, but also the curve distortion plays a role. The uncertainty problem could be addressed by propagating the measurement noise through each step, if the algorithms had a closed form. Unfortunately, the polynomial numerator and denominator degrees are not known a priori but are iteratively determined, and thus a Monte Carlo method was chosen.

The fitting is performed several times on the measured data superimposed with synthetic noise, and the resonance parameters are recorded. In this way, all the distorting effects that may affect the measurement are taken into account. The added noise has a power spectral density equal to the residuals variance. The number of iterations N_{iter} is chosen high enough so that an increase in N_{iter} does not significantly change the results.

5.3 Measurement results

The method was validated by a comparison with the NIST magnitude-only extraction technique [110].

The measurement data were taken on the NIST 10 GHz 60 mm cavity, since it is a well-characterized resonator with a clean resonance [131, 132]. The resonator temperature-stabilized water jacket reduced the effects of thermal drift during the measurement process. The considered resonating mode was the TE_{01p} with p=23; the resonant frequency was nominally 10 GHz.

Fig. 5.11 shows the estimated resonance parameters. The relative standard deviation in the resonant frequency is estimated by de-trending the data to be less than $2 \cdot 10^{-8}$, which is close to the instrument's time base accuracy. In practice, such figures are of no use, being the cavity center-frequency repeatability of few parts in 10^{-5} . The Q factor standard deviation is 0.1%.

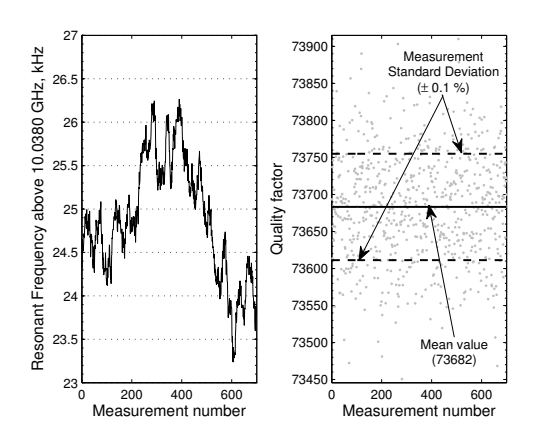


Figure 5.11. NIST 10 GHz 60 mm cavity resonator measurement.

The measured standard deviations are consistent with the uncertainty results from the Monte Carlo method, which is of no surprise since the latter tries to emulate the measurement noise. Fig. 5.12 shows the agreement between the NIST

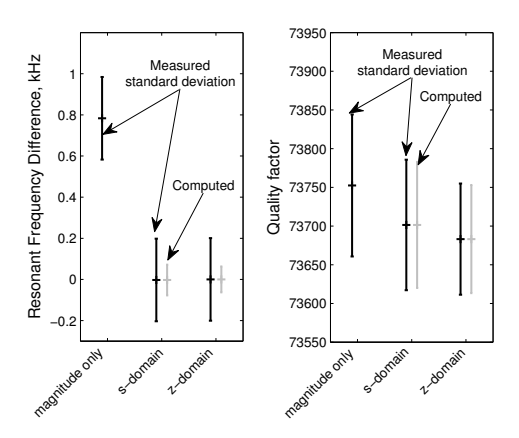


Figure 5.12. NIST 10 GHz 60 mm cavity resonator measurement comparison. The measurement data are the same used in Fig. 5.11. The black error bars are the measurement results, the gray ones are the computed uncertainties. 200 iterations were used for each measurement.

magnitude-only method results and two fitting methods. Both are Padé approximants, the polynomial basis function is $x(\omega) = e^{-j\omega T}$ for the z-domain method and $x(\omega) = j\omega$ for the fitting in the Laplace plane (s-domain). The resonant frequencies slightly differ, due to the different way of computing it. For all the practical purposes, this discrepancy is well below the resonator repeatability. The differences

in the resonant frequency standard deviations are due to limitations in de-trending the cavity thermal drift.

5.3.1 Split-Cylinder technique

A PTFE-based printed circuit board substrate was measured with the NIST 10 GHz Split-Cylinder Resonator. The measured sample thickness was 0.5 ± 0.05 mm. The cavity modal separation degrades with frequency thus very close interfering modes are present for the fourth and above TE_{0np} resonances. Since the sample dielectric parameters do not vary drastically with frequency, a smooth permittivity and loss tangent behavior is a good indicator of the method accuracy (Fig. 5.13). The

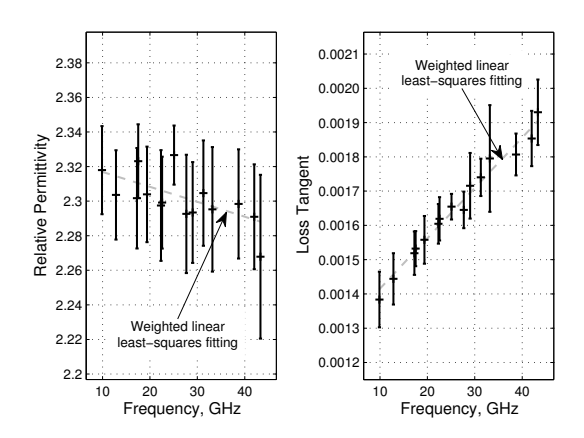


Figure 5.13. Split-Cylinder method permittivity and loss tangent results.

measured loss tangent data agree with a straight line up to 43 GHz; such agreement are usually obtained with samples having a loss tangent much lower [118] and the covered frequency band hardly exceeds one octave [117] with a single cavity resonator.

The error bars are combined uncertainties (2σ confidence), which, particularly for the permittivity, depend on the sample thickness uncertainty.

The magnitude-only method [110], although applied to the same measurement data, reveals poor capability of handling the distorting effects (Fig. 5.14). Above the fourth resonance, the loss in the sample and the presence of interfering effects greatly reduce the accuracy, being the resonances highly distorted as seen in the inset.

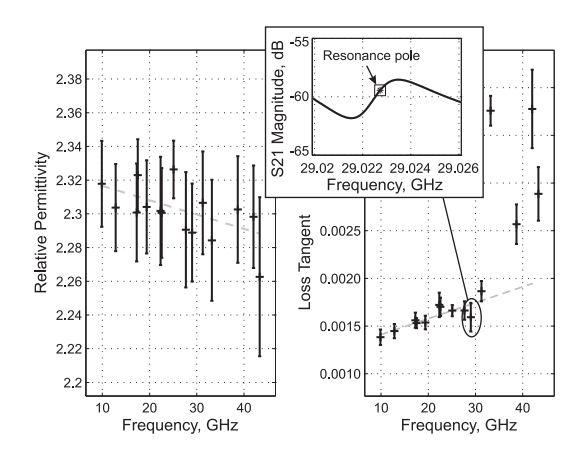


Figure 5.14. Split-Cylinder method permittivity and loss tangent results with the NIST magnitude-only method.

5.3.2 Considerations

The fitting method was compared against a well-documented technique and showed clear advantages. Similar results could be obtained in comparing with different techniques.

However, an evenly agreement is not proving the actual accuracy statement in the final results (permittivity and quality factor). Further comparisons using different techniques are being scheduled.

As the Split-Cylinder technique greatly profited from the better resonance estimates, future developments may consist on taking into account the TM resonance modes to obtain the normal permittivity component. Moreover, the mode-matching routines could be refined, since at the higher frequencies some results were found in disagreement with the lower-frequency trend-line. For the sample in Fig. 5.13, a bad agreement was found above 45 GHz, which could be due to resonances in the sample region not properly modeled.

Bibliography

- [1] "S-parameter design," Agilent Technologies, Santa Rosa, CA, Application Note AN 154, Jun. 2006.
- [2] 8405A Vector Voltmeter, Hewlett-Packard, Santa Rosa, CA, 1966.
- [3] HP 8515A S-Parameter and HP 8513A Reflection/Transmission Test-Sets Operating and Service Manual, Hewlett-Packard, Santa Rosa, CA, Sep. 1990.
- [4] N5242A 2-Port and 4-Port PNA-X Network Analyzer Data Sheet and Technical Specifications, Agilent Technologies, Santa Rosa, CA, Sep. 2008.
- [5] "Microwave multiport measurement system," Anritsu, Product Brochure 11410-00438, Jan. 2008.
- [6] A. Ferrero and U. Pisani, "An improved calibration technique for on-wafer large-signal transistor characterization," *IEEE Trans. Instrum. Meas.*, vol. 42, no. 2, pp. 360–364, Apr. 1993.
- [7] "Device characterization with harmonic source and load pull," Maury Microwave Co., Ontario, CA, Application Note 5C–054, Dec. 2000.
- [8] "Fundamental of rf and microwave noise figure measurements," Agilent Technologies, Santa Rosa, CA, Application Note AN 57-1, Oct. 2006.
- [9] J. Randa, "Microwave radiometry and noise standards at NIST," NIST-Boulder, RF Technology Division Seminar, Apr. 2003.
- [10] Operating and Service Manual Agilent 346A/B/C Noise Source, Agilent Technologies, Santa Rosa, CA, Jun. 2001.
- [11] "Noise figure measurement accuracy the Y-Factor method," Agilent Technologies, Santa Rosa, CA, Application Note AN 57-2, Mar. 2004.
- [12] "Noise figure primer," Hewlett-Packard, Santa Rosa, CA, Application Note AN 57, Jan. 1965.
- [13] "Applications and operation of the 8970A noise figure meter," Hewlett–Packard, Santa Rosa, CA, Product Note 8970A-1, Nov. 1981.
- [14] N. Marcuvitz, Ed., Waveguide Handbook, ser. IEEE Electromagnetic Waves Series. Stevenage, UK: Institution of Electrical Engineers, 1986.
- [15] R. Marks and D. Williams, "A general waveguide circuit theory," J. Res. Natl. Inst. Stand. Technol., vol. 97, pp. 533–561, Sep. 1992.
- [16] J. Penfield, P., "Wave representation of amplifier noise," IRE Transactions on

- Circuit Theory, vol. 9, no. 1, pp. 84–86, Mar. 1962.
- [17] R. P. Meys, "A wave approach to the noise properties of linear microwave devices," *IEEE Trans. Microw. Theory Tech.*, vol. 26, no. 1, pp. 34–37, Jan. 1978.
- [18] S. W. Wedge and D. B. Rutledge, "Wave techniques for noise modeling and measurement," *IEEE Trans. Microw. Theory Tech.*, vol. MTT-40, pp. 2004– 2012, Nov. 1992.
- [19] A. Van Der Ziel, *Noise in Solid State Devices and Circuits*. New York, US: Wiley-Interscience, 1986.
- [20] J. Johnson, "Thermal agitation of electricity in conductors," *Phys. Rev.*, vol. 32, no. 1, p. 97, Jul. 1928.
- [21] H. Nyquist, "Thermal agitation of electric charge in conductors," *Phys. Rev.*, vol. 32, no. 1, pp. 110–113, Jul. 1928.
- [22] H. Bosma, "On the theory of linear noisy systems," *Philips Res. Rep. Suppl.*, no. 10, pp. 1–190, 1967.
- [23] F. K. Weinert, "The RF vector voltmeter an important new instrument for amplitude and phase measurements from 1 MHz to 1000 MHz," *Hewlett-Packard Journal*, vol. 17, no. 9, pp. 1–9, May 1966.
- [24] "Pulse and waveform generation with step-recovery diodes," Hewlett-Packard Co., Santa Rosa, CA, Application Note AN 918, Oct. 1984.
- [25] J.-C. Tippet and R.-A. Speciale, "A rigorous technique for measuring the scattering matrix of a multiport device with a 2-port network analyzer," *IEEE Trans. Microwave Theory Tech.*, vol. MTT-30, no. 5, pp. 661–666, May 1982.
- [26] J.-C. Rautio, "Techniques for correcting scattering parameter data of an imperfectly terminated multiport when measured with a two-port network analyzer," *IEEE Trans. Microwave Theory Tech.*, vol. MTT-31, no. 5, pp. 407–412, May 1983.
- [27] S. Sercu and L. Martens, "Characterizing N-port packages and interconnections with a 2-port network analyzer," *IEEE 6th Topical Meeting on Electrical Performance of Electronic Packaging*, pp. 163–166, Oct. 1997.
- [28] I. Rolfes and B. Schiek, "Measurement of the scattering-parameters of planar multi-port devices," in *European Microwave Conference*, vol. 2, Oct. 2005.
- [29] A. Ferrero and F. Sanpietro, "A simplified algorithm for leaky network analyzer calibration," *IEEE Microwave and Guided Wave Letters*, vol. 5, no. 4, pp. 119–121, Apr. 1995.
- [30] A. Ferrero, F. Sampietro, and U. Pisani, "Multiport vector network analyzer calibration: a general formulation," *IEEE Trans. Microw. Theory Tech.*, vol. 42, pp. 2455–2461, Dec. 1994.
- [31] V. Teppati and A. Ferrero, "On-wafer calibration algorithm for partially leaky multiport vector network analyzers," *IEEE Trans. Microw. Theory Tech.*, vol. 53, no. 11, pp. 3665–3671, Nov. 2005.

- [32] G. L. Madonna, "Measurement techniques for microwave device and circuit characterization," Ph.D. dissertation, Politecnico di Torino, 1999.
- [33] J. Martens, D. Judge, and J. Bigelow, "Multiport vector network analyzer measurements," *IEEE Microw. Mag.*, vol. 6, no. 4, pp. 72–81, Dec. 2005.
- [34] H. Heuermann, "GSOLT: the calibration procedure for all multi-port vector network analyzers," in *IEEE MTT-S International Microwave Symposium Digest*, vol. 3, Jun. 2003, pp. 1815–1818.
- [35] A. Ferrero, V. Teppati, M. Garelli, and A. Neri, "A novel calibration algorithm for a special class of multiport vector network analyzers," *IEEE Trans. Microw. Theory Tech.*, vol. 56, no. 3, pp. 693–699, Mar. 2008.
- [36] R. B. Marks, "Formulations of the basic vector network analyzer error model including switch-terms," in 50th ARFTG Conference Digest, vol. 32, Dec. 1997, pp. 115–126.
- [37] A. Ferrero and V. Teppati, "Development and implementation of a new multiport calibration algorithm," in 70th ARFTG Conference Digest, Nov. 2007.
- [38] H. J. Eul and B. Schiek, "A generalized theory and new calibration procedures for network analyzer self-calibration," *IEEE Trans. Microw. Theory Tech.*, vol. 39, no. 4, pp. 724–731, Apr. 1991.
- [39] A. Ferrero and U. Pisani, "QSOLT: A new fast calibration algorithm for two port S parameter measurements," in 38th ARFTG Conference Digest, vol. 20, San Diego, CA, USA, Dec. 1991, pp. 15–24.
- [40] —, "Two-port network analyzer calibration using an unknown 'thru'," *IEEE Microwave and Guided Wave Letters*, vol. 2, no. 12, pp. 505–507, Dec. 1992.
- [41] N. R. Franzen and R. A. Speciale, "A new procedure for system calibration and error removal in automated s-parameter measurements," in 5th European Microwave Conference, Hamburg, Germany, Oct. 1975, pp. 69–73.
- [42] G. F. Engen and C. A. Hoer, "Thru-reflect-line: An improved technique for calibrating the dual six-port automatic network analyzer," *IEEE Trans. Mi*crow. Theory Tech., vol. 27, no. 12, pp. 987–993, Dec. 1979.
- [43] R. B. Marks, "A multiline method of network analyzer calibration," *IEEE Trans. Microw. Theory Tech.*, vol. 39, no. 7, pp. 1205–1215, Jul. 1991.
- [44] J. Fitzpatrick, "Error models for systems measurements," *Microwave J.*, pp. 63–66, May 1978.
- [45] H. J. Eul and B. Schiek, "Thru-match-reflect: One result of a rigorous theory for de-embedding and network analyzer calibration," in 18th European Microwave Conference, Oct. 1988, pp. 909–914.
- [46] F. Sanpietro, A. Ferrero, U. Pisani, and L. Brunetti, "Accuracy of a multiport network analyzer," *IEEE Trans. Instrum. Meas.*, vol. 44, no. 2, pp. 304–307, Apr. 1995.
- [47] A. Ferrero, F. Sanpietro, and U. Pisani, "Accurate coaxial standard verification by multiport vector network analyzer," in *IEEE MTT-S International*

- Microwave Symposium Digest, San Diego, CA, May 23–27, 1994, pp. 1365–1368.
- [48] B. Donecker, "Determining the measurement accuracy of the HP 8510 microwave network analyzer," in 23rd ARFTG Conference Digest, vol. 5, Jun. 1984, pp. 51–84.
- [49] "Guidelines on the evaluation of vector network analyzers (vna)," EURAMET, Calibration Guide EURAMET/cg-12/v.01, Jul. 2007.
- [50] J. Randa and D. K. Walker, "On-wafer measurement of transistor noise parameters at NIST," *IEEE Trans. Instrum. Meas.*, vol. 56, no. 2, pp. 551–554, Apr. 2007.
- [51] V. Teppati, "Microwave device characterization techniques oriented to increase the measurement accuracy," Ph.D. dissertation, Politecnico di Torino, 2002.
- [52] G. P. Bava, U. Pisani, and V. Pozzolo, "Active load technique for load-pull characterization at microwave frequencies," *Electronic Lett.*, vol. 18, pp. 178–179, Feb. 1982.
- [53] A. Ferrero, "Active load or source impedance synthesis apparatus for measurement test set of microwave components and systems," U.S. Patent 6 509 743, Jan. 21, 2003.
- [54] D. E. Bockelman and W. R. Eisenstadt, "Combined differential and common-mode scattering parameters: theory and simulation," *IEEE Trans. Microw. Theory Tech.*, vol. 43, pp. 1530–1539, Jul. 1995.
- [55] A. Ferrero and M. Pirola, "Generalized mixed-mode S-parameters," *IEEE Trans. Microw. Theory Tech.*, vol. 54, no. 1, pp. 458–463, Jan. 2006.
- [56] M. Spirito, M. P. van der Heijden, M. de Kok, and L. C. N. de Vreede, "A calibration procedure for on-wafer differential load-pull measurements," in 61st ARFTG Conference Digest, Jun. 13, 2003, pp. 1–4.
- [57] W. Liu and C. Tsironis, "Load pull characterization system for differential devices," in 62nd ARFTG Microwave Measurements Conference, Dec. 4–5, 2003, pp. 201–204.
- [58] V. Teppati, A. Ferrero, M. Garelli, and S. Bonino, "A comprehensive mixed-mode time-domain load- and source-pull measurement system," *IEEE Trans. Instrum. Meas.*, accepted for publication.
- [59] M. Garelli and S. Terrando, "Caratterizzazione a radiofrequenza di dispositivi bilanciati: Progetto e realizzazione di un banco load-pull mixed-mode," Master's thesis, Politecnico di Torino, Torino, Italy, Sep. 2005.
- [60] A. Ferrero and V. Teppati, "A novel active differential/common-mode load for true mixed-mode load-pull systems," in *IEEE MTT-S International Mi*crowave Symposium Digest, San Francisco, CA, Jun. 2006, pp. 1456–1459.
- [61] A. Ferrero, "Caratterizzazione di dispositivi attivi a microonde in regime di linearità e non linearità," Ph.D. dissertation, Politecnico di Torino, 1992.

- [62] "The microwave transition analyzer: a versatile measurement set for bench and test," Hewlett-Packard, Rohnert Park, CA, Product Note 70820-1, 1991.
- [63] H. Arthaber, M. Mayer, A. Gafni, N. Gadringer, and G. Margerl, "A time-domain large-signal measurement setup," Int. J. RF Microwave, vol. 15, no. 1, pp. 3–12, Jan. 2005.
- [64] A. Ferrero and V. Teppati, "A complete measurement test-set for non-linear device characterization," in ARFTG Conference Digest-Fall, 58th, vol. 40, San Diego, CA, USA, Nov. 2001, pp. 1–3.
- [65] P. Colantonio, F. Giannini, E. Limiti, and V. Teppati, "An approach to harmonic load- and source-pull measurements for high-efficiency PA design," *IEEE Trans. Microwave Theory Tech.*, vol. MTT-52, no. 1, pp. 191–198, Jan. 2004.
- [66] J. Benedikt, R. Gaddi, P. J. Tasker, M. Goss, and M. Zadeh, "High power time domain measurement system with active harmonic load-pull for high efficiency base station amplifier design," in *IEEE MTT-S International Microwave Sym*posium Digest, vol. 3, Boston, MA, Jun. 11–16, 2000, pp. 1459–1462.
- [67] A. Sheikh, C. Roff, J. Benedikt, P. J. Tasker, B. Noori, P. Aaen, and J. Wood, "Systematic waveform engineering enabling high efficiency modes of operation in Si LDMOS at both L-band and S-band frequencies," in *IEEE MTT-S International Microwave Symposium Digest*, Atlanta, GA, USA, Jun. 15–20, 2008, pp. 1143–1146.
- [68] F. De Groote, J.-P. Teyssier, J. Verspecht, and J. Faraj, "High power on-wafer capabilities of a time domain load-pull setup," in *IEEE MTT-S International Microwave Symposium Digest*, Atlanta, GA, USA, Jun. 15–20, 2008, pp. 100– 102.
- [69] S. C. Cripps, Advanced Techniques in RF Power Amplifier Design. Boston: Artech House, May 2002.
- [70] A. Van Der Ziel, Noise in Measurements. New York, US: John Wiley & Sons, Inc, Sep. 1976.
- [71] H. A. Haus, "Optimum noise performance of optical amplifiers," *IEEE J. Quantum Electron.*, vol. 37, no. 6, pp. 813–823, Jun. 2001.
- [72] N2002A Noise Source Test Set User's Guide, Agilent Technologies, Santa Rosa, CA, Jun. 2003.
- [73] C. Grosvenor, J. Randa, and R. Billinger, "Design and testing of NFRad-a new noise measurement system," NIST, Technical Note 1518, Mar. 2000.
- [74] —, "NFRad–review of the new NIST noise measurement system," in 55st ARFTG Conference Digest, 2000, pp. 135–144.
- [75] H. A. Haus, W. R. Atkinson, G. M. Branch, W. B. Davenport, W. H. Fonger, W. A. Harris, S. W. Harrison, W. W. McLeod, E. K. Stodola, and T. E. Talpey, "Representation of noise in linear twoports," in *Proceedings of the IRE*, vol. 48, no. 1, Jan. 1960, pp. 69–74.

- [76] J. Randa, "Noise characterization of multiport amplifiers," *IEEE Trans. Microw. Theory Tech.*, vol. 49, pp. 1757–1763, Oct. 2001.
- [77] —, "Noise-parameters uncertainties: A Monte Carlo simulation," J. Res. Natl. Inst. Stand. Technol., vol. 107, no. 5, pp. 431–444, Sep. 2002.
- [78] J. Randa and W. Wiatr, "Monte Carlo estimation of noise-parameter uncertainties," in *IEE Proc.-Sci. Meas. Technol.*, vol. 149, no. 6, Nov. 2002, pp. 333–337.
- [79] M. Sannino, "On the determination of device noise and gain parameters," *Proc. IEEE*, vol. 67, no. 9, pp. 1364–1366, Sep. 1979.
- [80] ——, "Simultaneous determination of device noise and gain parameters through noise measurements only," *Proc. IEEE*, vol. 68, no. 10, pp. 1343–1345, Oct. 1980.
- [81] H. T. Friis, "Noise figures of radio receivers," Proc. IRE, vol. 32, no. 7, pp. 419–422, Jul. 1944.
- [82] R. Q. Lane, "The determination of device noise parameters," *Proc. IEEE*, vol. 57, no. 8, pp. 1461–1462, Aug. 1969.
- [83] E. W. Strid, "Measurement of losses in noise-matching networks," *IEEE Trans. Microw. Theory Tech.*, vol. 29, no. 3, pp. 247–252, Mar. 1981.
- [84] L. F. Tiemeijer, R. J. Havens, R. de Kort, and A. J. Scholten, "Improved Y-factor method for wide-band on-wafer noise-parameter measurements," *IEEE Trans. Microw. Theory Tech.*, vol. 53, no. 9, pp. 2917–2925, Sep. 2005.
- [85] V. Adamian and A. Uhlir, "A novel procedure for receiver noise characterization," *IEEE Trans. Instrum. Meas.*, vol. IM-22, pp. 181–182, Jun. 1973.
- [86] A. Davidson, B. Leake, and E. Strid, "Accuracy improvements in microwave noise parameter measurements," *IEEE Trans. Microwave Theory Tech.*, vol. MTT-37, pp. 1973–1978, Dec. 1979.
- [87] G. Simpson, D. Ballo, J. Dunsmore, and A. Ganwani, "A new noise parameter measurement method results in more than 100x speed improvement and enhanced measurement accuracy," in 72ndt ARFTG Conference Digest, Dec. 2008.
- [88] D. Ballo, "Making source-corrected noise-figure measurements," *ED Online*, Sep. 2007.
- [89] N5242A-029 PNA-X Source-Corrected Noise Figure Measurement, Agilent Technologies, Santa Rosa, CA, Oct. 2008.
- [90] J. Randa, "Uncertainty analysis for NIST noise-parameter measurements," NIST, Technical Note 1530, Mar. 2008.
- [91] M. Garelli, A. Ferrero, and S. Bonino, "A complete noise- and scattering-parameters test-set," *IEEE Trans. Microw. Theory Tech.*, to be published in Mar. 2009.
- [92] G. Caruso and M. Sannino, "Analysis of frequency-conversion techniques in

- measurements of microwave transistor noise temperatures," *IEEE Trans. Microw. Theory Tech.*, vol. 25, no. 11, pp. 870–873, Nov. 1977.
- [93] V. Teppati and A. Ferrero, "A new class of nonuniform, broadband, nonsymmetrical rectangular coaxial-to-microstrip directional couplers for high power applications," *IEEE Microw. Wireless Compon. Lett.*, vol. 13, no. 4, pp. 152–154, Apr. 2003.
- [94] I. Bahl and K. Ely, "Modern microwave substrate materials," *Microwave Journal*, vol. 33, pp. 131–146, 1990.
- [95] J. Baker-Jarvis, M. D. Janezic, B. Riddle, H. L. Holloway, N. G. Paulter, and J. E. Blendell, "Dielectric and conductor-loss characterization and measurements on electronic packaging materials," NIST, Technical Note 1520, Jul. 2001.
- [96] B. Bianco, M. Parodi, S. Ridella, and F. Selvaggi, "Launcher and microstrip characterization," *IEEE Trans. Instrum. Meas.*, vol. 25, no. 4, pp. 320–323, Dec. 1976.
- [97] J. Baker-Jarvis, R. G. Geyer, J. Grosvenor, J. H., M. D. Janezic, C. A. Jones, B. Riddle, C. M. Weil, and J. Krupka, "Dielectric characterization of low-loss materials a comparison of techniques," *IEEE Trans. Dielectr. Electr. Insul.*, vol. 5, no. 4, pp. 571–577, Aug. 1998.
- [98] C. N. Works, T. W. Dakin, and F. W. Boggs, "A resonant-cavity method for measuring dielectric properties at ultra-high frequencies," in *Proceedings of the IRE*, vol. 33, no. 4, Apr. 1945, pp. 245–254.
- [99] J. Baker-Jarvis and B. Riddle, "Dielectric measurements using a reentrant cavity: Mode-matching analysis," NIST, Technical Note 1384, 1996.
- [100] W. P. Westphal, Techniques of measuring the permittivity and permeability of liquids and solids in the frequency range 3 c/s to 50 kMc/s. MIT XXXVI, 1950.
- [101] J. Baker-Jarvis, M. D. Janezic, J. H. Grosvenor, and R. G. Geyer, "Transmission/reflection and short-circuit line methods for measuring permittivity and permeability," NIST, Technical Note 1355, 1994.
- [102] G. C. Montgomery, R. H. Dicke, and E. M. Purcell, *Principles of Microwave Circuits*. McGraw-Hill, 1948.
- [103] E. L. Ginzton, Microwave Measurements. McGraw-Hill, 1957.
- [104] R. E. Collin, Foundations for Microwave Engineering, 2nd ed. Wiley, 2000.
- [105] K. Leong and J. Mazierska, "Precise measurements of the Q factor of dielectric resonators in the transmission mode-accounting for noise, crosstalk, delay of uncalibrated lines, coupling loss, and coupling reactance," *IEEE Trans. Microw. Theory Tech.*, vol. 50, no. 9, pp. 2115–2127, Sep. 2002.
- [106] P. J. Petersan and S. M. Anlage, "Measurement of resonant frequency and quality factor of microwave resonators: Comparison of methods," *Journal of Applied Physics*, vol. 84, no. 6, pp. 3392–3402, Sep. 1998.

- [107] J. T. Verdeyen, Laser electronics. Prentice-Hall, 1981.
- [108] D. Kajfez and E. J. Hwan, "Q-factor measurement with network analyzer," *IEEE Trans. Microw. Theory Tech.*, vol. 32, no. 7, pp. 666–670, Jul. 1984.
- [109] D. Kajfez, "Linear fractional curve fitting for measurement of high Q factors," *IEEE Trans. Microw. Theory Tech.*, vol. 42, pp. 1149–1153, Jul. 1994.
- [110] K. J. Coakley, J. D. Splett, M. D. Janezic, and R. F. Kaiser, "Estimation of Q-factors and resonant frequencies," *IEEE Trans. Microw. Theory Tech.*, vol. 51, no. 3, pp. 862–868, Mar. 2003.
- [111] T. Miura, "A proposal for standard to compare Q-factor evaluation accuracy of microwave resonator," *IEEE MTT-S International Microwave Symposium Digest*, pp. 1963–1966, Jun. 2006.
- [112] G. Kent, "An evanescent-mode tester for ceramic dielectric substrates," *IEEE Trans. Microw. Theory Tech.*, vol. 36, no. 10, pp. 1451–1454, Oct. 1988.
- [113] —, "Nondestructive permittivity measurement of substrates," *IEEE Trans. Instrum. Meas.*, vol. 45, no. 1, pp. 102–106, Feb. 1996.
- [114] G. Kent and S. M. Bell, "The gap correction for the resonant-mode dielectrometer," *IEEE Trans. Instrum. Meas.*, vol. 45, no. 1, pp. 98–101, Feb. 1996.
- [115] M. D. Janezic, E. F. Kuester, and J. B. Jarvis, "Broadband complex permittivity measurements of dielectric substrates using a split-cylinder resonator," *IEEE MTT-S International Microwave Symposium Digest*, vol. 3, pp. 1817–1820, Jun. 6–11, 2004.
- [116] M. D. Janezic, "Nondestructive relative permittivity and loss tangent measurements using a split-cylinder resonator," Ph.D. dissertation, University of Colorado at Boulder, 2003.
- [117] IPC-TM-650 2.5.5.13 Relative Permittivity and Loss Tangent Using a Split-Cylinder Resonator, IPC Association Connecting Electronics Industries, Jan. 2007.
- [118] Agilent 85072A 10 GHz Split Cylinder Resonator, Agilent Technologies, Apr. 2007.
- [119] C. H. Liang, L. Li, and T. Su, "Analysis of resonance problems of arbitrarily complicated transmission line cavities by using complex phase angle theory," *IEEE Antennas Wireless Propag. Lett.*, vol. 5, no. 1, pp. 76–79, Dec. 2006.
- [120] J. D. Jackson, Classical Electrodynamics. John Wiley & Sons, 1962.
- [121] H. Rothe and W. Dahlke, "Theory of noisy fourpoles," *Proceedings of the IRE*, vol. 44, no. 6, pp. 811–818, Jun. 1956.
- [122] W. T. Beyene, "Improving time-domain measurements with a network analyzer using a robust rational interpolation technique," *IEEE Trans. Microw. Theory Tech.*, vol. 49, no. 3, pp. 500–508, Mar. 2001.
- [123] S. Grivet-Talocia, I. S. Stievano, I. A. Maio, and F. Canavero, "Time-domain and frequency-domain macromodeling: application to package structures," in

- 2003 IEEE International Symposium on Electromagnetic Compatibility, vol. 2, Aug. 2003, pp. 570–574.
- [124] R. Neumayer, A. Stelzer, and R. Weigel, "Identification of microwave device and packaging models from frequency response data," in *SBMO/IEEE MTT-S International Microwave and Optoelectronics Conference*, vol. 2, Sep. 20–23, 2003, pp. 961–965.
- [125] K. M. Cuomo, J. E. Pion, and J. T. Mayhan, "Ultrawide-band coherent processing," *IEEE Trans. Antennas Propag.*, vol. 47, no. 6, pp. 1094–1107, Jun. 1999.
- [126] B. Gustavsen and A. Semlyen, "Rational approximation of frequency domain responses by vector fitting," *IEEE Trans. Power Del.*, vol. 14, no. 3, pp. 1052– 1061, Jul. 1999.
- [127] D. Deschrijver, B. Haegeman, and T. Dhaene, "Orthonormal vector fitting: A robust macromodeling tool for rational approximation of frequency domain responses," in *IEEE Trans. Adv. Packag.*, vol. 30, no. 2, West Point, NY, USA, May 2007, pp. 216–225.
- [128] Y. S. Mekonnen and J. E. Schutt-Aine, "Fast macromodeling technique of sampled time/frequency data using z-domain vector-fitting method," in *Elec*trical Performance of Electronic Packaging, 2007 IEEE, Atlanta, GA, USA,, Oct. 2007, pp. 47–50.
- [129] K. Naishadham and J. E. Piou, "A signal model to extract intrinsic parameters of high-Q dielectric resonators from noisy measurements," 2005 IEEE MTT-S International Microwave Symposium Digest, Jun. 12–17, 2005.
- [130] L. Young, "Q factors of a transmission line cavity," *IRE Transactions on Circuit Theory*, vol. 4, no. 1, pp. 3–5, Mar. 1957.
- [131] E. Vanzura, R. Geyer, and M. Janezic, "The NIST 60-millimeter diameter cylindrical cavity resonator: Performance evaluation for permittivity measurements," NIST, Technical Note 1354, 1993.
- [132] M. D. Janezic, J. D. Splett, K. J. Coakley, R. F. Kaiser, and J. H. Grosvenor, "Relative permittivity and loss tangent measurement using the NIST 60 mm cylindrical cavity," NIST, Special Publication 260-159, Sep. 2005.